HARVARD
Kenneth C. Griffin

GRADUATE SCHOOL
OF ARTS AND SCIENCES

DISSERTATION ACCEPTANCE CERTIFICATE

The undersigned, appointed by the

Department of Chemistry & Chemical Biology

have examined a dissertation entitled:

Ultracold Atom-Polar Molecule Interactions: Discoveries, Surprises and Puzzles

presented by: Lingbang Zhu

candidate for the degree of Doctor of Philosophy and hereby certify that it is worthy of acceptance.

Signature _____

Typed name: Professor Kang-Kuen Ni

Signature _____

Typed name: Professor Eric Heller

Signature _____

Typed name: Professor Suyang Xu

Date: 19 August 2025

Ultracold Atom-Polar Molecule Interactions: Discoveries, Surprises and Puzzles

A dissertation presented

by

Lingbang Zhu

to

The Department of Chemistry and Chemical Biology

in partial fulfillment of the requirements

for the degree of

Doctor of Philosophy

in the subject of

Chemical Physics

Harvard University

Cambridge, Massachusetts

August 2025

Dissertation Advisor: Professor Kang-Kuen Ni Lingbang Zhu

Ultracold Atom-Polar Molecule Interactions: Discoveries, Surprises and Puzzles

Abstract

Studying ultracold chemical reactions with quantum state resolution reveals details of the reaction processes, especially with single quantum state preparation of the reactants and state-selective detection of reaction products. In this thesis, we investigate two main processes: KRb + KRb $\rightarrow$ K_2 + Rb_2 reactions, and Rb and KRb atom-molecule collisions.

In the KRb bimolecular reaction, we demonstrate the preservation of quantum coherence in bimolecular reactions for the first time, which is surprising in a reaction considered to be largely chaotic. Additionally, we proposed a coherent control scheme to manipulate product yields across different product channels. These results represent a critical step toward probing quantum coherence and entanglement in the chemical reaction.

In atom-molecule collisions between Rb and KRb, we discovered an exceptionally long-lived intermediate complex, KRb_2, which can be photo-excited by trapping light. The observed complex lifetime was orders of magnitude longer than theoretical predictions, underscoring the limitations of the current theory. We further explored the dependence of complex lifetimes on the initial quantum states and external

electric and magnetic fields, providing additional experimental benchmarks to guide future theoretical work.

Separately, we found that inelastic collisions between hyperfine-excited Rb atoms and KRb molecules can lead to rotation excitation of KRb post-collision. By probing the product state distribution, the result suggests that mechanical angular momentum is coupled to the spins. Such couplings are too weak in the current theory models to explain the result. Moreover, our result contradicts state-of-the-art coupled-channel calculations. These suggest that some subtle effects, such as molecular vibration and conical intersections, play a critical role in the reaction dynamics.

The final piece of the thesis describes the observation of resonant interaction between a Rydberg atom and an ensemble of polar molecules. Such hybrid quantum systems have been proposed for a wide range of applications. Our work provides an experimental demonstration of resonant dipolar interactions between Rydberg atoms and ultracold polar molecules, paving the way for the realization of hybrid systems for quantum computation and simulation.

Contents

Acknowledgments

First and foremost, I would like to thank my advisor, Kang-Kuen Ni, for her unwavering support and guidance over the past six years. I've learned so much from her—both about the science we do in the lab and about how to think critically, ask the right questions, and approach problems systematically and rigorously. Working with her has also helped me grow immensely in scientific communication and presentation. I've also become more logical and clear in expressing my ideas, both verbally and in writing. These are lessons that have become a core part of who I am, and I'll carry them with me wherever I go.

I've also had the pleasure of having Prof. Eric Heller and Prof. Suyang Xu as co-advisors for my thesis. Prof. Heller taught a semester-long course that really helped me build intuition for using semiclassical methods to tackle quantum mechanical problems in my research. Our discussions were always exciting—he often pointed me toward ideas and directions I hadn't considered before. Prof. Suyang Xu has also been incredibly supportive during our discussions, helping me think more clearly and plan more effectively.

Our research group has always been a supportive and fun community, from the time I first joined the lab to the moment I'll be leaving. I'm especially grateful to everyone on the KRb team. Yu Liu and Ming-Guang Hu built this one-of-a-kind, amazing experiment and generously shared their knowledge with me, helping me understand the scientific ideas and working principles behind the setup. Although

we joined the lab around the same time, Matthew Nichols quickly became incredibly skilled at running the experiment. During the tough times of the pandemic, he was essentially the one teaching me how to operate the experiment, and I'm truly thankful for that. Yi-Xiang Liu is the person I have worked with the longest. Together, we fought through many challenges—maintaining and running the experiment when neither of us was very familiar with the setup, searching for real and meaningful signals in the Rydberg experiment, and puzzling over theoretical explanations for many of our results. She's one of the hardest-working and resilient people I've met, and it's been an honor to work alongside her for over three years. Mark Babin joined our experiment for two years, bringing a fresh perspective with his background in physical chemistry. He's a genuinely kind person, and I learned a lot from seeing our scientific work through his lens. Jeshurun Luke, who joined the project three years after me, is both incredibly smart and hardworking. He has made significant contributions to both the experiment and theory, and I'm confident that he'll carry the project forward with great momentum. It's also been a pleasure having Roy Shaham join the team in 2024. He has a strong grasp of physics and is a great person to bounce ideas off. His MATLAB skills are unmatched within the team and have had a significant impact on our data processing and analysis. Robin Wang joined our lab in early 2025 and is the newest member of the experiment. I wish her all the best in her scientific journey ahead. Lastly, in the summer of 2023, we had a visiting student, Arfor Houwman, who joined the KRb team temporarily. His contributions went beyond just science—he also brought us some great times,

including organizing some memorable candlepin bowling nights.

Members of the Ni Lab working on other experiments have also played an important role in guiding me, both scientifically and in the practical aspects of building apparatus for the experiments. During the summer of 2018, when I briefly worked with the NaCs 1.5 team, Jessie Zhang and Yen-Wei Lin taught me a great deal about constructing ECDLs from scratch and properly setting up a phase lock system. At the start of my PhD, I received a great deal of help from other senior members of the lab, including Yichao Yu, William Cairncross, and Lewis Picard. Yichao is one of the smartest people I've ever met—his enthusiasm for science is contagious, and he always seemed to have the right answer to any question I asked. Will is a concise, professional, and highly focused physicist. Lewis stands out as someone who is not only scientifically driven but also socially perceptive and thoughtful. Among all the senior members of the Ni Lab, I probably interacted and learned the most from Kenneth Wang. Our connection went beyond work, and I really appreciated the friendship and support he offered throughout the years.

I'd also like to thank the many people who joined the lab after me, including Yu Wang, Ryan Cimmino, Fang Fang, and Hunter Kenemy from the NaCs Rydberg experiment, Annie Jihyun Park, Gabriel Patenotte, Samuel Gebretsadkan, and Youngshin Kim from the NaCs 1.5 experiment, Conner Williams, Christian Nunez, and Amanda Younes from the NaCs 2.0 experiment, and finally Lysander Christakis, Dewei Gong, and Ziguang Lin from the Yb experiment, who contributed to the collaborative and friendly environment that makes the Ni Lab so special. The

welcoming and collaborative spirit of our group is truly the result of contributions from every single member.

Beyond our laboratory, a remarkable network of theorists has shaped the way we think about ultracold molecules and their collisions. I am deeply grateful to Goulven Quéméner, John Bohn, Tijs Karman, and Matthew Frye, whose lively, in-depth discussions have illuminated the labyrinth of the long-lived intermediate complex and helped steer our ideas. For the Rb + KRb collision project, I owe special thanks to Timur Tschurbul, Michal Tomza, and John Bohn. Their insights were indispensable in forging the theoretical backbone that supports our experimental findings. Finally, conversations with Grigor Adamyan and Artem Volosniev proved invaluable as we crafted an in-house framework to capture the subtle interactions between Rydberg Rb atoms and KRb molecules.

I'd also like to thank my undergraduate advisor, Shengwang Du, for giving me incredible opportunities to explore AMO research throughout all four years of college. The training I received in his group transformed me from a complete newcomer into someone who understood what real research is like—not just the polished stories from textbooks or pop science videos, but the actual day-to-day experience of doing science. That experience laid the foundation for the skills and mindset I needed to proceed in my PhD research.

Finally, I can never thank my parents, Hong and Hongshan, enough for raising me and always providing the best care and resources for everything in life. Even though we haven't seen each other in person for more than five years, their

unwavering support has been essential in helping me push through the toughest times during my six years of PhD. I'm deeply grateful to my wife, Qinwen Zhai, for her love and support throughout our nine years together. She stood by me through the darkest days of the pandemic and during times when we were oceans apart. Her presence in my life means everything to me. And last but not least, I want to thank our chinchilla, Inky, who just turned two years old, for being adorable and for providing emotional support in his own fluffy way. He has no idea what I'm writing here, of course, but he's helped me become a more caring and mature person.

To my parents, my wife, my mentors, my peers, and my chinchilla.

Chapter 1

Introduction

1.1 Quantum nature of chemical reactions

Quantum effects play a fundamental and profound role in chemical reactions. These effects are particularly evident at low temperatures or near energetic thresholds. In addition, the wave-like nature of matter gives rise to coherence and interference phenomena that have no classical analogs. Together, these quantum behaviors influence chemical reaction rates, product yields and distributions, and the dynamics of intermediates in ways that classical theories cannot capture.

A primary manifestation of quantum mechanics in chemical processes is the phenomenon of tunneling. Quantum tunneling allows particles with insufficient energy to pass through potential energy barriers, as a consequence of their wave-like nature. This enables classically forbidden chemical reactions to occur, significantly

enhancing reaction rates and altering product distributions, especially for reactions at low temperatures. Among all chemical species, hydrogen, due to its low mass and correspondingly delocalized wavefunction, exhibits a high probability for tunneling and has been widely studied. Hydrogen tunneling plays a crucial role in acid-base reactions [1], atom transfer processes involving organic species [2, 3], and enzymatic oxidation-reduction reactions [4, 5]. Although tunneling of heavier chemical species is less common, it can still influence certain organic chemical reactions [6, 7].

Another key quantum effect in chemical reactions is the presence of quantized energy levels. Because both reactants and products occupy discrete quantum states, a reaction channel only becomes accessible when the total collision energy exceeds the threshold of the product state. At low temperatures, this leads to the emergence of the Wigner threshold laws [8], where the reaction cross-sections exhibit sharp on and off behavior as new partial waves become accessible. Additionally, shape and Feshbach resonances can arise from the quantized energy levels when the metastable states lie close to the dissociation limit. These resonances, observed across many experimental platforms, ranging from molecular beams [9, 10] to laser-cooled atoms and molecules [11], can create dramatic enhancements in elastic, inelastic, and reactive cross-sections that vastly alter the collision and chemical dynamics [12, 13, 14, 15, 16].

When the quantum states of both reactants and products are well resolved, reaction dynamics can be described in terms of state-to-state reaction rates rather than a single bulk rate [17, 18]. Controlling the initial quantum state of the

reactants in a specific eigenstate, or a coherent superposition, allows for steering the reaction towards particular product channels. Experimentally, it requires quantum-state-resolved detection of reaction products, a capability that has been demonstrated in beam experiments such as $Ar^+ + N_2$ [19] and $O + H_2$ [20] reactions. The KRb + KRb reaction studied in our work also falls into this category, where reactant and product states can be precisely prepared and probed.

Coherence and interference effects, distinctive to quantum mechanics, also manifest in chemical reactions and can significantly influence the dynamics. When multiple reaction pathways contribute to a product channel, the interference between these pathways can enhance or suppress reaction rates. This interference can bias the formation of products towards specific quantum states. Early demonstration of such coherence effects was observed in photochemical processes, including photo-association [21], photo-ionization [22], and photo-dissociation [23, 24]. In these processes, one could leverage quantum coherence to optimize product yield and control reaction pathways.

In the context of reactive scattering settings, coherent control of product state distribution has been proposed using interferences between reaction pathways [25, 26]. For light molecules such as HD, HF, and D_2, interference effects have been experimentally confirmed in molecular beam experiments [27, 28, 29].

Spins, an intrinsically quantum mechanical property, also play a significant role in determining the outcomes of chemical reactions. Along with electronic states, spin states determine the electronic potential energy surfaces on which chemical

dynamics happen. Spins can provide or restrict access to certain reaction pathways, and drastically affect the efficiency of chemical processes [30, 31, 32]. For instance, a change in total spin multiplicity, such as from singlet to triplet, may be forbidden unless mediated by spin–orbit coupling, requiring the reaction to transition between potential energy surfaces [33, 34].

While the role of electronic spin in reaction dynamics is extensively explored, nuclear spins can also influence reaction outcomes, but have not been studied as much. In reactions producing homonuclear molecules, symmetry-based nuclear spin selection rules restrict which spin configurations are allowed in the products. These rules can lead to strong state-to-state propensities or even complete suppression of certain reaction channels [35, 36]. Furthermore, when electronic and nuclear spins are strongly coupled, as in radical pair systems, singlet to triplet conversion can be induced by hyperfine interactions [37, 38]. Such spin dynamics give rise to magnetic field sensitivity in reaction yields and rates, enabling external control over chemical reactivity.

Additionally, quantum effects play a crucial role through non-adiabatic processes, where transitions between different potential energy surfaces occur during a reaction. A prominent example is the breakdown of the Born–Oppenheimer approximation, which assumes that nuclear and electronic motions can be separated [39]. This approximation fails when two potential energy surfaces of the same spin multiplicity become degenerate or nearly degenerate, allowing nuclear motion to induce transitions between them. Such regions of degeneracy, known

as conical intersections, serve as gateways for non-adiabatic transitions and are central to determining the branching ratios and quantum yields of photochemical reactions [40, 41, 42].

In this thesis, we investigate the manifestation of quantum effects in the ultracold bimolecular reaction $KRb + KRb \rightarrow K_2 + Rb_2$, utilizing state-sensitive detection to quantify the reaction products. This approach enables direct observation of quantum tunneling effects on reaction rates and product yields in specific quantum channels. Signatures of quantum coherence and interference are imprinted in the product state distributions, revealing the surprising preservation of coherence even in a reaction considered chaotic and ergodic, characterized by a mostly statistical outcome [43]. Additionally, we investigate the role of spin in short-range atom-molecule interactions through KRb + Rb collisions. Our findings suggest that electronic spin couples to mechanical degrees of freedom, substantially modifying the collision dynamics and outcomes. This coupling is further enhanced by the presence of two intersecting potential energy surfaces, forming a conical intersection that facilitates the effects of the spin-rotation interaction.

1.2 Going ultracold

Experimental observation of quantum effects in chemical reactions often requires access to low-temperature regimes. Studying chemical reactions in crossed or merged molecular beam experiments enables one to avoid thermal averaging, which can mask

the underlying quantum phenomena at higher temperatures. When reactant beams are cooled to temperatures of just a few Kelvins, or even down to milliKelvin via buffer-gas cooling [44, 45, 46], Stark and Zeeman deceleration [47, 48], the resulting collision energies are confined within a narrow window. In this regime, only a few rotational, vibrational, and partial-wave channels remain energetically accessible, enabling high-resolution studies of quantum-state-specific dynamics. The relevant energy scales are shown in Fig. 1.1.

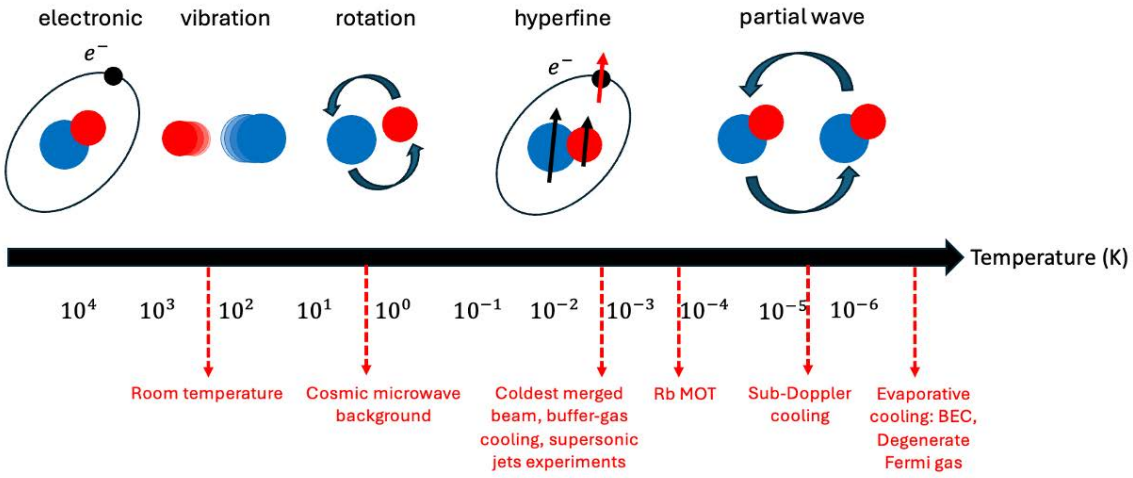

Figure 1.1: A molecular thermometer that displays the energy scales of relevant degrees of freedom in molecules, expressed in units of Kelvin (K).

Moreover, these platforms typically offer precise control over external electric and magnetic fields, as well as the ability to prepare and select specific quantum states of the reactants. This level of control is essential for implementing coherent

control strategies and for probing the fundamental role of quantum interference, tunneling, and resonance effects in chemical reactions.

An alternative approach to accessing low temperatures is through laser cooling of atoms and molecules, which routinely achieves sub-milliKelvin temperatures. When combined with evaporative cooling, this technique can further lower the temperature to the sub-microKelvin regime for certain atomic and molecular species, enabling the creation of Bose–Einstein condensates and Fermi-degenerate gases [49, 50, 51]. In this ultracold regime, the quantum states of the reactants, including rotational, vibrational, partial-wave, and even hyperfine levels, are well defined and highly controllable.

Moreover, thermal motion is drastically suppressed at such low temperatures, allowing quantum mechanical effects to govern reaction dynamics fully. These unique conditions make ultracold atoms and molecules an ideal platform for experimentally testing quantum chemistry predictions and exploring fundamental quantum effects with unprecedented precision.

1.3 Choosing KRb molecules

With the goal of understanding quantum effects in chemical reactions, we choose potassium–rubidium (KRb) molecules as our species of interest. The choice was a historic continuation of previous attempts to create a dense Fermionic dipolar gas, which surprisingly turned out to be a good platform to study ultracold chemical

reactions, as KRb offers several compelling advantages. First, the techniques for laser cooling, magnetic and optical trapping, and evaporative cooling of alkali atoms have been well established for three decades. Building on this solid foundation, coherent molecule association methods developed over the past two decades [52, 53, 54, 55, 56] now enable the routine production of ultracold ensembles of bialkali molecules, including KRb, at temperatures below $1\mu K$.

While many bialkali species share similar chemical properties, only a subset supports the energetically allowed double exchange reaction $\mathrm{AB} + \mathrm{AB} \rightarrow \mathrm{A_2} + \mathrm{B_2}$. Notably, this reaction is exothermic for just a few combinations, and KRb stands out among them. Most other reactive bialkali species involve lithium, which is comparatively more challenging to cool and manipulate.

Another practical advantage of KRb lies in the modest energy release (approximately 10 cm^{-1}) associated with its exothermic reaction $\mathrm{KRb} + \mathrm{KRb} \rightarrow \mathrm{K_2} + \mathrm{Rb_2}$. This energy allows only a limited number of rotational states to be populated in the products, therefore restricting the number of accessible exit channels. This makes it experimentally feasible to resolve and quantify the complete distribution of product states.

Another advantage of choosing KRb is the availability of the fermionic isotope ^{40}K. Among all alkali atoms, only ^{40}K and ^{6}Li are stable fermions (while ^{40}K is technically radioactive [57], its half-life exceeds a billion years, making it effectively stable for experimental purposes). By pairing fermionic ^{40}K with bosonic ^{87}Rb, one obtains a fermionic $^{40}\mathrm{K}^{87}\mathrm{Rb}$ molecule that is relatively unique among all bialkali

species.

Fermionic bialkali molecules offer key advantages for studying chemical reactions, particularly in the ultracold regime. When prepared in a single quantum state, two-body collisional loss is strongly suppressed due to exchange symmetry constraints, which forbid s-wave scattering between identical fermions. As a result, only p-wave collisions (and higher partial waves, which are negligible) contribute, and these are suppressed at ultracold temperatures by the centrifugal barrier [52]. Consequently, reactive collisions can proceed only via quantum tunneling through the barrier, greatly reducing loss rates. The suppression of collisional losses significantly enhances the stability and lifetime of the KRb molecular ensemble, allowing for the control of the initial quantum state and the accumulation of statistically significant measurements of the reaction products over a more extended period.

By choosing KRb molecules as our experimental platform, we also gain access to atom–molecule collision and reaction studies at no additional cost, by utilizing the residual K or Rb atoms after molecular association. This is shown in Fig. 1.2. Among these two atomic species, collisions between K and KRb are reactive, resulting in molecular loss [58], while Rb + KRb collisions are not expected to support chemical reactions. Investigating both systems offers valuable insight into the reaction dynamics. On the theoretical side, advances in quantum dynamics calculations have enabled the quantitative prediction of the outcomes of K + KRb reactions [58]. In contrast, Rb + KRb collisions exhibit unexplained two-body losses [59], the underlying mechanisms of which remain poorly understood. Understanding these

losses is a key objective of this thesis. Furthermore, incorporating both atoms and molecules within the same experimental apparatus opens the door to exploring hybrid quantum systems, such as dipolar interactions between KRb molecules and Rydberg atoms. This can be achieved by optically exciting either the K or Rb atom to a Rydberg state, enabling the study of long-range, tunable interactions between polar molecules and highly excited atoms.

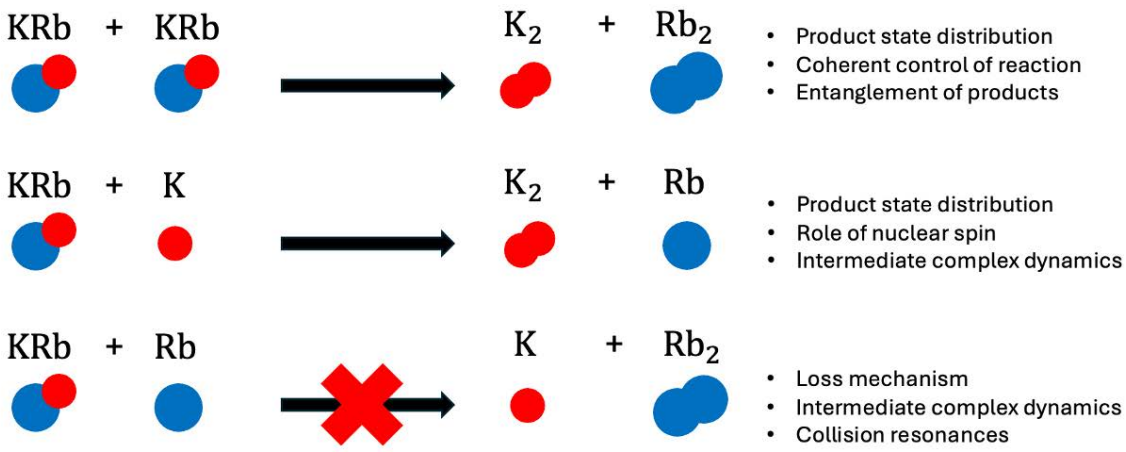

Figure 1.2: Three distinct collisions or reactions that can be studied within our KRb-based experimental platform, each offering insight into different quantum chemical dynamics.

1.4 This thesis

The content of this thesis is organized as follows: Chapter 2 provides an overview of the experimental apparatus and procedures used to produce and control ultracold KRb molecules. Chapter 3 describes the detection methods employed to probe reaction outcomes, including absorption imaging and ionization-based techniques. In Chapter 4, we present studies of ultracold atom–molecule collision complexes and characterize inelastic collisional losses, as well as their dependence on external fields. Chapter 5 focuses on the observation of quantum interference between chemical reaction pathways, revealed through state-selective ionization detection of the products. We also propose a coherent control scheme that leverages such interference effects. In Chapter 6, we investigate long-range dipolar interactions between KRb molecules and Rydberg Rb atoms, demonstrating resonant energy exchange between the two species. Chapter 7 revisits atom–molecule collisions, now with Rb atoms prepared in an excited hyperfine state. We report on the observation of hyperfine-to-rotational energy transfer and compare our results with theoretical predictions, shedding light on the role of short-range interaction physics. Finally, Chapter 8 outlines possible future research directions and highlights some open questions of interest to the broader communities of ultracold chemistry and physics.

Chapter 2

Production and control of an ultracold KRb gas

2.1 Overview of the experimental apparatus

With the goal of creating a sample of ultracold KRb molecules and Rb atoms, an experimental apparatus integrating techniques from both atomic physics and physical chemistry was constructed. The initial system build began nearly ten years ago and was primarily carried out by the previous generation of graduate students and postdoctoral researchers in the KRb experiment. While most of the construction details can be found in Dr. Yu Liu's thesis [60], I will highlight the key components of the apparatus and the major modifications made in my graduate career in this thesis.

The experimental setup spans three optical tables within a single laboratory room: the machine table, the laser table, and the Rydberg table. The laser table houses all lasers used for laser cooling, trapping, and imaging of Rb and K atoms, as well as lasers responsible for coherent molecular association. The machine table houses the mechanical components of the main experimental apparatus, comprising four interconnected vacuum chambers and magnetic coils surrounding some of them. Two pulsed 532 nm lasers and a continuously tunable dye laser, along with optical delivery paths, microwave waveguides, and antennas, are also mounted onto the machine table. Finally, a complete Rb Rydberg excitation laser system is built on the Rydberg table. This system, developed more recently (2021–2023), enables both Rydberg excitation and state-selective ionization detection of Rb atoms. Further details on the Rydberg setup will be discussed in Chapter 6 of this thesis.

2.2 MOT chamber: Creation of cold Rb and K atom clouds

The first step in creating an ultracold KRb gas is to simultaneously accumulate a large number of cold Rb and K atoms at low temperatures. This is achieved using a spatially overlapping dual-species magneto-optical trap (MOT) inside the MOT chamber. The MOT chamber is actually a relatively large glass cell, with K and Rb sources located at one end in four protruding arms. Connections to the evaporation chamber can be found at the other end.

Inside the protruding arms of the MOT cell, two sets of Rb dispensers, each consisting of three dispensers, were installed. In the early stages of the experiment, these dispensers were briefly fired at relatively high currents (4.0–4.5 A) for 10–15 minutes [60]. These initial firings deposited sufficient Rb atoms onto the glass cell walls to sustain efficient MOT loading for an extended period. From 2021 to 2024, however, we observed a gradual decline in the number of post-evaporation Rb atoms, suggesting a depletion of residual Rb inside the chamber. In response, we fired one set of the Rb dispensers for two hours at 2.45 A. Interestingly, this initially led to a threefold increase in the Rb MOT fluorescence signal, but the post-evaporation Rb atom number in the QUIC trap dropped to nearly zero. We speculated that the drop was caused by increased background collisions with unwanted gas species produced during the dispenser firing. After approximately one week of continuous pumping in the MOT cell, the post-evaporation Rb numbers recovered and slightly exceeded their previous values. Throughout this process, the ion pump reading for the MOT cell remained below the detection limit (1×10^{-10} Torr) and showed no measurable change.

The K atom sources are contained in two sealed glass ampoules housed inside copper tubes attached to the protruding arms. One ampoule contains 50 mg of ^{40}K enriched to 3.15%, and the other contains 25 mg enriched to 7%. To release K atoms, one of the ampoules was cracked inside the copper tubes and heated with heat tapes. Over time, the K atoms migrated throughout the glass cell, meaning that we could no longer independently control the K and Rb vapor pressures without

additional Rb dispenser firings or opening up the other ampoule.

Prior to 2024, the MOT cell was heated to approximately 40°C, and the active K ampoule was maintained above 50°C to sustain a sufficiently high alkali vapor pressure. However, we later found that such heating was unnecessary. As part of preparations for a major electrical shutdown, we removed all power supplies related to MOT cell heating without negatively affecting the number of atoms or molecules. This change eliminated the risk of overheating from potential linear power supply failures, where output voltages could rail to 50 V and cause severe damage to the glass cell.

Another key component of the MOT setup is the generation of MOT laser beams. For Rb, we use two distributed Bragg reflector (DBR) lasers at 780 nm: one for the cooling transition and one for the repump transition. The repump laser is locked to the $|F = 1\rangle$ to $|F' = 1, 2\rangle$ crossover peak of the Rb D_2 line with saturated absorption spectroscopy and then frequency-shifted up by approximately 78.45 MHz with an Acoustic-optical modulator (AOM) to match the required repump frequency for Rb atoms.

The cooling laser is referenced to the repump laser via an optical phase-locked loop (PLL) setup. The two laser beams are combined onto a fiber-coupled fast photodetector, capable of detecting beat signals up to tens of GHz. The beat note is amplified and sent to a phase-frequency detector board (ADF 4159), where it is compared with a frequency-controlled RF reference. The resulting phase-frequency difference is encoded into an error signal, which is fed back to the cooling laser. By

adjusting the reference RF frequency (using an FPGA-controlled DDS channel), we can dynamically tune the frequency difference between the cooling and repump lasers by a few hundred megahertz continuously in the experimental sequence.

To generate the MOT beams, the cooling and repump lasers are combined using a non-polarizing beamsplitter and seeded into a tapered amplifier (TA), producing amplified light at both frequencies. Notably, we also employ a fiber-based electro-optic modulator (EOM) to modulate the cooling laser and generate a sideband as a second repump frequency, which typically results in a 10% increase in the Rb atom number after RF evaporation. So far, we do not fully understand why this scheme outperforms the case with a single repump frequency.

In addition to the MOT beam path, small portions of the cooling and repump lasers are split off for Rb absorption imaging and optical pumping. For imaging, the cooling laser is tuned to the $|F = 2\rangle$ to $|F' = 3\rangle$ cycling transition. Both cooling and repump lasers are also used for optical pumping to purify the atomic hyperfine states before further experimental steps.

For K, we employ three DBR lasers operating at 767 nm. Due to the low natural abundance of ^{40}K (0.012%), it is challenging to directly lock a laser to the ^{40}K transitions. Instead, we dedicate a master laser referenced to the crossover between the $|F = 1, 2\rangle$ ground states and the unresolved excited states of ^{39}K. The cooling and repump lasers for ^{40}K are then phase-locked to the master laser using techniques similar to those described for the Rb system.

To generate the K MOT beams, we combine the cooling and repump light and seed them into a TA. Because the same fiber ports are used for both K MOT beams and gray molasses beams, an AOM is employed to combine the first-order diffracted MOT light with the zeroth-order transmitted gray molasses light. An independent mechanical shutter controls the gray molasses path, allowing us to switch the K MOT and gray molasses beams on and off independently, which is critical for achieving sub-Doppler cooling of K atoms.

Similar to the Rb system, a portion of the cooling and repump light is split off for K optical pumping and absorption imaging. However, a key difference for K is that we must use the cooling laser for imaging at low magnetic fields and the repump laser for imaging at high magnetic fields. This distinction (compared to the Rb system) arises because one of the required imaging frequencies lies above the master laser frequency, while the other lies below, and it is not possible to continuously ramp the phase lock frequency across zero.

Each experiment typically begins with the MOT loading stage. To enhance loading, we first illuminate the MOT glass cell with a UV LED for 1.5 seconds, which desorbs deposited alkali atoms from the cell walls and increases the vapor pressure. This step increases the MOT loading rate at the expense of temporarily raising the background pressure. To mitigate the negative effects, we hold the atoms in the MOT for an additional 5 seconds, allowing the background pressure to decrease.

Following MOT loading, we apply a MOT compression stage (CMOT) by red-detuning the repump laser by 7.5 MHz. This reduces radiation pressure,

allowing the MOT to shrink in size and minimizing heating during transfer into the quadrupole trap for evaporative cooling. Since the K MOT is much smaller, compression is not necessary for K.

After the Rb CMOT, we perform molasses cooling for both Rb and K atoms. While the general procedures are described in Yu Liu's thesis [60], the gray molasses setup for K needs particular attention. Prior to 2024, the gray molasses system used a DBR laser as the seed light, with two double-pass AOM setups generating the cooling and repump frequencies. These frequencies were recombined before being seeded into a TA, similar to the MOT beam generation setup. However, the frequency stability of the DBR degraded over time, leading to frequent unlocking events, and the TA power output also dropped significantly.

In 2024, we replaced the entire gray molasses laser system with a fiber laser setup following the locking scheme described in William Tobias's thesis on the JILA KRb experiment [61]. Our updated optical layout is shown in Fig. 2.1. The new fiber laser, manufactured by UltraQware (now Qtek), is frequency-doubled from 1540 nm and provides up to 2 W of output power at 767 nm. A resonant EOM (QUBIG) operating at 1286 MHz, corresponding to the hyperfine splitting between the $|F = 9/2\rangle$ and $|F = 7/2\rangle$ states of ^{40}K, is used to create the cooling and repump sidebands.

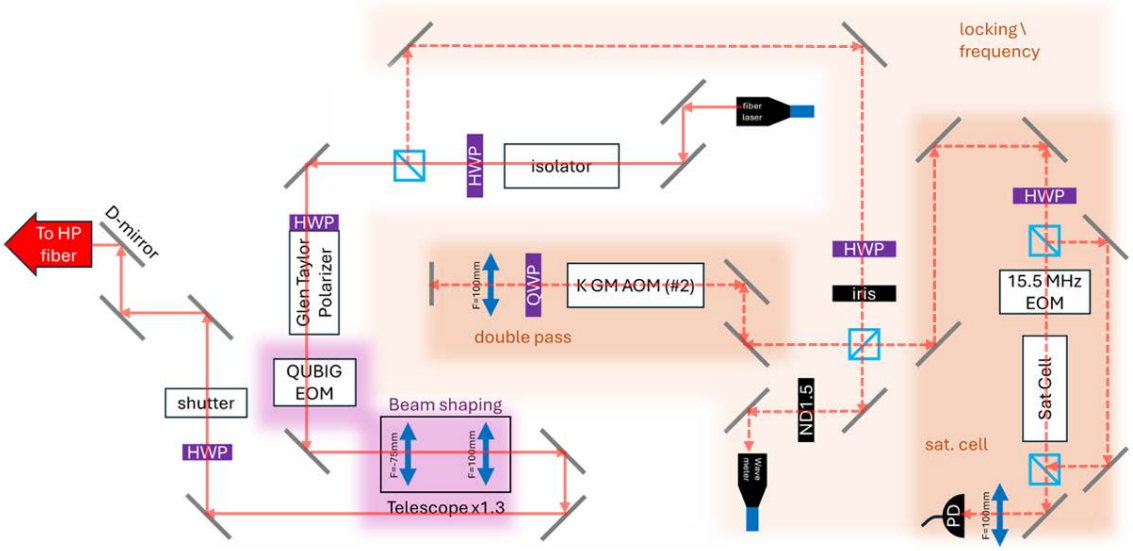

Figure 2.1: Optical layout for the new gray molasses system. Solid arrows represent the main branch, which delivers most of the power to the machine table. It's combined with the K MOT beams on an AOM similar to the old gray molasses setup (with the DBR + TA). Dashed arrows represent the locking and monitoring beam paths.

Since stronger cooling is required relative to the repump, we set the carrier frequency to the cooling transition. The carrier is shifted down using a double-pass AOM setup to reach the $4^2S_{1/2}\ |F = 1, 2\rangle$ to $4^2P_{1/2}\ |F' = 2\rangle$ crossover transition of ^{39}K for laser locking.

Before transporting the K and Rb atoms to the next chamber for evaporative cooling, we perform optical pumping to prepare the atomic populations in their respective stretched trapping states, which are more deeply trapped. Proper optical pumping is crucial for maximizing transfer efficiency and optimizing subsequent

evaporation performance. It is important to note that the polarizations of the optical pumping beams are critical for achieving high pumping fidelity.

2.3 Evaporative cooling and transport of cold K and Rb atoms

We use a magnetic transport scheme to move the cold K and Rb atoms from the MOT cell to the next chamber, the evaporation chamber (also referred to as the QUIC chamber). In most ultracold atom experiments, it is critical to separate the atom loading region from the scientific study region, as effective MOT loading typically requires background pressures of 10^{-9}–10^{-8} Torr, which are too high to maintain a vacuum lifetime longer than 10 seconds for efficient evaporative cooling. In our setup, a differential pumping system separates the MOT cell from the rest of the apparatus, achieving a pressure difference of nearly two orders of magnitude.

Magnetic transport is implemented by physically moving the MOT coils along a 1-meter-long track. During this process, we first ramp up the current in the MOT coils to 340 A to create a tightly confined magnetic trap, and then accelerate the coils, mounted on a cart, along the track. The cart temporarily slows down near the midpoint, where a large stationary magnet is located. It accelerates again toward the end of the track and decelerates gradually to a complete stop at the evaporation chamber location. The entire transport sequence takes approximately 1 second.

It is known that the single-pass transport efficiency is about 25%, with most atom loss occurring early in the acceleration phase inside the MOT cell [60], prior to entering the differential pumping section. This is expected, given the higher background pressure in the MOT region. We note that a track-based magnetic transport scheme may not offer the best performance in terms of efficiency and speed. Future improvements could involve replacing the cart transport system with a stationary array of quadrupole coils, allowing for faster and more efficient transport [62].

After the K and Rb atoms arrive in the evaporation chamber, they are transferred into a fixed, more tightly confined quadrupole trap for evaporative cooling. Tighter trapping is preferred at this stage to enhance collision rates between atoms, improving the efficiency of evaporation.

In our scheme, we perform evaporation exclusively on Rb atoms (which are more abundant), while K atoms are sympathetically cooled and act as a heat load in the system. We employ an RF-induced evaporation technique [63] to selectively remove hot Rb atoms from the cloud. The RF signal is generated by a dedicated DDS channel, amplified using a high-power amplifier (LZY-22+, Mini-Circuits), and coupled to the atoms through the Ioffe coil. The RF drive induces transitions from the initial $|2, 2\rangle$ low-field-seeking state through a cascade of m_F-changing transitions until atoms reach anti-trapped states ($|2, -1\rangle$ and $|2, -2\rangle$) and are subsequently expelled from the trap.

To preferentially remove higher energy atoms first, we begin evaporation with

an RF frequency of 30 MHz (corresponding to atoms with large kinetic energies that can access higher magnetic field regions) and gradually ramp down to 15 MHz. At this stage, as the cloud becomes colder and denser, losses due to Majorana spin flips at the trap center become significant [64]. To mitigate this, we turn on the Ioffe coil to create a finite magnetic field minimum [65]. Evaporation is then continued by exponentially ramping the RF frequency down to near 2 MHz.

The full evaporation sequence typically lasts 10 to 20 seconds, with the time constants and RF amplitudes for each ramp segment treated as free-tuning parameters. In 2023, we explored the use of a machine-learning-based optimization algorithm (M-LOOP) [66], designed to optimize experimental performance by efficiently navigating high-dimensional parameter spaces. The M-LOOP results were consistent with our manual optimizations, suggesting that the evaporation process is already near optimal given current hardware constraints.

It is worth noting that the RF evaporation scheme can leave a fraction of atoms in the $|2,1\rangle$ state during the process and at the end of the evaporation, as confirmed by a Stern-Gerlach experiment in the evaporation chamber. Both the temporary presence during evaporation and the residual atoms post-evaporation can lead to inelastic collision losses.

Ideally, a microwave evaporation scheme targeting the $|2,2\rangle \rightarrow |1,1\rangle$ transition would be preferable, as atoms transferred to the $|1,1\rangle$ state are immediately anti-trapped and expelled. In 2021, we briefly explored the use of microwave evaporation. However, its performance was limited by the available microwave power

inside the evaporation chamber. We suspect that poor microwave coupling efficiency to the atomic cloud is the primary limiting factor. In the future, performance could potentially be improved by employing a more powerful microwave amplifier (exceeding 20 W) and replacing the microwave waveguide.

	RF evaporation	**Microwave evaporation**
K present	5.0×10^6 Rb + 1.4×10^6 K	1.4×10^6 Rb + 1.0×10^6 K
Rb only	1.1×10^7 Rb	6.4×10^6 Rb

Table 2.1: Performance comparison between microwave evaporation and RF evaporation. In these measurements, RF evaporation was performed using optimized parameters, while microwave evaporation used the maximum available amplitude at all stages to maximize performance. The post-evaporation temperatures of both Rb and K atoms are slightly lower for RF evaporation.

A minor but important point is that the RF evaporation process generates significant RF noise in the 2–30 MHz range throughout the lab during evaporation. This noise can even be detected on grounded surfaces, such as the laser table. The resulting interference can cause RF rectification, affecting the performance of temperature servos. Simultaneously, RF pickup on electric cables impacts EOM modulation if not properly shielded.

The most noticeable consequences are: (1) temperature servo setpoint drifts due to RF rectification, leading to laser frequency drifts if fast feedback mechanisms are not employed, and (2) loss of error signals for saturated absorption vapor cell locks

and cavity Pound-Drever-Hall (PDH) locks when the RF evaporation frequency approaches the modulation frequency.

To mitigate the second problem, we identify the resonant frequencies of the affected EOMs and modify the RF evaporation sequence to skip neighboring frequencies during the evaporation ramp.

After the RF evaporation, we transfer the K and Rb atoms to the science chamber using a transport optical dipole trap (TODT). The TODT is formed by a 1064 nm laser beam whose focus can be translated between the evaporation chamber and the science chamber. This is achieved by mounting a lens on an air-bearing stage, which can be programmed to move smoothly with little friction or hysteresis.

The TODT power is controlled via an AOM with active feedback for intensity stabilization. Typically, we load the K and Rb atoms from the QUIC trap into the TODT at the maximum available laser power, approximately 4 W. The transport process takes less than 1 second, and we achieve a transfer efficiency of about 50% for both species. Since the TODT power is very high, careful consideration must be given to thermal effects on the AOM to maintain constant total RF power throughout operation. Prior to 2021, the entire TODT beam path was in free space, making it sensitive to air currents and thermal fluctuations. During this period, the TODT transport efficiency was 50–60%, and we suspected that environmental sensitivity was a major limiting factor.

To address this, we implemented a high-power-handling photonic crystal

fiber (PCF) to reduce the free-space path length. In the new beam path, the AOM used for intensity control was placed before the PCF, such that thermal fluctuations now primarily lead to intensity instability (which can be actively suppressed by the intensity servo) rather than beam pointing noise. Additionally, the free-space path length after the fiber was reduced by approximately a factor of two, decreasing sensitivity to air currents. However, despite these upgrades, no significant improvement in TODT transport efficiency was observed, suggesting that the dominant atom loss originates from other sources.

After transferring the K and Rb atoms to the science chamber, we load them into the horizontal optical dipole trap (HODT), which nearly co-propagates with the TODT. We then perform quantum state preparation for molecule association, which requires Rb atoms to be in the $|1,1\rangle$ state and K atoms in the $|9/2,-9/2\rangle$ state.

To achieve this, Rb atoms are transferred via a microwave adiabatic rapid passage (ARP) pulse, while K atoms undergo a cascade of m_F-changing transitions at a magnetic field of $B = 25.8$ G. After the state preparation, any residual Rb atoms remaining in the $|2,2\rangle$ state are removed by applying a resonant blast pulse using a Rb imaging beam, targeting the $|F = 2, m_F = 2\rangle \rightarrow |F' = 3, m_{F'} = 3\rangle$ transition. Following state preparation, we ramp up the magnetic field using the Feshbach coils to $B = 550$ G, which is slightly above the Feshbach resonance used for molecule association. At this magnetic field, the Rb–K collision cross section is enhanced, allowing for more efficient evaporative cooling compared to evaporation at lower magnetic fields.

Finally, before molecule association, we perform ODT evaporation by gradually ramping down the intensity of the HODT in the presence of a vertical ODT (VODT), which provides confinement along the loosely trapped HODT axial direction. This configuration allows the cloud to remain mostly trapped while selectively removing atoms with the highest energies.

At the end of the ODT evaporation stage, we obtain a mixture of K and Rb atoms co-trapped in the combined trap of the HODT and VODT (commonly referred to as the crossed-ODT, or XODT) at a temperature near $T = 500$ nK. As of the completion of this thesis (2025), we typically achieve atom numbers of approximately 1.0×10^5 for both K and Rb at this stage.

This number is lower than what was achieved prior to 2021, where about 1.5×10^5 atoms per species were obtained. The reduction is attributed to a major HVAC shutdown event in the summer of 2021, which impacted many parts of the experimental setup. Despite thorough checks of the system, we have not been able to fully recover the previous K and Rb atom numbers.

2.4 Coherent association of KRb molecules

In this step, we create ground state KRb molecules through a two-step process: first, magneto-association into weakly bound Feshbach molecules, followed by a two-photon stimulated Raman adiabatic passage (STIRAP) transfer into the rovibronic ground state. This molecule creation scheme is highly efficient, fully

coherent, and prepares nearly all KRb molecules into the same quantum state.

Magneto-association is performed by ramping the magnetic field from $B = 550$ G to $B = 544.0$ G across the Feshbach resonance of ^{40}K and ^{87}Rb located at $B_0 = 546.7$ G, with a typical ramp rate of 10 G/ms. The ramp rate is a tunable parameter that can be optimized to maximize the number of Feshbach molecules. During this process, the magnetic field sweeps adiabatically, converting atom pairs from the open channel configuration (Rb in $|1, 1\rangle$ and K in $|9/2, -9/2\rangle$) into a weakly bound molecular state in the closed channel (Rb in $|1, 0\rangle$ and K in $|7/2, -7/2\rangle$).

Typically, we achieve a Feshbach conversion efficiency of approximately 15–20%. The number of Feshbach molecules and their lifetimes can be measured by performing decay measurements, where we wait for a few milliseconds after the magnetic field ramp and monitor the drop in the Rb absorption signal, which represents the number of Feshbach molecules.

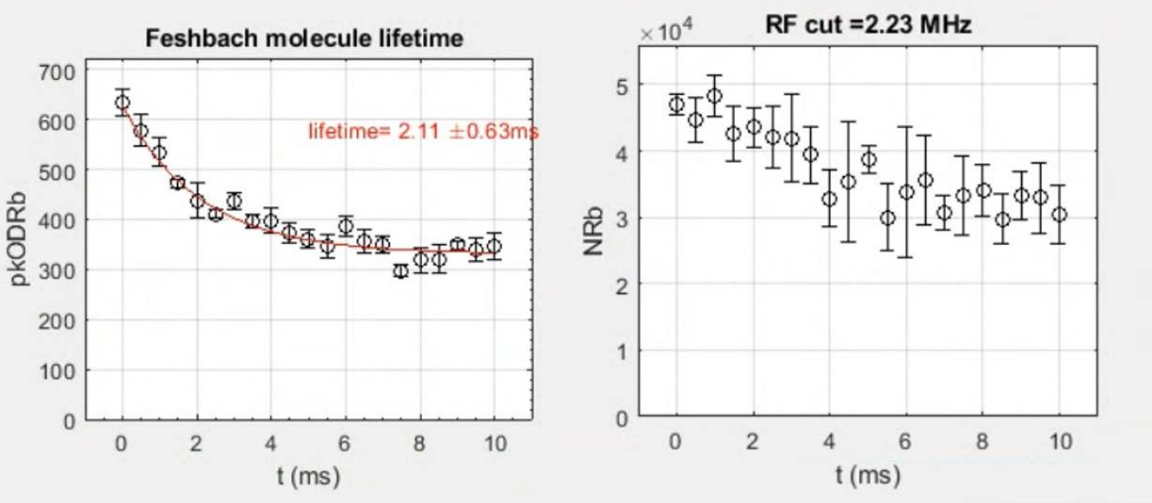

Figure 2.2: Measurement of Feshbach molecule number and lifetime. The exponential decay time constant extracted from the left panel corresponds to the lifetime of Feshbach molecules. In the right panel, the difference in Rb atom number (N_{Rb}) between $t = 0$ ms and $t = 10$ ms reflects the number of Feshbach molecules. From this measurement, approximately 2×10^4 Feshbach molecules are formed.

Due to the short lifetime of Feshbach molecules, it is crucial to transfer them to the rovibronic ground state as quickly as possible. However, residual K and Rb atoms also contribute to Feshbach molecule loss due to collisions, and removing them from the system requires additional time. To balance the competing demands of rapid transfer and atom removal, we implemented a fast removal scheme for the residual Rb atoms. Specifically, we apply a fast microwave ARP pulse for 0.75 ms to transfer the remaining Rb population from the $|1, 1\rangle$ state to the $|2, 2\rangle$ state, as opposed to a typical ARP duration of 4-10 ms in other parts of the experimental

sequence. Immediately afterward, a resonant blast of light targeting the $|2,2\rangle$ to $|3,3\rangle$ transition is used to expel the $|2,2\rangle$ atoms from the trap. Because the 0.75 ms pulse duration is too short to fully satisfy the adiabatic condition for ARP, the overall removal efficiency is limited to approximately 50%.

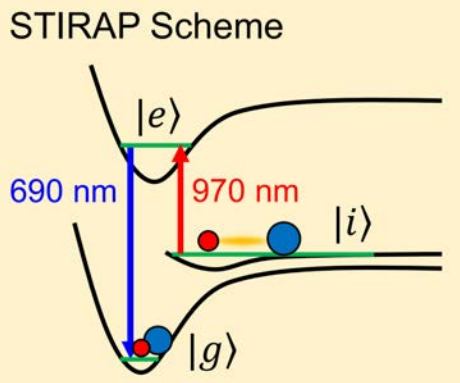

Figure 2.3: Schematic of the STIRAP process [60]. The molecules start in the loosely bound Feshbach state $|i\rangle$. A STIRAP pulse sequence adiabatically transfers the molecular population to the rovibronic ground state $|g\rangle$, without populating the intermediate excited state $|e\rangle$, provided that the adiabatic condition is satisfied.

Immediately after removing the residual Rb atoms, we apply the STIRAP pulse to transfer the weakly bound KRb molecules to the rovibronic ground state. The STIRAP process couples the weakly bound state in the $|a^3\Sigma^+, v = -2\rangle$ potential to the rovibronic ground state $|X^1\Sigma^+, v'' = 0\rangle$ via an intermediate state $|2^3\Sigma^+, v' = 23\rangle$. Specifically, we select this intermediate state because it offers good vibrational wavefunction overlap with both the initial and final states, and because its electronic structure exhibits a mixture of singlet and triplet character, ensuring large Rabi

rates that facilitate efficient population transfer [52].

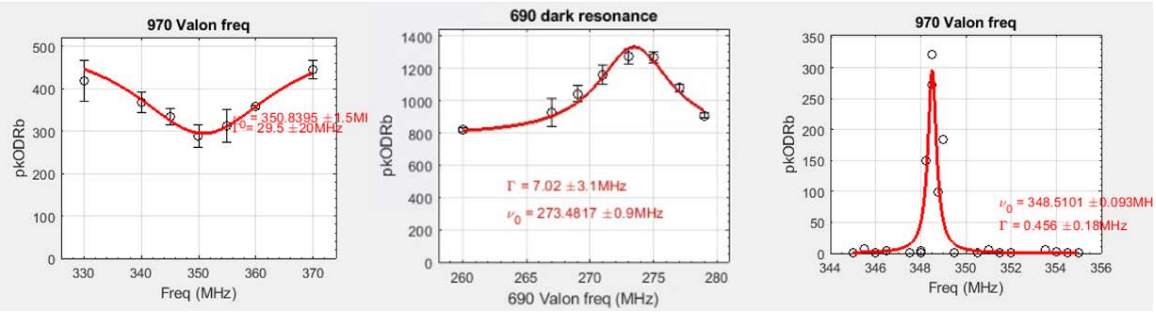

Figure 2.4: Spectroscopy scans of the STIRAP lasers to identify their respective resonance conditions. Left panel: Resonance scan of the 970 nm laser. Feshbach molecules are optically pumped to a wide range of final states when the 970 nm laser is resonant, resulting in a dip with a width on the order of 20 MHz near resonance. Middle panel: Dark resonance scan to determine the resonant condition for the STIRAP down leg (690 nm) laser. Right panel: Ground state molecule number as a function of two-photon detuning. In this measurement, we scanned the 970 nm laser frequency (due to its more stable lock compared to the 690 nm laser). The two-photon resonance condition is notably more stringent than the one-photon resonance condition for the 970 nm laser.

Prior to 2024, we utilized external cavity diode lasers (ECDLs) to generate both the 690 nm and 970 nm beams. At that time, we achieved approximately 8.5 mW (690 nm) and 27 mW (970 nm) of optical power on the machine table, measured after the fibers. However, the laser diodes gradually degraded over time, and by 2022, the 690 nm output power dropped below 6.5 mW. Additionally, the 690 nm ECDL

exhibited multiple stable operating regions near the locking setpoint as we tuned its current and piezo voltage. Although the cavity transmission modes and error signals appeared normal in nearly all modes, the molecule production performance varied dramatically between these regions, complicating system diagnostics and stability. Some of these modes were also unstable and would lead to unlocking events within a few minutes to an hour.

Based on these challenges, and after consulting with the JILA KRb experiment (which had transitioned to using a fiber-based 690 nm laser from Precilasers), we decided to replace the 690 nm ECDL with a fiber laser. We selected a 500 mW model that is sufficient for our experimental needs. In this system, the 690 nm output is generated by a sum-frequency generation (SFG) of a 1064 nm laser and a 1957 nm laser. Special care must be taken with the 1957 nm seed laser, as it can enter an unstable mode at certain current setpoints, destabilizing the lock. A typical solution is to reduce the operating current in steps of 0.1 A while monitoring the mode stability of the output.

We operate the fiber-based 690 nm laser at a total emission power of 100 mW, delivering 54.1 mW of optical power to the machine table. Following this upgrade, our STIRAP efficiency improved from 85% to 93%. It became significantly less sensitive to the PID parameters of the lock, likely due to the intrinsically low phase noise of the fiber laser.

After STIRAP, the final step in the molecule production sequence is the removal of residual K and Rb atoms. In this step, we apply a longer microwave ARP pulse

to transfer the remaining Rb atoms from the $|1,1\rangle$ state to the $|2,2\rangle$ state, and then use resonant imaging light for both Rb and K to blast the atoms out of the trap. This STIRAP atom removal process takes 5 ms, which is significantly longer than the earlier removal step after the Feshbach field ramp (0.75 ms), allowing the removal efficiency to approach nearly 100%.

In many experiments, it is desirable to retain some Rb or K atoms along with the KRb molecules in the XODT. For instance, to prepare a Rb + KRb mixture, we lower the microwave ARP amplitude that reduces the transfer efficiency from $|1,1\rangle$ to $|2,2\rangle$, so that a fraction of Rb atoms remain in the $|1,1\rangle$ state and are unaffected by the subsequent resonant removal beam. Similarly, a K + KRb mixture can be prepared by reducing the intensity of the removal beam targeting K atoms.

2.5 Microwave control of KRb molecules

After KRb molecules are created in the electronic and rovibronic ground state, they can be transferred into a wide range of hyperfine (nuclear spin) states and a few excited rotational states. This is primarily accomplished through a sequence of microwave pulses applied at different magnetic fields.

Specifically, we can populate various nuclear spin states in the ground rotational manifold ($N = 0$) via two-photon microwave transitions, access a series of hyperfine states in the $N = 1$ manifold through one-photon transitions, and reach selected states in the $N = 2$ manifold via two-photon processes as well. In principle, the Rb

microwave system can be used to excite KRb molecules to the $N = 3$ manifold. However, the state preparation fidelity in these cases is too low to be practically useful.

Because we work with microwave transitions under a range of magnetic and electric fields, it is often necessary to calculate suitable intermediate states and the corresponding microwave frequencies. To facilitate this, we use the MATLAB package Diatomix [67], developed by Arfor Houwman, a visiting student in our group in 2023. Diatomix offers a user-friendly graphical interface for calculating the energy levels of all hyperfine states of KRb molecules in their electronic and vibrational ground states, as well as the transition dipole moments connecting different hyperfine states, under arbitrary static electromagnetic fields and ODT intensities. This tool enables efficient identification of viable microwave transitions before experimental scans.

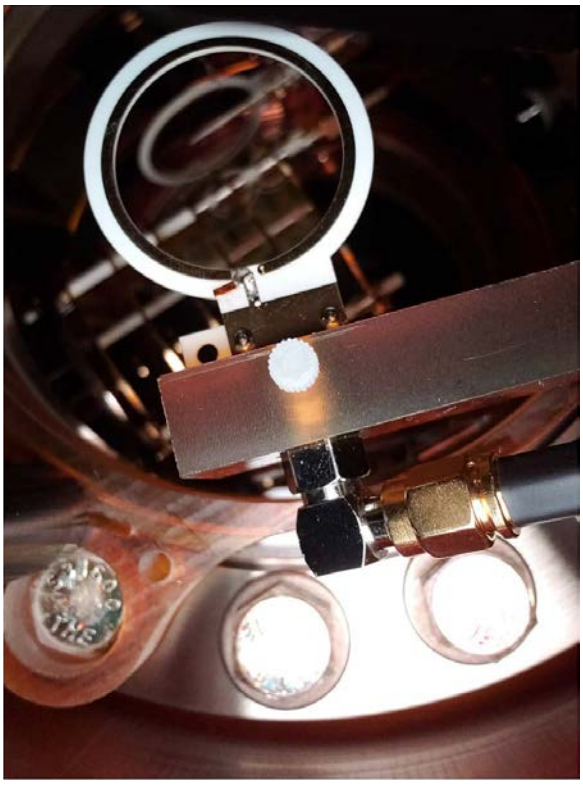

Figure 2.5: The $N = 1$ loop antenna mounted at the bottom of the science chamber. The photo was taken from underneath the chamber and facing upwards. A small copper piece was soldered to the loop to tune the antenna resonance for improved impedance matching.

Our microwave system is designed to excite KRb molecules up to the third rotational level $N = 2$. Two independent microwave circuits are employed for the $N = 1$ and $N = 2$ excitations. In the following section, we briefly introduce the two circuits.

The $N = 1$ microwave circuit is based on a DDS synthesizer (Valon Technology

5009) with two independent channels, each connected to an RF switch. The Valon DDS frequency is controlled via USB by the experiment control computer. Fast microwave switching is achieved by applying TTL signals to the RF switches. The outputs from the RF switches are then amplified by a 30 W amplifier (Mini-Circuits ZHL-30W-252-S+) and delivered to a loop antenna mounted at the bottom of the science chamber, as shown in Fig. 2.5.

It should be noted that controlling the Valon DDS synthesizer via USB introduces an unstable communication lag between 100–500 ms, making mid-sequence frequency changes impractical. Consequently, the frequency must be preset at the beginning of each experimental run.

At present, the $N = 1$ microwave system exhibits a mysteriously low coupling efficiency, manifested as the relatively slow Rabi rates on the order of 2–4 kHz, particularly when driving π transitions.

The $N = 2$ microwave circuit has a similar configuration: a Valon DDS synthesizer whose output is connected to an RF switch, and then amplified by a microwave amplifier (Mini-Circuits ZVE-3W-83+). The amplified signal is delivered to a loop antenna mounted on top of the science chamber, pointing downward at an angle, as shown in Fig. 2.6.

Interestingly, although the amplifier saturates at only 3 W output power, the observed Rabi rates for $N = 2$ transitions are significantly higher (50–100 kHz for σ_+) compared to those of the $N = 1$ system (10–20 kHz for σ_+). One possible

explanation is that the plate electrodes inside the vacuum chamber attenuate lower microwave frequencies more strongly, leading to reduced coupling efficiency for the $N = 1$ transitions.

Figure 2.6: The $N = 2$ microwave antenna mounted above the science chamber. The antenna is positioned at an angle to avoid obstructing the optical access for the ODT and ionization beams from above.

As mentioned earlier, frequency tuning and impedance matching of the microwave antennas are achieved by soldering a small copper piece near the antenna to alter its resonance pattern, as shown in Fig. 2.7. As the position of the copper piece is adjusted, the resonance dips, which are visible as sharp drops in the network analyzer reflection signal measurement, shift in frequency. The goal is to tune the configuration such that a substantial resonance dip appears at the desired operating

frequency.

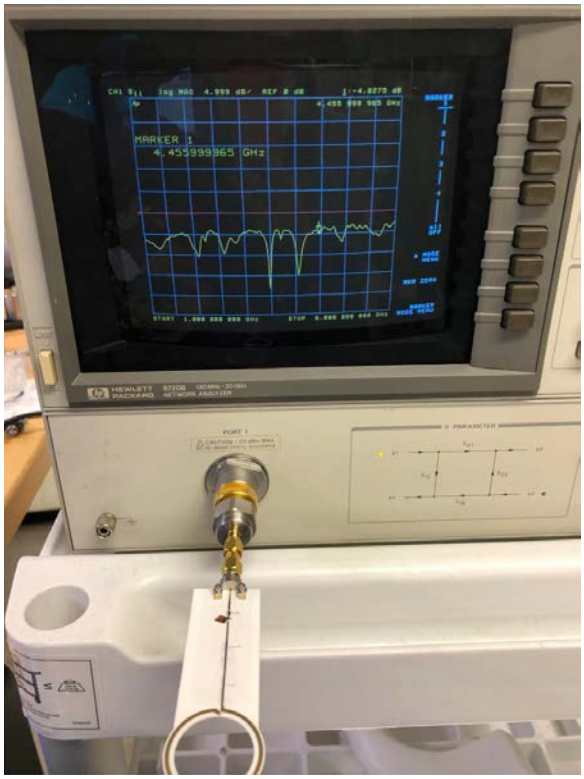

Figure 2.7: Testing the $N = 2$ microwave antenna using a network analyzer.

2.6 Laser frequency monitor and feedback with a wavelength meter

As briefly mentioned in previous sections, we employ a wavelength meter to monitor the frequencies of multiple lasers, using the measurements in a closed-loop feedback system for frequency stabilization. In this section, we elaborate further on the design

of this system.

Our wavelength meter, the Bristol 871A, features a fiber-coupled input and offers millisecond-level response time and sub-MHz-level precision of frequency reading for detecting visible to near-infrared lasers. Wavelength meters on the market typically fall into two categories. The first type, based on Fizeau etalons, offers superior precision, resolution, and fast measurement times, but can only detect one laser tone at a time. The second type, utilizing a Michelson interferometer, enables the simultaneous spectral display of multiple laser tones. However, it performs less favorably in terms of speed and resolution. Our objective is to build a system that combines the advantages of both: simultaneous monitoring of multiple lasers with high resolution and speed.

To accomplish this, we adopted a design developed previously in the Doyle group at Harvard. The key idea is to use a galvanometer-mounted mirror to route multiple laser beams into a single fiber input sequentially. When the switching rate is fast enough, the system effectively mimics real-time monitoring of multiple laser frequencies.

The galvanometer (Thorlabs) converts an externally applied analog voltage into a proportional rotation of the mirror mounted on it. In our implementation, we define eight discrete angular positions, each corresponding to a different laser beam path being coupled into a common fiber. By periodically varying the applied voltage, the mirror rotates through these positions in sequence, allowing the system to cycle through eight laser inputs.

To support broadband wavelength compatibility (from 400 nm to 1100 nm), we utilize a photonic crystal fiber from NKT Photonics, which efficiently couples all relevant laser wavelengths into the wavelength meter.

For the mirror control, we use a counter-to-DAC circuit controlled by an external clock signal. The clock is a TTL square wave that drives a 3-bit binary counter, cycling through values from '000' to '111' and back. These digital outputs are fed into a parallel DAC chip, converting the binary count into an analog voltage. This voltage drives the galvanometer to the corresponding angular position. Simultaneously, the clock signal is also sent to the wavelength meter to trigger its internal photodetector exposure, ensuring synchronization between mirror switching and wavelength measurements.

Chapter 3

Detection techniques

3.1 Overview of the detection techniques

Detecting different chemical species, particularly with quantum-state sensitivity, is a critical component of our experiment. A central objective for us is to accurately probe the quantum state distributions after chemical reactions or inelastic collisions. This capability enables a direct comparison between experimental observations and theoretical models, providing insight into the fundamental dynamics that govern these processes.

Our experimental apparatus essentially has two "senses": absorption imaging and ionization detection. Before delving into detailed descriptions of these detection techniques, we first outline the advantages and limitations of each method, highlighting the complementary roles they play in our studies.

Absorption imaging, a widely used technique in the AMO physics community [68], is employed to detect reactant atoms and molecules in the experiment. It offers two major advantages: inherent quantum-state selectivity and the ability to measure spatial distributions with high precision. On the other hand, absorption imaging has notable limitations: it is effective only for trapped atoms and molecules at very low temperatures, making it unsuitable for detecting most fast-moving reaction or collision products. Furthermore, it performs poorly when probing small ensembles consisting of only tens of atoms or molecules, as the weak absorption signal results in a low signal-to-noise ratio. Finally, absorption imaging requires the species to possess a cycling transition to scatter a sufficient number of photons, limiting its applicability to only a selected range of species.

Ionization detection, more prevalent in physical chemistry experiments [69, 70, 71], is employed in our work in the form of photo-ionization (both one-photon and two-photon) and field ionization. One-photon ionization typically uses a single UV photon capable of ionizing any species whose ionization threshold lies below the photon energy, but it lacks quantum-state selectivity. In contrast, resonant two-photon ionization (commonly referred to as REMPI, although "multi" in our case refers specifically to "two") offers high quantum-state sensitivity. In REMPI, the first photon resonantly excites the atom or molecule via a bound-to-bound transition, and a second photon ionizes it. While REMPI requires detailed spectroscopic knowledge of the intermediate states, which can be challenging when exploring new systems, it enables precise probing of quantum-state-specific outcomes of chemical

reactions and inelastic collisions. Finally, we can also detect Rydberg atoms through electric field ionization, a technique that will be discussed in more detail in Chapter 6 as part of our Rydberg studies.

3.2 Absorption imaging of atoms and molecules

In essence, absorption imaging utilizes a cycling transition to scatter photons, casting a shadow of the atoms onto a camera. The requirement of a cycling transition limits its applicability to specific quantum states of K and Rb atoms in our experiment. For Rb, we use the $|2,2\rangle \rightarrow |3,3\rangle$ transition for imaging. For K, we use either the $|9/2,9/2\rangle \rightarrow |11/2,11/2\rangle$ or the $|9/2,-9/2\rangle \rightarrow |11/2,-11/2\rangle$ transitions, depending on the initial quantum state of the K atoms. Additionally, we can image KRb molecules by coherently dissociating them into K and Rb atoms via a reversed STIRAP sequence followed by a Feshbach field ramp.

We have independent imaging systems for both the evaporation and science chambers. Each absorption imaging setup is a standard 4-f optical system [72], comprising a pair of lenses with equal focal lengths and a CCD camera (PCO Pixelfly) positioned at the image plane. A typical imaging sequence involves capturing three consecutive image frames: a shadow frame, a light frame, and a background frame. The shadow frame is captured with an imaging beam resonant to the atomic cycling transition, which passes through the atom cloud and casts a shadow on the camera. The light frame is taken with the imaging beam on but

without atoms present in the chamber, while the background frame is captured without any imaging beam.

From these images, we can extract detailed information about the density distribution, temperature, and total number of atoms using the following procedure. We first define the optical depth (OD) at each pixel:

$$\mathrm{OD}(x,y) = -\log\left(\frac{I_{\mathrm{shadow}}(x,y) - I_{\mathrm{background}}(x,y)}{I_{\mathrm{light}}(x,y) - I_{\mathrm{background}}(x,y)}\right), \tag{3.1}$$

where I_{shadow}, I_{light}, and $I_{\mathrm{background}}$ are the recorded intensities at pixel (x,y) for the respective frames.

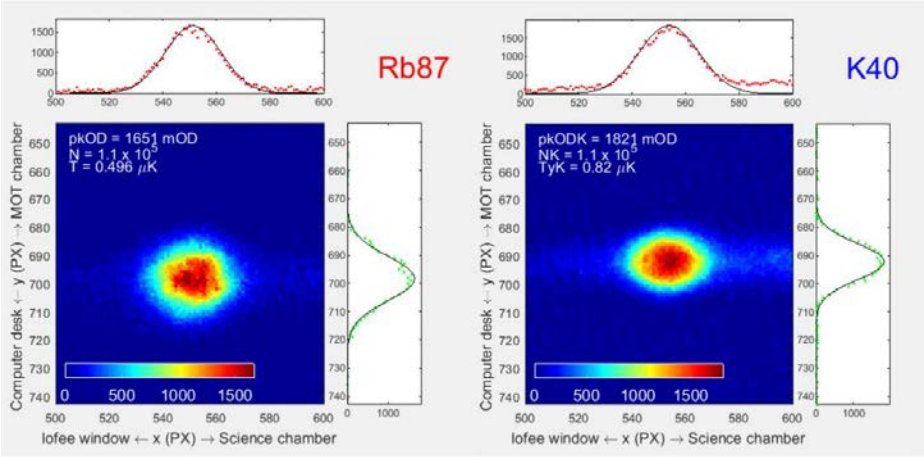

Figure 3.1: Absorption imaging results of Rb and K atoms after ODT evaporation. The atoms are released from the XODT and imaged after time-of-flight (TOF) of 5 ms (K) and 7 ms (Rb). The images are constructed from the three camera frames according to Eq. 3.1. For better visualization, we use milli-optical depth (mOD), where 1 mOD corresponds to 1/1000 of an OD of 1. The x and y axes are given in units of camera pixels (6.45 μm per pixel). We extract the peak optical depth (pkOD) and cloud widths σ_x and σ_y after TOF expansion and calculate the atom number N and temperature T for each species. A small fraction of atoms appear outside the central cloud region, spreading primarily along the horizontal direction. This effect is attributed to a slight mismatch between the HODT and VODT foci, resulting in some atoms being trapped only in the HODT without confinement from the VODT.

The OD value at each pixel represents the integrated atom number along the imaging axis at that location. A two-dimensional matrix of OD values is constructed to form an "OD image". We fit the OD image to a 2-dimensional

Gaussian distribution, from which we extract three parameters: the peak optical depth (peakOD), and the cloud sizes σ_x and σ_y for further processing.

For a thermal cloud of atoms at temperature T in a three-dimensional harmonic trap, the Gaussian width (standard deviation $\sigma_{x,y}$) of the cloud after a time-of-flight (TOF) expansion is given by [73]:

$$\sigma_{x,y}^2 = \frac{k_B T}{m} \frac{1 + \omega_{x,y}^2 \, \mathrm{TOF}^2}{\omega_{x,y}^2}, \tag{3.2}$$

where $\omega_{x,y}$ are the trapping frequencies along the x and y directions, m is the mass of the species, and k_B is the Boltzmann constant.

In typical experiments, the imaging beam is tuned on-resonance with the cycling transition to maximize the signal-to-noise ratio. Under this condition, the total atom number N can be extracted from the OD image using:

$$N = \frac{2\pi}{\sigma_0} \, \mathrm{peakOD} \, \sigma_x \sigma_y, \tag{3.3}$$

where σ_0 is the resonant scattering cross-section. The cross-section is related to the saturation intensity I_{sat} of the cycling transition by [74]:

$$\sigma_0 = \frac{\hbar \omega \Gamma}{2 I_{\mathrm{sat}}}, \tag{3.4}$$

with Γ being the natural linewidth of the transition and ω being the optical frequency.

From Eq. 3.2 and Eq. 3.3, one can see that the total atom number N is simply the product of the three extracted cloud parameters (peakOD, σ_x, and σ_y), whereas the temperature T has a nontrivial dependence on the trapping frequencies $\omega_{x,y}$ as well. While it is possible to calculate T using a single time-of-flight (TOF) measurement and the known trapping frequencies $\omega_{x,y}$ obtained through parametric heating experiments, this approach is only valid if the foci of the HODT and VODT are perfectly aligned.

An alternative approach, which we refer to as the TOF expansion method, determines the temperature by varying the TOF and extracting the slope of $\sigma_{x,y}^2$ versus TOF^2, which according to Eq. 3.2 should yield $\frac{k_B T}{m}$. This method depends solely on the atomic velocity distribution during free expansion and is independent of the initial cloud size and shape, making it inherently more accurate.

In practice, we often intentionally misalign the HODT and VODT slightly to improve ODT evaporation efficiency and achieve better molecule conditions. As a result, the TOF expansion method becomes the only valid and accurate technique for measuring the cloud temperature. Nevertheless, for quick daily diagnostics, we still use the single-shot method and use σ_y to obtain rough estimates of the cloud temperature, even though it tends to overestimate the true temperature, especially at short TOFs.

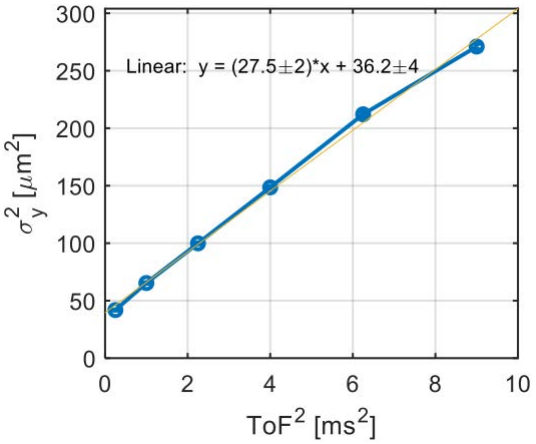

Figure 3.2: KRb temperature measurement by varying the time-of-flight (TOF). We measure the Rb atoms following molecular dissociation at TOF values between 0.26 ms and 9 ms, and extract the Gaussian widths along the more tightly confined y-direction. The cloud temperature and initial size at TOF = 0 ms are obtained from the slope and y-intercept of a linear fit to σ_y^2 versus TOF^2. From this measurement, we determine a KRb temperature of 290 ± 20 nK and an initial Gaussian width $\sigma_y = 6.0 \pm 0.3\ \mu$m. It is worth noting that we do not use the x-direction TOF expansion to extract the temperature, as σ_x at $t = 0$ is already large and the expansion during TOF is negligible, leading to large uncertainties in the temperature estimation along that axis.

3.3 Ionization detection

The capability to detect ions within an AMO experiment setting is one of the features that makes our apparatus unique. In our setup, neutral reaction products are first photoionized by a laser pulse, then accelerated by velocity map imaging (VMI) ion optics, and subsequently detected by a microchannel plate (MCP) detector after traveling through a one-meter-long time-of-flight (TOF) tube [60]. The MCP records both the TOF and the spatial hit locations of the ions, enabling the determination of both the species' mass and translational velocities.

In the following subsections, we discuss the different ionization techniques employed in our experiment in detail and explain how we extract useful information about chemical reactions and collision dynamics from the collected ion data.

3.3.1 Direct UV ionization with pulsed dye laser

Single-photon UV ionization is the most conceptually simple method used in our experiment. Considering the ionization thresholds of all relevant species (K, Rb, KRb, K_2, Rb_2, K_2Rb, KRb_2, and K_2Rb_2), the UV laser system must be able to operate at wavelengths below 300 nm. In addition, wavelength tunability of the laser is desired to efficiently ionize different product species (or selectively ionize certain species only).

Additionally, we must choose to use a pulsed laser rather than a continuous-wave

(CW) laser, as TOF spectrometry requires a well-defined time zero. This constraint leads to our use of a frequency-doubled pulsed dye laser. Our tunable dye laser (LIOP-TEC/LiopStar-HQ) is pumped by a pulsed, frequency-doubled $Nd:YVO_4$ laser (EdgeWave BX80) operating at 532 nm, as illustrated in Fig. 3.3.

The pump laser features an adjustable repetition rate of up to 10 kHz and a maximum pulse energy of 3 mJ, which remains relatively independent of the repetition rate. The 532 nm pump beam is delivered to the dye laser through free space and is split with a 30:70 power ratio between the two stages of the dye laser: the oscillator and the amplifier.

The oscillator stage functions in a way similar to a seed laser in fiber laser systems. Cylindrical lenses focus the pump beams into a thin line, creating a high-intensity region that turns the illuminated area of laser dye into a gain medium. The laser dye is circulated at a high flow rate (5–10 L/min) through a dye cell with a thin cross-section, allowing for a fast refresh rate of the laser dye to prevent excessive photo-bleaching. This design enables stable operation at high repetition rates of up to 10 kHz; however, in practice, the pulse energy decreases significantly for repetition rates above 5 kHz.

In the context of this thesis, we primarily used two types of laser dye, LDS 698 and LDS 798, to ionize the intermediate complexes KRb_2^* for Rb + KRb collisions. Between these, LDS 698 was used for most studies because it provides the highest pulse energy at the desired wavelength, while LDS 798 was used for more specific tasks, such as confirming the ionization threshold of KRb_2^* complexes. Typically,

with a 3 mJ pump pulse energy at 532 nm, we obtain 50–60 μJ of pulse energy from the oscillator at 709 nm (the optimal wavelength for ionization of KRb_2^* complexes) and 1.0–1.2 mJ of pulse energy from the amplifier. The efficiency of the frequency-doubling stage depends strongly on the beam size after amplification, due to the quadratic dependence of second-harmonic generation (SHG) efficiency on the beam intensity. After frequency doubling, we typically obtain 30–50 μJ of UV pulse energy at 354 nm.

Apart from our choices of laser dyes, a wide variety of laser dyes can be used to generate different UV wavelengths for ionizing different reaction products, following the laser dye recipes shown in Tab. 3.1. In general, Rhodamine dyes are preferred for generating shorter UV wavelengths (280–310 nm) due to their higher conversion efficiencies.

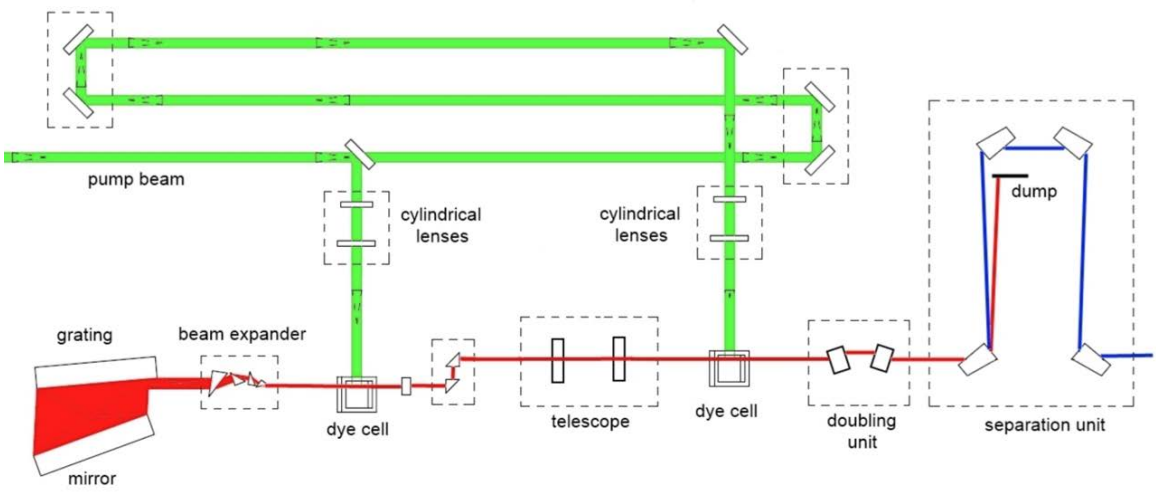

Figure 3.3: Schematics of the dye laser (Picture from LIOP-TEC/LiopStar manual [75]). The dye laser consists of an oscillator, an amplifier, and a frequency-doubling stage. The grating at one end of the oscillator stage acts as a frequency-selection unit, similar to its usage in an ECDL. By adjusting the grating angle, the feedback spans a wide range of wavelengths from 532 nm up to 810 nm (tested experimentally), although the user manual specifies operation only up to 750 nm. The output from the oscillator is slightly magnified and collimated using a telescope consisting of two lenses and subsequently sent to the amplifier cell. The amplified light is frequency-doubled via SHG using a BBO (beta barium borate) crystal. To separate the frequency-doubled UV light from the residual fundamental light, a separation unit consisting of four dispersive prisms is placed after the SHG setup. The resulting UV beam (usually elliptical with one axis diverging) is then shaped and collimated with external lenses and delivered to the experiment through free space.

While changing the laser dye enables coarse tuning of the laser wavelength by tens of nanometers, fine adjustments on the order of a few nanometers can be achieved by varying the dye concentration and selecting a different solvent. Historically, we have also used DMSO (dimethyl sulfoxide) as a solvent to push the emission toward longer wavelengths. However, extra caution must be taken when handling DMSO due to its associated difficulties and potential hazards, a reason why we stopped using it in recent years.

Typically, we prepare the laser dye solution by dissolving a measured amount (approximately 1 gram) of laser dye, weighed using an analytical balance, into 1 gallon of 200-proof ethanol. The mixture is then stirred overnight using a magnetic stir bar to ensure complete dissolution. Before introducing fresh dye solution into the dye pumps, the old laser dye solution is first drained from the system through a valve. Because this draining process leaves behind residual dye, a cleaning procedure is performed by adding one gallon (any amount above half a gallon) of 190-proof methanol (which is significantly cheaper than ethanol) and circulating it through the pump to dilute any remaining dye, after which we drain the waste solution through the valve. This rinse-dilute-drain cycle is typically repeated three to six times, depending on the amount of methanol used in each step. After this procedure, the final solution becomes visibly transparent, indicating effective removal of residual dye from the system.

Table 3.1: Laser-dye recipes for 532 nm pumping (from Sirah [76])

Name	**Peak** (nm)	**Range** (nm)	**Eff.** (%)	**Solvent**	**Conc.** ($g\,L^{-1}$)
Fluorescein 548	550	541–571	27	Ethanol + H_2O	0.40
Pyromethene 580	557	547–581	28	Ethanol	0.20
Rhodamine 590	566	559–576	28	Ethanol	0.09
Pyromethene 597	582	566–611	28	Ethanol	0.16
Kiton Red 620	591	585–600	26	Ethanol	0.20
Rhodamine 610	596	588–614	26	Ethanol	0.20
Mix. Rh 610/Rh 640	615	598–636	26	Ethanol	0.17 / 0.04
Rhodamine 640	624	614–662	25	Ethanol	0.25
DCM	627	602–660	27	Ethanol	0.30
DCM	651	626–685	27	DMSO	0.30
LDS 698	692	667–720	20	Ethanol	0.25
LDS 722	718	691–751	19	Ethanol	0.25
LDS 751	744	712–782	15	Ethanol	0.15
LDS 751	764	733–802	15	DMSO	0.15
LDS 798	785	758–826	12	Ethanol	0.14
LDS 821	815	791–839	10	Ethanol	0.13
LDS 821	839	814–862	10	DMSO	0.13
LDS 867	863	832–900	10	Ethanol	0.15

3.3.2 REMPI for product quantum state detection

Since single-photon UV ionization lacks intrinsic quantum state selectivity, we use REMPI to extract product state distributions. The REMPI process typically involves two laser pulses: a resonant excitation pulse that transfers ground-state population to an electronically excited state, followed by a strong 532 nm pulse that ionizes the particle. Because the first step requires the resonance condition to be met, only products in a specific initial quantum state can be excited and subsequently ionized, enabling state-selective detection.

Most electronic transitions of the involved species in our experiment are approximately 10 MHz in width, limited by spontaneous decay, necessitating the use of narrow-linewidth lasers. Furthermore, wide frequency tunability is required to address different initial quantum states. All these requirements make external cavity diode lasers (ECDLs) an efficient and cost-effective choice. In our experiment, we utilize three ECDLs for REMPI of Rb (420 nm), K_2 (648 nm), Rb_2 (674 nm), and KRb (667 nm), with the 670 nm ECDL covering both Rb_2 and KRb within its tunable range.

The physical setup of the 670 nm laser is shown in Fig. 3.4. We use an AR-coated laser diode (EYP-RWE-0670-00703-1000-SOT02-0000) in an ECDL configuration to seed a tapered amplifier (EYP-TPA-0670-00500-2004-CMT02-0000). At a drive current of 130 mA, the seed laser produces approximately 24 mW of output power, which is sufficient for amplification. The amplified light is collimated

in one direction using an aspheric lens immediately after the TA chip. In the orthogonal direction, we use an external cylindrical lens for collimation. After collimation, the beam is focused into an AOM in the horizontal direction using a second cylindrical lens, enabling fast optical switching (∼50 ns) with external modulation signals. The first-order diffraction of the AOM is then fiber-coupled and combined with the 532 nm pulsed laser using a dichroic mirror before being finally delivered to the experiment.

Frequency tuning of the 670 nm laser can be achieved at multiple levels. Coarse tuning by several nanometers (corresponding to a few terahertz in frequency) can be achieved by carefully adjusting the horizontal knob of the grating to change its angle. Temperature control of the diode mount and the entire laser housing within a few degrees Celsius of the room temperature enables frequency tunability on the order of tens of gigahertz. Finally, fine-tuning of the laser frequency by a few gigahertz can be achieved by adjusting the voltage applied to the piezo actuator attached to the horizontal tuning knob of the grating. We note that our use of an AR-coated diode significantly improves laser mode stability, as it reduces the likelihood of mode hops and enables more continuous and stable operation.

REMPI detection of Rb atoms is performed with a two-photon ionization scheme, where the atoms are first excited from the $5S_{1/2}$ state to the $6P_{3/2}$ state, and subsequently ionized with a 532 nm pulsed laser. We use a 420 nm ECDL laser (Toptica DL pro) with a maximum output power near 50 mW (at 80-90 mA of operating current). Because the transition dipole moment connecting $5S_{1/2}$ and

$6P_{3/2}$ is large, we use about 2 mW of 420 nm laser power for the first leg of Rb REMPI. We note that this laser is also used for Rb Rydberg excitation (see Chapter 6).

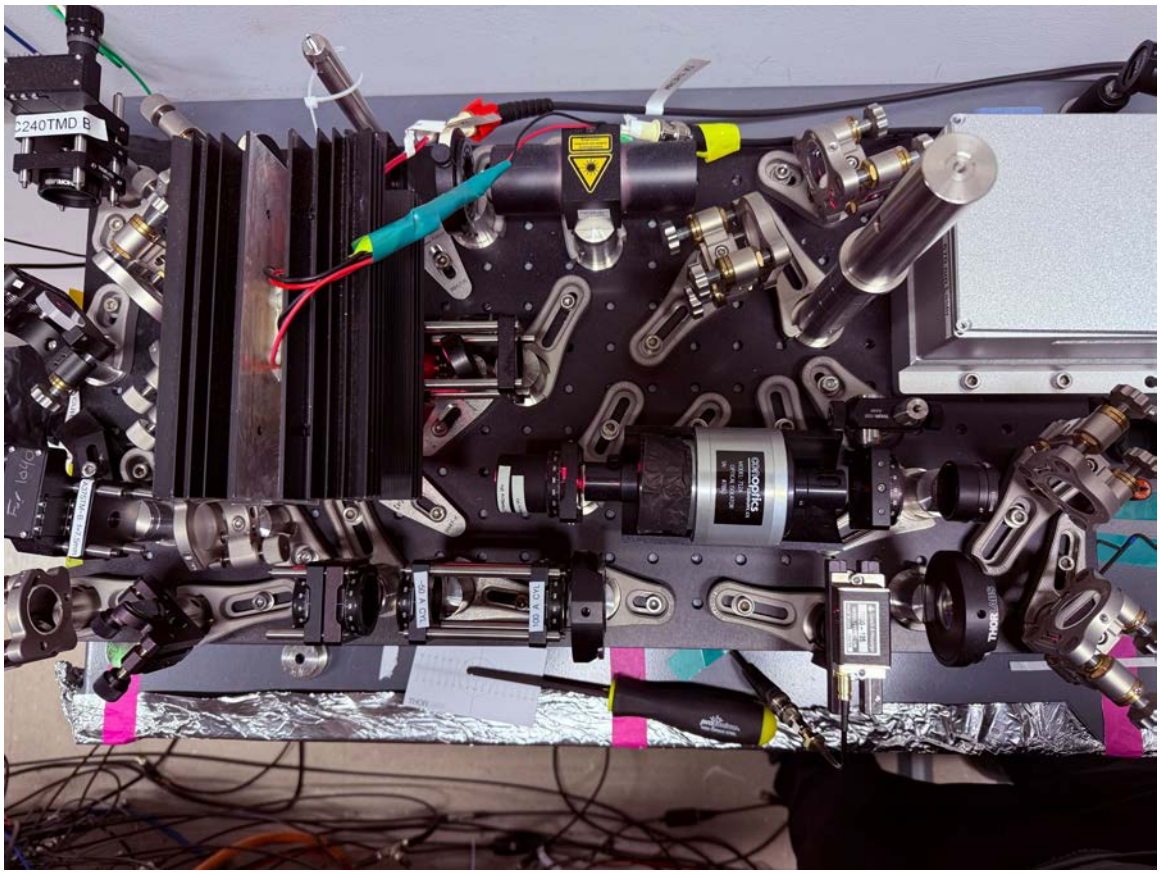

Figure 3.4: Physical setup for the 670 nm laser used for Rb_2 and KRb REMPI detection, mounted on a separate breadboard that is not attached to the machine table.

For K_2, we use a 648 nm laser to resonantly excite product molecules to an electronically excited state, similar to the REMPI setup used for Rb_2 and KRb.

Instead of using an AR-coated diode in an ECDL configuration, this laser was built using a non-AR-coated diode (Ushio HL65014DG), as high-power AR-coated diodes at this wavelength are difficult to find.

Non-AR-coated diodes are notoriously known for their multimode behavior and frequent mode hops, and our 648 nm laser is no exception. To maintain stable single-mode operation, we limit the diode current to below 230 mA and the output power to 50 mW, which is significantly lower than its maximum rating of 150 mW. Even under these constraints, it remains highly challenging to achieve continuous frequency tuning and single-mode operation, as the mode-hop-free tuning range is below 1 GHz. Recently, this laser diode was discontinued, prompting us to explore an alternative setup for K_2 REMPI. This involves two plans: an injection-lock setup using a more stable AR-coated diode as the seed laser for a high-power non-AR-coated diode, and a TA-based amplification setup.

Regardless of the species involved, it is essential to emphasize that REMPI is inherently a sequential excitation process: the atom or molecule is first excited to an intermediate (electronically excited) state, and then ionized by a high-intensity laser pulse (532 nm in our case). A REMPI process can be effectively modeled using the framework we described in [77], which is essentially a two-level system with loss in the excited state:

$$\frac{d}{dt}\rho_{gg} = -\frac{i}{2}(\Omega_{ge}\rho_{eg} - c.c.), \tag{3.5}$$

$$\frac{d}{dt}\rho_{ee} = -(\Gamma + \Gamma_{\text{ion}})\rho_{ee} + \frac{i}{2}(\Omega_{ge}\rho_{eg} - c.c.), \tag{3.6}$$

$$\frac{d}{dt}\rho_{eg} = -\frac{1}{2}(\Gamma + \Gamma_{\text{ion}})\rho_{eg} + i\Delta\rho_{eg} + \frac{i}{2}\Omega_{eg}(\rho_{ee} - \rho_{gg}), \tag{3.7}$$

where *c.c.* stands for complex conjugate, Ω_{ge} is the Rabi rate of the bound-to-bound transition, Δ is the laser detuning (ideally zero), Γ is the spontaneous decay rate of the excited state $|e\rangle$, and Γ_{ion} is the ionization rate of the 532 nm bound-to-continuum transition.

A typical REMPI pulse sequence used in our experiment is shown in Fig. 3.5. The relative timing between the two pulses is critical and is typically scanned in 10 ns steps using a digital delay generator. The optimal timing of the 532 nm pulse is tens of nanoseconds after the bound-to-bound transition pulse, depending on the Rabi rate. This is because of the finite time required to transfer the population from the ground state to the excited state.

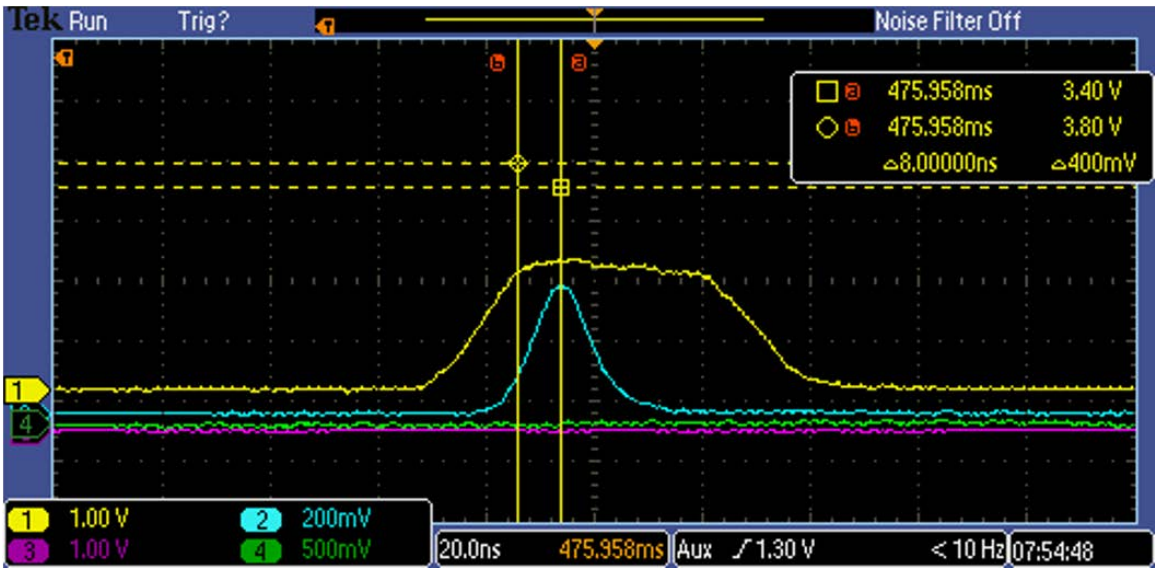

Figure 3.5: Scope traces for the Rb_2 REMPI using a 674 nm CW laser and a 532 nm pulsed laser. The yellow and blue traces correspond to the intensities of the 674 nm and 532 nm laser beams. The traces were recorded using a high-bandwidth photodetector (Thorlabs PDA8A2, with a rise time of 7 ns), which captured the relative intensity evolution of each beam over time.

As described by Eq. 3.7, the excited state population reaches its first maximum shortly after excitation begins, which sets the optimal timing for the bound-to-continuum (532 nm) pulse for efficient ionization. The CW laser light is no longer needed after the 532 nm pulse has been generated. Keeping it on for longer durations can lead to off-resonant excitation and scattering of both reactants and products. To prevent this, we typically switch off the CW beam within tens of nanoseconds after the 532 nm pulse.

For Rb atoms, the excited state ($6P_{3/2}$) decay rate Γ is $2\pi \times 1.1$ MHz [78], and a typical Rabi rate is also $2\pi \times 1.1$ MHz with 2 mW of 420 nm laser power and a $1/e^2$ beam radius of 1 mm. For KRb, Rb_2 and K_2, the excited state decay rates are about $2\pi \times 15$ MHz. Using 10 mW of laser power for the bound-to-bound transition, we can achieve typical Rabi rates of $2\pi \times 11$ MHz.

Finally, frequency stabilization of the REMPI lasers is achieved via wavemeter-based locking. Each laser's frequency is continuously monitored using a wavelength meter, and deviations from the target setpoint are calculated in real-time. A software-based PID servo then generates a corresponding feedback voltage, which is applied to the laser's piezo actuator to close the feedback loop and maintain frequency stability within ± 5 MHz from the setpoint.

3.4 Coincidence detection: Pairing up the products

We now have the tools to probe the quantum states of reaction products through REMPI. However, in many cases, multiple product molecules or atoms are generated in a single reaction event. Detecting all products originating from the same event can reveal correlations, providing deeper insight into the underlying reaction dynamics. To achieve this, it is necessary to correlate ion signals from different product species and identify those originating from the same reaction event. This correlation is

enabled in our experiment using a post-selection technique, known as coincidence detection.

Coincidence detection is solely used for the KRb + KRb $\rightarrow$ K_2 + Rb_2 reaction, where the moderate energy release ($\sim$300 GHz) produces product transverse momenta that are large enough to be resolved by velocity map imaging (VMI) [71], yet small enough to remain within the detectable range.

The procedure for coincidence detection can be described as follows: For each REMPI pulse, we identify the corresponding K_2 and Rb_2 ion signals, as shown in Fig. 3.6. We then iterate through each K_2–Rb_2 pair and select only those that satisfy momentum conservation criteria in all three spatial directions, as described in [79]. Quantitatively, the momentum conservation criteria can be expressed as three inequalities corresponding to the transverse (X, Y) and time-of-flight (Z) directions:

$$|(X_{\mathrm{K_2}} - X_{0,\mathrm{K_2}}) + \sqrt{M_{\mathrm{Rb_2}}/M_{\mathrm{K_2}}}(X_{\mathrm{Rb_2}} - X_{0,\mathrm{Rb_2}})| \leq n\sigma_X\sqrt{1 + M_{\mathrm{Rb_2}}/M_{\mathrm{K_2}}}, \tag{3.8}$$

$$|(Y_{\mathrm{K_2}} - Y_{0,\mathrm{K_2}}) + \sqrt{M_{\mathrm{Rb_2}}/M_{\mathrm{K_2}}}(Y_{\mathrm{Rb_2}} - Y_{0,\mathrm{Rb_2}})| \leq n\sigma_Y\sqrt{1 + M_{\mathrm{Rb_2}}/M_{\mathrm{K_2}}}, \tag{3.9}$$

$$\begin{aligned}|(TOF_{\mathrm{K_2}} - TOF_{0,\mathrm{K_2}}) + (TOF_{\mathrm{Rb_2}} - TOF_{0,\mathrm{Rb_2}})\frac{(\eta\delta t/TOF_{0,\mathrm{K_2}} - 1)}{(\eta\delta t/TOF_{0,\mathrm{Rb_2}} - 1)}| \\ \leq n_T\sigma_T\sqrt{1 + (\frac{(\eta\delta t/TOF_{0,\mathrm{K_2}} - 1)}{(\eta\delta t/TOF_{0,\mathrm{Rb_2}} - 1)})^2}.\end{aligned} \tag{3.10}$$

Here, σ_X, σ_Y, and σ_T represent the 1σ spatial and temporal resolutions of the detection system, which depend on the applied acceleration voltage. The quantities X_{K_2}, X_{Rb_2}, Y_{K_2}, and Y_{Rb_2} are the ion hit positions determined by the transverse

velocities, magnetic field, and acceleration voltage. X_{0,K_2}, X_{0,Rb_2}, Y_{0,K_2}, and Y_{0,Rb_2} are the averaged hit positions for each species along the X and Y directions. Similarly, TOF_{K_2} and TOF_{Rb_2} are the measured time-of-flights, while TOF_{0,K_2} and TOF_{0,Rb_2} represent the average TOFs for each species.

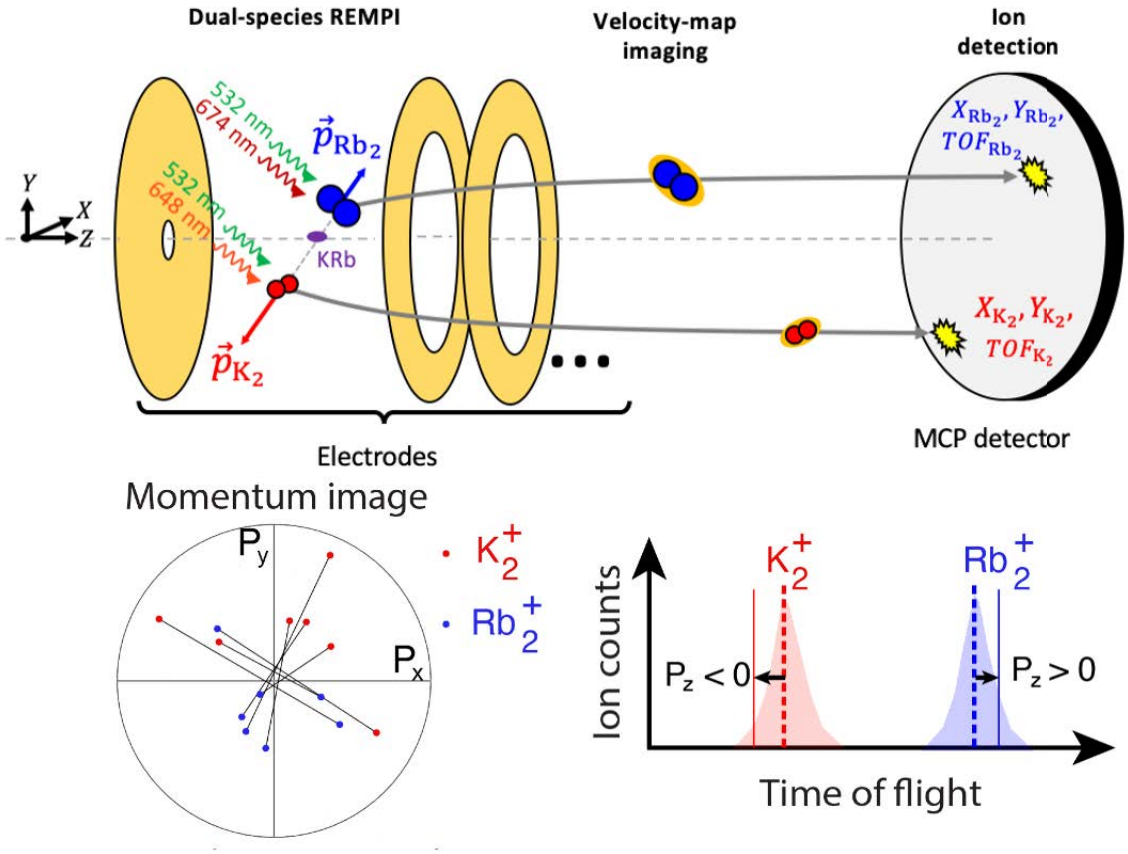

Figure 3.6: Coincidence detection setup [43]. Upper panel: REMPI of K_2 and Rb_2. The electric field generated by the plate electrodes accelerates ions to the MCP detector. When the velocity map imaging (VMI) condition is satisfied [71], the ion hit positions depend linearly on their transverse momenta. Bottom left panel: Momentum correlation of K_2 and Rb_2 products. K_2 and Rb_2 created from the same reaction event must have equal and opposite transverse momenta. Bottom right panel: Time-of-flight correlation of K_2 and Rb_2 products. K_2 and Rb_2 from the same reaction must also have equal and opposite momenta along the time-of-flight axis. After a short free-flight period in the absence of an electric field, the two ions experience different acceleration voltages, leading to anti-correlated TOFs at the detector.

The parameter δt represents the free-flight time of neutral reaction products after the chemical reaction before ionization. Given the 10 kHz repetition rate of the ionization pulses, δt follows a uniform distribution between 0 and 45 μs. The parameter η is a geometrical factor determined by the electrode configuration, which is 136 in our system [60].

We can vary the acceleration voltage (repeller voltage) to tune the sensitivity and detection range of our VMI system. Typically, we choose a repeller voltage V_{rep} (that sets the acceleration voltage) between 100 V and 2 kV. When $V_{\text{rep}} = 100$ V, we found $\sigma_X = 0.23$ mm, $\sigma_Y = 0.23$ mm, and $\sigma_T = 11$ ns. At $V_{\text{rep}} = 2000$ V, $\sigma_X = 0.08$ mm, $\sigma_Y = 0.08$ mm, and $\sigma_T = 4$ ns. The parameters n and n_T set the strictness of the filter conditions and are determined empirically to balance loss of signal and background suppression. In practice, we typically choose $n = 3$ and $n_T = 3$ to effectively suppress uncorrelated ion counts while maintaining a high coincidence signal.

In addition to the momentum filters, we also implemented a scheme to cancel the effect of accidental coincidence events [43, 79]. These events occur when K_2 and Rb_2 ion signals originate from different reaction events but pass all momentum filters completely by chance.

In this scheme, we vary the ionization pulse number difference between -50 and $+50$, and pair K_2 and Rb_2 ions from different ionization pulses using the momentum filtering criteria. Ideally, K_2 and Rb_2 ions from different ionization pulses should never satisfy the coincidence conditions, resulting in zero coincident product pairs.

However, this is not the case in actual experiments. In reality, we plot the number of filtered K_2–Rb_2 pairs as a function of pulse number difference, as shown in Fig. 3.7. The average ion count at nonzero pulse number differences yields N_{res}, indicated by the red dashed line in Fig. 3.7, representing the number of accidental coincidences. The true signal, N_0, is defined as the number of K_2–Rb_2 pairs from the same ionization pulse satisfying the momentum filters. Therefore, the background-free coincidence signal is then calculated as $N_{sig} = N_0 - N_{res}$.

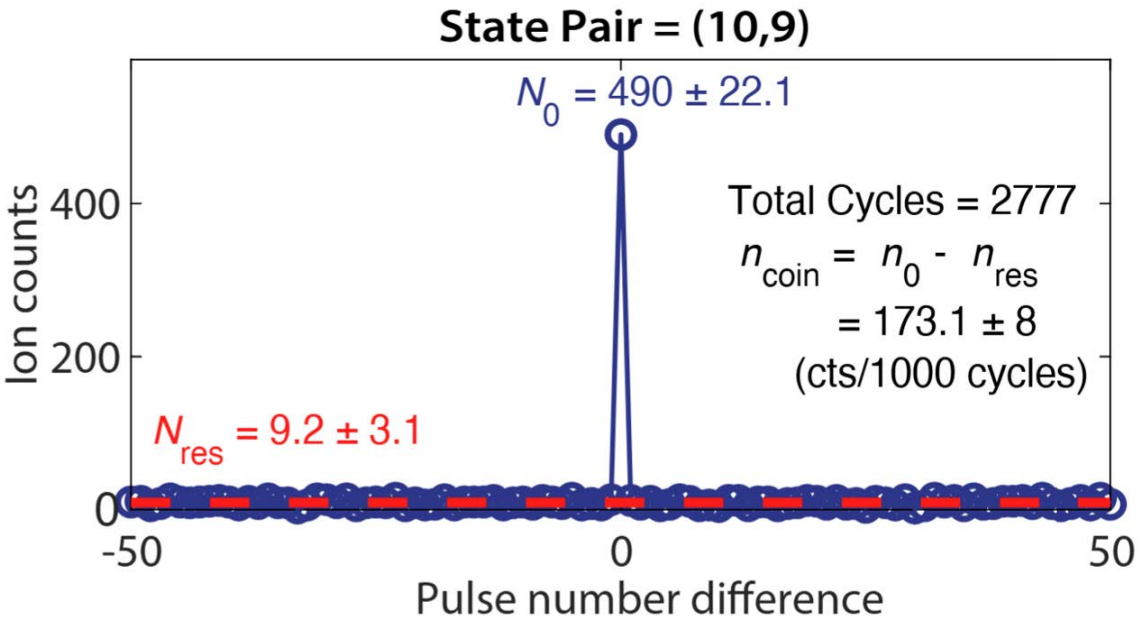

Figure 3.7: An example of the pulse number shift scheme used to cancel accidental coincidence background [79]. Here, we probe the rotational state pair ($N_{K_2} = 10$, $N_{Rb_2} = 9$) at a magnetic field of $B = 5$ G, where the initial KRb quantum state is $|\psi_f\rangle = 0.595|-4, 1/2\rangle + 0.719|-3, -1/2\rangle + 0.359|-2, -3/2\rangle$ as characterized in [36]. The data shown were collected over a total of 2777 experimental cycles.

Chapter 4

Probing the long-lived intermediate complex: observations and implications

4.1 Introduction

Collisional complexes, formed as transient intermediates during molecular collisions, are typically short-lived and decay within picoseconds under typical thermal conditions. However, in the ultracold regime, particularly for bialkali molecules, these complexes can persist for up to milliseconds, many orders of magnitude longer than expected. Such long-lived complexes, arising from so-called sticky collisions, have become a significant obstacle in the pursuit of dense, stable,

and quantum degenerate molecular gases. Even in bialkali systems that are chemically nonreactive, these complexes can lead to two-body losses in the molecular sample [80, 81, 55, 82]. Despite extensive theoretical and experimental efforts over the past decade, the behavior of these complexes remains only partially understood. In some systems, measured lifetimes far exceed the predictions of statistical models such as Rice–Ramsperger–Kassel–Marcus (RRKM) theory [83], while in others, the predictions and measurements appear to be in reasonable agreement. A unified understanding of complex lifetimes remains lacking, and such an understanding is crucial for uncovering the short-range quantum dynamics that govern these processes. These short-range dynamics are likely to contain rich and hidden structure. Beyond their fundamental significance, a deep understanding of the formation and decay of ultracold complexes is essential for controlling collisional loss in molecular experiments. In this chapter, we provide an overview of recent progress in the field, aimed at addressing these questions, including new insights from our studies using the ultracold KRb system.

4.2 Intermediate complex and RRKM theory

The sticky collision mystery first emerged when multiple experiments unexpectedly observed two-body loss in ultracold samples of chemically nonreactive bialkali molecules, even when both molecules were prepared in their absolute internal ground states. In most cases, these losses appeared to be nearly universal, meaning

that almost every collision resulted in the loss of both colliding particles. This observation seemed contradictory to the expectation that, at ultracold temperatures, conservation of energy and momentum should forbid any chemical reaction or internal excitation that would lead to inelastic loss. A leading hypothesis was that the molecules form long-lived intermediate complexes upon collision, which remain near each other for durations orders of magnitude longer than typical molecular vibrational timescales ($\sim$ps). This idea was directly verified in our experiment through the detection of such complexes [84], and through variable photoexcitation-induced loss in the RbCs experiment [85]. Notably, in our study, we found that photo-excitation from the optical trapping light was responsible for the complex loss. However, other experiments subsequently reported substantial loss in the absence of any trapping light [86, 87], suggesting either the complex lifetimes were much longer than expected, or there exist other loss mechanisms.

Meanwhile, understanding the sticking time, or complex lifetime, poses a major theoretical challenge. Despite involving only four atoms, a full quantum scattering calculation for such systems remains out of reach due to their computational complexity [88, 89]. As a result, simpler statistical models such as RRKM theory have been employed. While RRKM has shown reasonable agreement with experimental results in some systems [85, 84], it fails to capture the observed behavior in others [86, 87], often underestimating the complex lifetime by several orders of magnitude.

The RRKM theory was originally developed to describe unimolecular reaction

rates in thermal chemistry [83]. The theory models the complex as a statistical ensemble that fully redistributes its internal energy among all available degrees of freedom. The lifetime is then estimated as the inverse of the rate at which the complex exits through any energetically allowed decay channel. In the context of ultracold sticky collisions, this rate depends on the density of available quantum states within the complex (density of states, DoS) and the number of open exit channels:

$$\tau = \frac{2\pi\hbar\rho_{\mathrm{DoS}}}{N_{\mathrm{exit}}} \tag{4.1}$$

4.3 Intermediate complex in ultracold bialkali collisions

Molecule	**Statistics**	**Nuclear spin**	τ_{exp}	τ_{RRKM}
^{23}Na^{39}K	boson	$\lvert -3/2, -1/2\rangle$	> 0.35 ms	6 μs
^{23}Na^{40}K	fermion	$\lvert 3/2, -4\rangle$	> 2.6 ms	18 μs (4.9 ms)
		$\lvert 3/2, -4\rangle$	> 1.4 ms	18 μs (4.9 ms)
		mixed	> 2.3 ms	18 μs (54 μs)
		mixed	> 133 μs	18 μs (54 μs)
^{23}Na^{87}Rb	boson	$\lvert 3/2, 3/2\rangle$	> 1.2 ms	19 μs
^{40}K^{87}Rb	fermion	$\lvert -4, 1/2\rangle$	360(30) ns	170(60) ns
^{87}Rb^{133}Cs	boson	$\lvert 3/2, 7/2\rangle$	0.53(6) ms	0.253 ms
	boson	$\lvert 3/2, 7/2\rangle$	0.8(3) ms	0.253 ms
	boson	$\lvert 3/2, 5/2\rangle$	2.1(1.3) ms	0.253 ms
	boson	$\lvert 1/2, 7/2\rangle$	> 3.3 ms	0.253 ms

Table 4.1: An overview of intermediate complex lifetimes for bialkali sticky collisions, adapted from the 2023 review paper [90]. The RRKM lifetimes in parentheses take into account reflections from the long-range potential, which will be discussed in more detail in later sections.

Since bialkali complexes typically have many internal rovibronic states but very few energetically allowed dissociation pathways at ultracold temperatures, the theory predicts relatively long lifetimes, as compared to the molecular vibration cycles.

Because of the importance of understanding intermediate complexes, which appear to exist across nearly all ultracold bialkali molecular platforms, numerous experimental investigations have been conducted. These experiments primarily focus on two key aspects of bialkali molecular collisions: the two-body loss rate and the lifetime (and loss mechanism) of the intermediate complex, both of which are critical in determining the overall stability and loss rate of the molecular gas. Here, we focus on the measurement of intermediate complex lifetimes, as summarized in Tab. 4.1 by a review paper in 2023 [90]. These measurements fall into two broad categories: direct detection via ionization of the complexes, as demonstrated in the KRb system, and indirect detection through trap modulation, where the overall loss rate is measured as a function of the modulation frequency. Direct measurements, currently only available in our experiment, offer higher accuracy due to their lower intrinsic background noise and rely on fewer assumptions of the photoexcitation model, but require a more complex ionization and detection apparatus—one that must typically be integrated into the experimental design from the outset. For other molecular species, the indirect method (also known as the chopping technique) has been the dominant approach for probing complex lifetimes, due to the lack of an ion detection setup.

In 2019, the former KRb team performed a direct measurement of the

intermediate K_2Rb_2 complex lifetime [84]. It was found that these complexes could be photo-excited and subsequently lost from the system upon exposure to 1064 nm ODT light. This observation inspired a method to measure the complex lifetime: by turning off the ODT light, one allows the complexes to accumulate in the absence of photo-excitation, during which they evolve solely under their intrinsic formation and dissociation dynamics. The time evolution of the complex population in the dark is governed by an exponential decay model, described by Eq. 4.2.

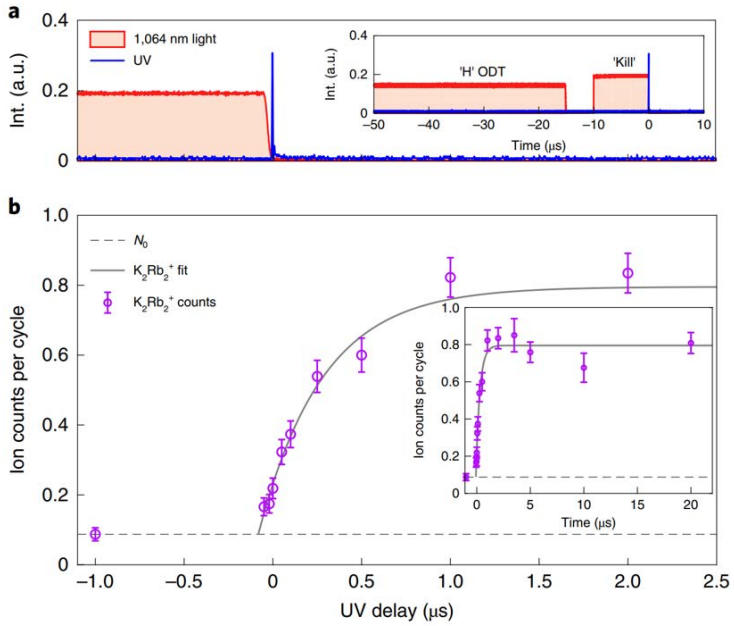

Figure 4.1: Direct measurement of the K_2Rb_2 complex lifetime [84]. (a) Experimental timing sequence. The optical dipole trap (ODT) light is switched off to allow the accumulation of complexes in the dark. A fast-switching "kill" ODT defines a precise $t = 0$ for starting the accumulation window. (b) Growth of the K_2Rb_2 complex population as a function of ODT dark time. The complex lifetime is extracted by fitting the data (purple circles) to an exponential growth model (black curve), with the time constant corresponding to the lifetime.

$$\frac{dn_c(t)}{dt} = \gamma - \frac{n_c(t)}{\tau} - \Gamma(I_{ODT})n_c(t) \tag{4.2}$$

Here, $n_c(t)$ denotes the complex density, γ is the complex formation rate

(assumed to be constant during the probing window), and τ is the complex lifetime. $\Gamma(I)$ represents the photoexcitation rate, which is set to zero in the absence of ODT light. The solution to Eq. 4.2 yields a simple exponential form, which agrees well with the experimental data shown in Fig. 4.1. From this fit, the complex lifetime is extracted to be 360(30) ns.

On the other hand, several other experiments involving NaK, NaRb, and RbCs have employed the indirect method to measure complex lifetimes [86, 87, 85]. Here, we highlight the RbCs experiment at Durham as a representative example. In their scheme, molecules are held in a 1064 nm optical trap modulated at various frequencies, both with and without the presence of a weak 1550 nm kill light. This kill light is sufficiently strong to deplete complexes, yet weak enough to avoid significantly altering the overall trapping frequencies. After a fixed modulation period (200 ms in this case), the remaining molecule numbers in both cases are compared. The difference between them arises from the so-called loss reduction effect. Specifically, the suppression of loss is determined by the ratio between the complex lifetime and the dark time of the trap modulation: the dark time must be long enough to allow a substantial fraction of the complexes to dissociate back into RbCs molecules before being lost by photoexcitation. One can extract the complex lifetime by fitting the observed modulation frequency-dependent loss suppression.

However, this method becomes ineffective when the complex lifetime significantly exceeds the trap dark time, which cannot be extended arbitrarily due to the onset of parametric heating in the molecular gas. In those cases (such as NaK and NaRb),

little to no reduction in the loss rate was observed with trap modulation. As a result, the method cannot provide a reliable measurement of the complex lifetime. Nevertheless, the absence of observable loss reduction still allows one to place a combined lower bound on the complex lifetime and the photo-excitation rate. Assuming the theoretically calculated photo-excitation rate is accurate, one can derive a lower bound for the complex lifetime in these cases.

4.4 Possible explanations

As shown in Tab. 4.1, the RRKM prediction for complex lifetimes shows qualitative agreement with experimental data in the cases of KRb and RbCs. However, in other systems such as NaK and NaRb, the RRKM-predicted lifetimes are orders of magnitude shorter than experimental observations. The reason for this discrepancy is unclear, but several possible explanations have been proposed that may shed light on this mystery.

First, the applicability of statistical models, such as RRKM, at ultracold temperatures is fundamentally uncertain. The density of states of the tetra-atomic complex typically ranges from 0.005 to 5 μK^{-1} for most bialkali species [90]. At ultracold temperatures ($T \sim \mu\text{K}$), the thermal collision energy spans only a narrow range, covering just a few resonances or, in some cases, missing them entirely. This seriously undermines the original assumption stated in the 2013 paper [91] that many narrow and isolated resonances would contribute to the dynamics within the

accessible collision energy window. Moreover, the presence of strong resonances in certain bialkali systems, especially for lighter species, would further violate the chaotic dynamics assumption, leading to significant deviations from its predictions.

Within the RRKM framework, there are two key parameters: the density of states of the intermediate complex, ρ_{DoS}, and the number of energetically allowed exit channels, N_{exit}. Current theoretical estimates of ρ_{DoS} typically account for the rotational and vibrational degrees of freedom of the tetra-atomic complex, under the constraint of motional angular momentum conservation: fixed J and its projection m_J. Therefore, when the angular momentum conservation is broken, one expects a significant increase in the effective density of states [92].

It has been predicted that three effects may significantly enhance the density of states in the presence of external electric fields. First, mixing of rotational states in the incoming channels due to long-range dipolar interactions can increase the density of states [93]. Second, non-conservation of J and m_J within the complex arising from anisotropic interactions can lift angular momentum constraints and further increase ρ_{DoS} [92, 94]. Third, if the nuclear spin degrees of freedom become activated, they introduce an additional phase space, potentially enlarging the density of states available to the reaction.

Among the three effects discussed, both long-range state mixing and angular momentum non-conservation in the short range [93] predict an increase in the complex lifetime at sufficiently high electric fields. The long-range effect occurs when the reactants effectively couple to multiple angular momentum states, typically

when the dipole–dipole interaction becomes comparable to the centrifugal barrier at a characteristic radius of the complex. This defines a critical electric field, estimated to be in the range of 10^2–10^3 V/cm for most bialkali species. Above this threshold, the density of states is expected to increase by roughly one order of magnitude (depending on the particular species) and then saturate at higher fields.

In contrast, the field-induced non-conservation of angular momentum, as predicted in [92, 94], exhibits a similar trend in the density of states versus electric field but with a lower critical threshold. In this case, the critical field is determined by comparing the Stark shift to the level spacing of the complex, leading to a typical value in the range of 10–10^2 V/cm. As a consequence, if m_J is no longer conserved, the density of states may increase by two to three orders of magnitude. If J and m_J conservation are broken, the enhancement can reach four to five orders of magnitude.

Although nuclear spin conservation has been demonstrated in the KRb + KRb reaction [36], its general applicability to other bialkali collisions is not guaranteed, particularly in systems where the complex lifetimes are significantly longer than that of the K_2Rb_2 complex. In such cases, the nuclear spin degree of freedom may become activated, allowing the projections of the individual nuclear spins to exchange freely within the complex. This can increase the density of states by one to two orders of magnitude. However, it also opens up a larger set of exit channels, since distinct nuclear spin states must be considered as separate final states. As a result, one would expect different complex lifetimes depending on the specific hyperfine state of the reacting molecules.

In addition, recent theoretical work [95] has proposed an alternative mechanism that may account for the unexpectedly long complex lifetimes observed in experiments. Specifically, when the number of available dissociation channels is close to one, the decay dynamics of the complexes can deviate significantly from those expected in systems with many channels. This leads to a non-exponential buildup of the ion signal over time. Fundamentally, this effect arises from the presence of multiple intermediate complex states, each of which has its distinct dissociation pathways to the asymptotic product channels with different strengths. As a result, different complex states have different lifetimes.

The coupling strengths between complex states and asymptotic channels follow a random distribution (assumed to be a normal distribution in their work). In scenarios with many exit channels, the average coupling, which can be well described by RRKM theory, effectively characterizes the total dissociation rate. However, when only a few, or just one, dissociation channel is available, complex states with particularly weak coupling to the exit channel can dominate the observed ion signal. Due to the nature of our direct detection method, we are more likely to observe complexes with longer lifetimes. Consequently, the measured lifetimes can be orders of magnitude longer than the RRKM lifetime, which is based on the average dissociation rate. This mechanism can lead to a two-to-four-order-of-magnitude enhancement in the effective lifetime in regimes where the number of dissociation channels is close to unity.

Finally, there are threshold effects governed by quantum reflection from

long-range interaction potentials. These effects are particularly significant for higher partial wave channels (p-wave and above), where the complex may become trapped at short range, making tens to hundreds of dissociation attempts before escaping. In contrast, for s-wave dissociation, quantum reflection is much less effective and contributes only modestly to the complex lifetime, typically enhancing it by less than an order of magnitude.

With all the possible explanations presented, it remains challenging to completely resolve the mystery of the bialkali collision complexes. Currently, likely explanations of observations are listed as follows:

Losses in nonreactive systems: In the presence of laser light, photo-excitation loss is likely the dominant mechanism. However, to account for the experimental results observed in the lighter bialkali species in the absence of laser light, one must either assume that the sticking times are orders of magnitude longer than current theoretical predictions or that there exist some fast loss processes that occur even during short-lived complexes [90].

Discrepancy between RRKM and data: From a theoretical perspective, one of the most important open questions concerns the role of nuclear spin degrees of freedom in collisions. One reasonable speculation is that nuclear spins play an active role in complexes when they are long-lived. In addition, they may couple to mechanical angular momenta and contribute to a larger available phase space. In addition, the few-exit-channel effect plays a significant role in enhancing the observed complex lifetimes, especially for ultracold collisions of nonreactive systems.

Electric field and threshold effects: Some experimental results might be explained by a combination of threshold effects and the influence of external electric fields. For example, for pure samples of fermionic $^{23}Na^{40}K$, the p-wave barrier may account for the unusually long sticking times [86]. For experiments involving bosonic $^{23}Na^{39}K$ and $^{23}Na^{87}Rb$, sufficiently strong electric fields could break angular momentum conservation [92]. These effects may also be present in the Rb + KRb collisions, leading to increases in observed complex lifetimes.

4.5 Intermediate complexes in atom-molecule collisions

While the experimental results and theoretical investigations continue to pose significant challenges in understanding bialkali molecule collisions, it seems more logical to first study a simpler system: atom–molecule (alkali-bialkali) collisions, which involve one fewer atom. These systems share many similarities with molecule–molecule collisions, but allow for a more rigorous and tractable theoretical treatment. This, in turn, might help to reveal the underlying mechanisms behind sticky collisions.

In the past decade, full quantum calculations have been performed for systems such as K + KRb (or K_2 + Rb) [58, 96, 97], revealing chaotic behavior in the scattering observables. However, these calculations rely on certain simplifying

assumptions to remain computationally feasible, most notably the neglect of coupling between orbital and spin angular momentum (both electronic and nuclear), as well as the effects of conical intersections. While subtle, these effects may play a crucial role in governing reaction and collision dynamics, as will be discussed further in Chapter 7.

On the experimental side, our setup allows us to study two types of atom–molecule collisions: K + KRb and Rb + KRb. The K + KRb reaction is exothermic and leads to the formation of K_2 and Rb atoms. In contrast, the Rb + KRb system is endothermic and does not yield Rb_2 and K products at ultracold temperatures. For the rest of this chapter, we focus primarily on Rb + KRb collisions as we have not yet systematically explored the K + KRb reaction, largely due to its large exothermicity and the abundance of product channels, which remains a promising direction for future studies.

For the Rb + KRb collisions, when the Rb atoms are prepared in their hyperfine ground state $F = 1, m_F = 1$, and the KRb molecules are in their rovibronic ground state, neither chemical reactions nor inelastic scattering are energetically allowed. As a result, all collisions in this configuration are expected to be elastic.

However, despite the absence of energetically allowed reactive or inelastic channels, we observe near-universal loss between Rb and KRb, similar to what was seen in non-reactive bialkali molecule collisions, as shown in Fig. 4.2. This fast loss of $k_{m,a} = 6.8(7) \times 10^{-11}$ $\mathrm{cm^3 s^{-1}}$ is close to the universal rate of 7.0×10^{-11} $\mathrm{cm^3 s^{-1}}$ [98], suggesting the formation of a long-lived intermediate complex during

the collision process, which may be susceptible to photo-excitation loss, much like the tetra-atomic complexes observed in molecule–molecule collisions.

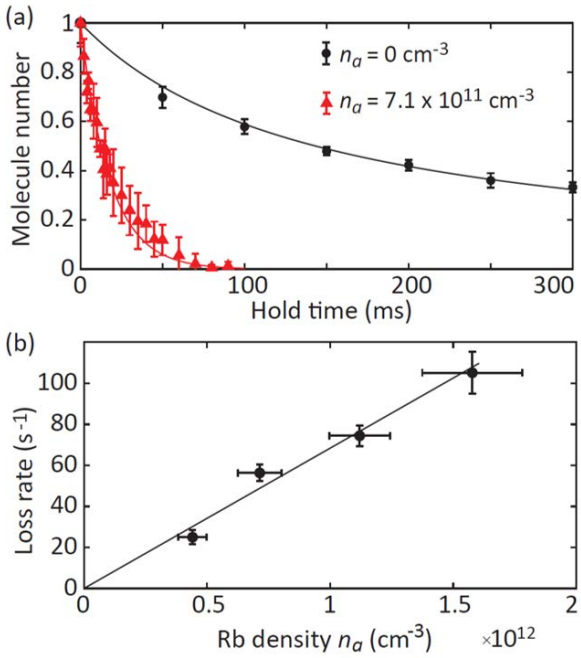

Figure 4.2: Two-body loss in a KRb-Rb mixture [99]. (a) Decay of normalized molecule number for a pure molecular sample (black circles) and a representative atom-molecule mixture (red triangles). (b) Dependence of the loss rate on the atomic density. All data shown are taken with $B = 542$ G in a continuously operated ODT of intensity $I_{tot} = 11.3$ kW/cm^2.

To investigate further, we probed the intermediate complex formed by Rb and KRb using UV ionization with the experimental scheme illustrated in Fig. 4.3.

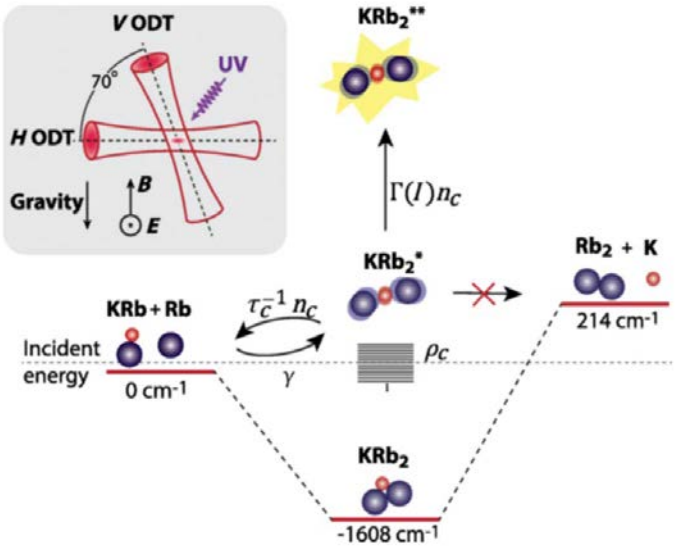

Figure 4.3: Detection scheme of the KRb_2^* complex using UV light [99]. γ denotes the complex formation rate, while τ_c and n_c represent the lifetime and density of the complexes, respectively. $\Gamma(I)$ is the photo-excitation rate, which depends on the UV intensity I. The complexes can either dissociate back into free atoms and molecules or be photo-excited to an electronically excited state, which subsequently dissociates into products with high kinetic energy that escape detection.

In this experiment [99], we prepare approximately 10^4 KRb molecules in their rovibronic ground state, along with Rb atoms in their hyperfine ground state $F = 1, m_F = 1$. The Rb atoms originate from unused atoms left over from the Feshbach association process used to create KRb molecules. At a temperature near 500 nK, the atoms and molecules undergo collisions, forming intermediate KRb_2^* complexes. To detect these complexes, we use a single-photon UV ionization

scheme, since little is known about their internal energy structure. The ionization thresholds for all relevant species in our experiment are shown in Tab. 4.2, based on measurements from [100]. We adapt these values for the Rb + KRb collision, which involves an energy offset compared to the KRb + KRb reaction. The ionization threshold of KRb_2^* is estimated to be around 402 nm. However, due to the low quantum efficiency of laser pulse generation at 402 nm (as illustrated in Fig. 3.1), we chose a shorter wavelength that can still ionize KRb_2^* while leaving other species unaffected. Specifically, we selected a wavelength near 355 nm and performed spectroscopy in this range, as shown in Fig. 4.4.

Species	**PI threshold (nm)**	**PI cross section (Mb)**	**Detector efficiency**
K	285.6	0.01	0.394
Rb	296.8	0.049	0.355
K_2	305.1	0.50 ± 0.25	0.360
Rb_2	317	0.58 ± 0.26	0.310
KRb	310.0–320.3	—	0.331
K_2Rb	374.9	—	0.313
KRb_2	377.6	—	0.295
K_2Rb_2	347.65	—	0.282

Table 4.2: Photoionization (PI) thresholds, PI cross sections, and MCP detector efficiencies for various species [60, 101, 102, 103, 104]

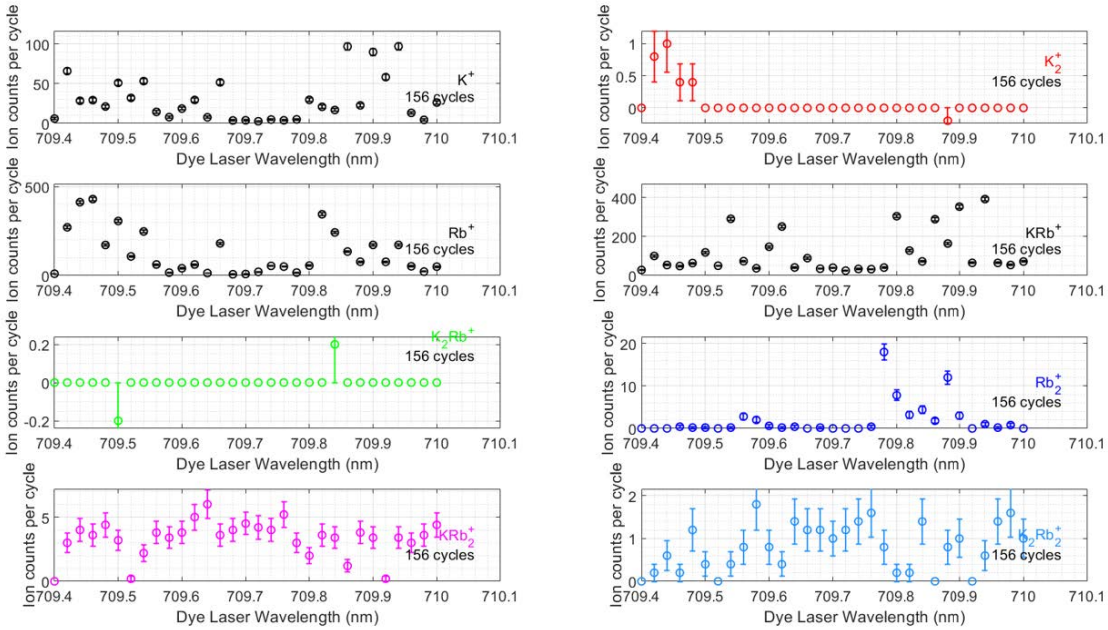

Figure 4.4: UV ionization spectroscopy. The x-axis shows the fundamental wavelength of the dye laser, which is subsequently amplified and frequency-doubled to generate UV light. We scan the presence of all relevant species as a function of the UV laser wavelength to identify a range with high ionization efficiency for KRb_2^* complexes, while minimizing ionization of other species.

After performing UV ionization spectroscopy in the relevant wavelength range, we selected 709.7 nm as the fundamental wavelength of the dye laser. This choice produces a sufficiently strong KRb_2^* signal while avoiding ionization of KRb and Rb atoms. To induce and probe complex formation, we modulated the ODT using a scheme similar to that described in [84], with a repetition rate of 1.5 kHz and a 25% duty cycle, while maintaining the time-averaged intensity equal to that of the

constant ODT configuration.

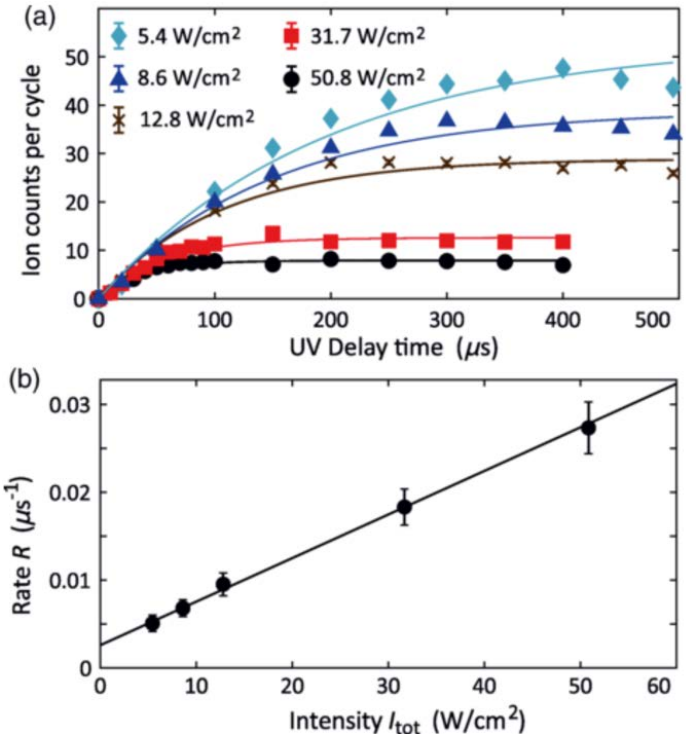

Figure 4.5: Lifetime of the KRb_2^* collision complex [99]. (a) Time evolution of the KRb_2^* complex population, measured via ion signal, after the 1064 nm optical dipole trap (ODT) is turned off. The time-averaged total intensity is held constant across all datasets. The legend shows the residual ODT intensities during its dark phase. (b) Characteristic growth rate of the complex population (the inverse of complex decay rate), extracted from exponential fits to the data in (a), plotted as a function of the corresponding ODT intensity. The solid line represents a linear fit to the data.

At significantly reduced ODT intensity, KRb_2^* complexes begin to accumulate. We probed them using UV light at various delay times after ramping down the

ODT, as shown in Fig. 4.5(a). From these time traces, we extracted characteristic timescales by fitting the growth curves with an exponential functional form. The inverse of these timescales, representing the total decay rate of the complexes, is plotted as a function of the remaining ODT intensity in Fig. 4.5(b).

The data show a linear dependence of the decay rate on the ODT intensity at low intensities, indicating that photo-induced loss is dominated by single-photon excitation processes in this regime. Extrapolating this linear fit to zero intensity yields the decay rate in the absence of ODT light. The inverse of this rate gives the KRb_2^* complex lifetime in the dark, which is determined to be 0.36(3) ms.

To validate that the observed complexes truly originate from Rb + KRb collisions, we measured the number of complexes as a function of Rb atom density n_a, as shown in Fig. 4.6(a). At low densities, the ion signal increases linearly with n_a, which is consistent with two-body Rb–KRb collisions being the dominant formation mechanism, rather than higher-order processes such as three-body interactions. At higher Rb densities, the signal deviates from linearity and eventually saturates. This sublinear behavior is attributed to the increasing loss of KRb molecules at high atomic densities, which limits the accumulation of complexes over time.

In previous studies of KRb + KRb collisions [84], we found that both single-photon and two-photon excitation processes contribute to the loss of complexes. Here, we use a similar approach to probe the KRb_2^* ion signal as a function of total ODT intensity. Assuming both excitation mechanisms exist, the ion signal is

modeled by the following functional form:

$$N_{\text{ion}} = \frac{A}{1 + B_1 I_{\text{tot}} + B_2 I_{\text{tot}}^2}, \tag{4.3}$$

where A is a constant, and B_1 and B_2 represent the rates of single-photon and two-photon excitation, respectively.

By fitting the data with this model (black curve in Fig. 4.6(b)), we extract $B_1 = 0.26(5)$ $(\text{W/cm}^2)^{-1}$ and $B_2 = 0.0008(3)$ $(\text{W/cm}^2)^{-2}$. These results indicate that at low ODT intensities, single-photon excitation dominates the loss process. In contrast, at higher intensities (such as those used in constant traps), two-photon excitation becomes the dominant loss mechanism.

We therefore conclude that we observed an exceptionally long lifetime for the intermediate complex in Rb+KRb collisions. Previous theoretical calculations for KRb_2^* complex lifetimes yield values of 270 ns [105] and ∼1 ns [92], which differ from our measured lifetime of 0.36(3) ms by factors of $\sim 10^3$ and $\sim 10^5$, respectively.

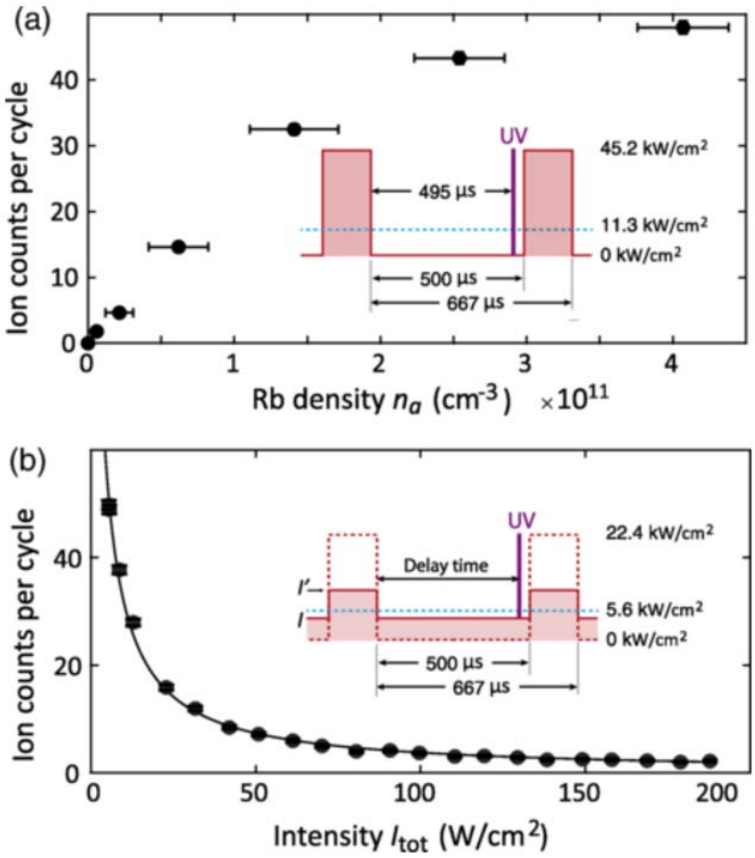

Figure 4.6: Dependence of KRb_2^* collision complexes versus initial atom density and ODT intensity [99]. (a) Steady-state KRb_2^* ion counts measured for different initial atom number densities n_a. The inset shows the timing diagram used for the measurement. (b) Steady-state KRb_2^* ion counts measured at different total ODT intensities, normalized by the number of experimental cycles. The solid line is a fit to the data using Eq. (2).

Among the possible explanations discussed for the discrepancy with RRKM

predictions, a few candidates appear especially relevant in the context of Rb + KRb collisions. One possibility is that the RRKM model itself breaks down entirely for atom–molecule collisions, where the density of states is significantly lower than in molecule–molecule collisions. While this argument might hold, it remains difficult to test directly, as no alternative theoretical framework currently exists—full quantum dynamics calculations that include essential effects such as spin-rotation coupling and conical intersections are not yet available.

Within the RRKM framework, one might argue that angular momentum conservation breaks down due to external fields, as proposed in [92]. In this scenario, the enhancement in the density of states would explain the extended complex lifetime. However, a quantitative prediction of the critical electric field strength at which this effect becomes significant for Rb-KRb collisions has yet to be performed. Nevertheless, this inspired us to probe the field dependence of complex lifetimes to validate this theory.

Another possibility is the activation of hyperfine degrees of freedom within the complex. In KRb + KRb collisions, nuclear spin conservation has been experimentally confirmed throughout the reaction process [36]. However, the Rb + KRb system differs fundamentally due to the presence of an unpaired electron in Rb, which may result in stronger couplings to nuclear spin states. Indeed, we find that the hyperfine degree of freedom is active in Rb ($F = 2, m_F = 2$) + KRb ($N = 0$) collisions, a case that will be explored in detail in Chapter 7.

To directly test whether hyperfine mixing plays a role in the extended

KRb_2^* lifetime, we compared measurements for two different KRb nuclear spin configurations. Specifically, we prepared KRb in its lowest hyperfine state, $|m_I^{\mathrm{K}} = -4, m_I^{\mathrm{Rb}} = 3/2\rangle$, while keeping Rb in $|F = 1, m_F = 1\rangle$. In this configuration, inelastic collisions involving nuclear spin flips are energetically forbidden, and the entrance channel serves as the only dissociation pathway. At 17 V/cm and 30 G—the same electric and magnetic fields used in earlier measurements—the extracted KRb_2^* lifetime agrees, within experimental uncertainty, with that of the $|m_I^{\mathrm{K}} = -4, m_I^{\mathrm{Rb}} = 1/2\rangle + |F = 1, m_F = 1\rangle$ configuration. This suggests that the complex lifetime is not sensitive to the KRb nuclear spin state. Additional examples and comparisons will be presented in the following section.

Finally, the few-exit-channel theory proposed in Ref. [95] is consistent with our observations, offering a potential explanation for the discrepancy of two to four orders of magnitude between the measured lifetimes and RRKM predictions. However, direct experimental validation of this theory remains challenging.

4.6 Complex lifetime vs initial state and external fields

To extend our understanding of the unexpectedly long KRb_2^* complex lifetime, we begin to systematically vary the experimental parameters available in the Rb + KRb system, while awaiting complementary evidence from other platforms and more

advanced theoretical models that can explain the observations. In this section, we focus on measurements of the KRb_2^* complex lifetime under different initial quantum states of Rb and KRb, as well as under varying external electric and magnetic fields.

We begin by exploring the complex lifetime as a function of the Rb hyperfine state. In our previous work [99], Rb atoms were prepared in their lowest-energy state, $|F = 1, m_F = 1\rangle$. Here, we transfer the atoms to other $F = 1$ states or the $F = 2$ manifold. Within $F = 1$, the $|F = 1, m_F = 0\rangle$ and $|F = 1, m_F = -1\rangle$ states lie higher in energy than $|F = 1, m_F = 1\rangle$ by 0.7 MHz/G and 1.4 MHz/G, respectively. Meanwhile, all $F = 2$ states are approximately 6.8 GHz above the $|F = 1, m_F = 1\rangle$ state at low magnetic fields.

Following the intuition provided by RRKM theory, increasing the energy of the initial state leads to a larger number of energetically allowed exit channels. One would therefore expect a decrease in the complex lifetime when Rb atoms are placed in these higher-energy hyperfine states.

In this measurement, we further reduced the ODT modulation frequency from 1.5 kHz to 833 Hz, allowing us to probe the complex formation and dissociation dynamics in the dark for durations up to 0.9 ms, as shown in Fig. 4.7(a). This extended probing time improves the accuracy of our lifetime measurements. Further reduction of the modulation frequency would cause severe parametric heating, preventing us from extending the dark time.

To transfer atoms from the $|F = 1, m_F = 1\rangle$ state to $|F = 1, m_F = 0\rangle$, we use

a microwave ARP sequence: first, a π-transition to $|F = 2, m_F = 1\rangle$, followed by a σ^- transition to $|F = 1, m_F = 0\rangle$. Similarly, preparation of the $|F = 1, m_F = -1\rangle$ state is performed via the intermediate state $|F = 2, m_F = 0\rangle$, using two sequential σ^- transitions. In both cases, we remove the residual $|F = 1, m_F = 1\rangle$ atoms by applying a microwave pulse resonant with the $|F = 1, m_F = 1\rangle \rightarrow |F = 2, m_F = 2\rangle$ transition. This removal method relies on the fact that atoms in the $F = 2$ manifold do not form long-lived complexes with KRb on timescales of microseconds. This has been confirmed experimentally by the absence of KRb_2^* ion counts in UV ionization measurements of $|F = 2\rangle$ Rb + KRb collisions.

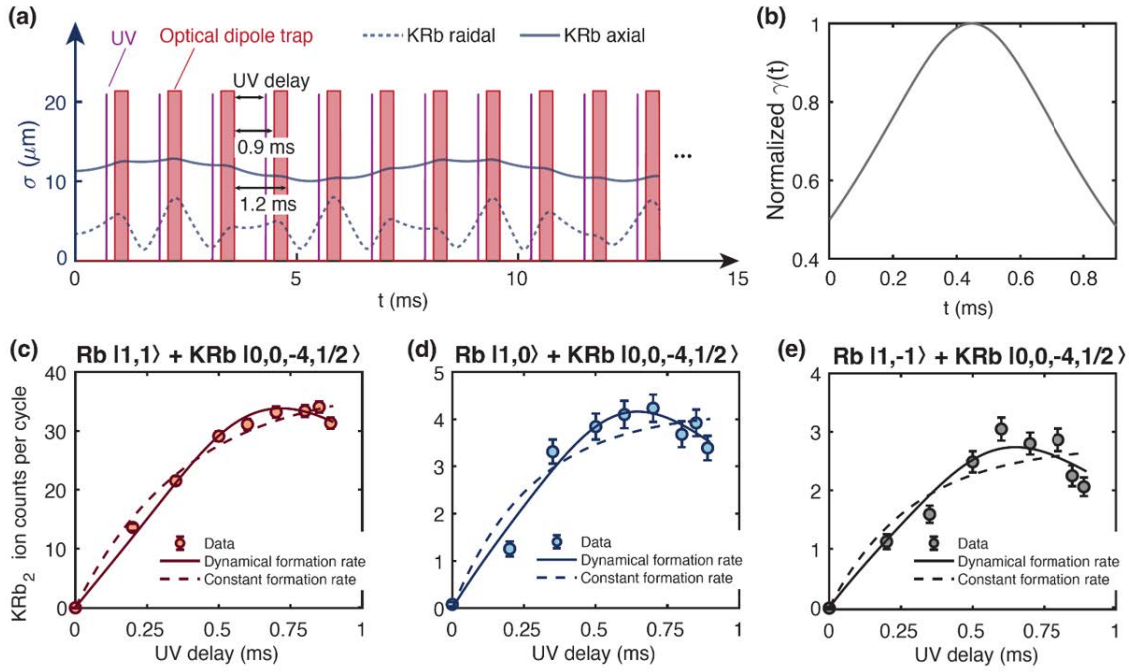

Figure 4.7: Measurement of the KRb_2^* complex lifetime for Rb atoms prepared in the $|F = 1, m_F = 1\rangle$, $|F = 1, m_F = 0\rangle$, and $|F = 1, m_F = -1\rangle$ states, using a modulated ODT at 833 Hz with a 25% duty cycle (unpublished data). (a) Modulation scheme of the ODT. (b) Due to variations in the average KRb–Rb cloud sizes during the modulation cycle, the complex formation rate γ becomes time-dependent, contrary to the constant-rate assumption used in previous work. (c)–(e) KRb_2^* ion signals as a function of the delay time between the ODT ramp-down and the UV ionization pulse for the three different Rb initial states. Two fitting models are shown: solid curves account for a time-dependent formation rate γ, while dashed curves assume a constant γ.

At a trap modulation frequency of 833 Hz, even though parametric heating

of Rb and KRb is not severe, the modulation causes the atom–molecule clouds to undergo contractions and expansions. In our previous study[99], this effect was neglected when the modulation frequency was significantly higher than the trap frequency. However, in our experiment, the trap frequencies are only ∼200 Hz, making this approximation less accurate.

To model the dynamics of the Rb and KRb clouds in the modulated ODT, we perform a Monte Carlo simulation that tracks the motion of a large ensemble of non-interacting particles. We begin by generating 3000 Rb atoms and 3000 KRb molecules at temperatures of 800 nK and 400 nK, respectively. The Rb atoms are hotter than KRb molecules because they originate from the hotter residual atoms from the molecule creation process via magneto-association, which preferentially converts the colder atoms into molecules. The initial positions and velocities are sampled from a Maxwell–Boltzmann distribution inside a 3-dimensional harmonic trap with trapping frequencies of $2\pi \times (212, 212, 63)$ Hz for Rb and $2\pi \times (250, 250, 72)$ Hz for KRb.

We simulate the evolution of the particles over 50 cycles of ODT modulation classically. Each cycle consists of 900 μs of free expansion (ODT off) followed by 300 μs of harmonic confinement (ODT on). Given the 25% duty cycle, the trap intensity during the bright time is increased by a factor of 4, so the trapping frequencies are taken to be twice the initial values in these intervals.

Our primary goal is to determine the average complex formation rate during the ODT dark time, as the UV ionization beam probes the complex population

at a delay time t after the ODT is turned off, averaged over multiple modulation cycles. For each delay time t, we extract the sizes of the Rb and KRb clouds in all three dimensions (x, y, z) over the 50 modulation cycles. Because both Rb and KRb clouds maintain Gaussian spatial profiles, we use the standard deviation of the coordinate spread in each direction to quantify the cloud sizes. The results show that the cloud sizes initially decrease after the ODT is turned off, and then gradually increase due to free expansion. This effect is more pronounced along the tightly trapped dimensions, where the ratio of ODT modulation frequency to trap frequency is smaller.

The average complex formation rate can also be calculated by averaging over 50 ODT modulation cycles. Specifically, the complex formation rate at a given time t is proportional to the spatial overlap integral of the Rb and KRb density distributions, expressed as:

$$\gamma(t) = k_{\text{col}} \int n_{\text{Rb}}(\mathbf{r}, t)\, n_{\text{KRb}}(\mathbf{r}, t)\, dV \tag{4.4}$$

Assuming Gaussian spatial profiles, the density distribution of each species along dimension x_i is given by:

$$n_{x_i,s}(t) = n_{x_i} \exp\left(-\frac{x_i^2}{2\sigma_{x_i,s}^2(t)}\right) \tag{4.5}$$

where $x_i \in \{x, y, z\}$ and $s \in \{\text{Rb}, \text{KRb}\}$. The standard deviation $\sigma_{x_i,s}(t)$

characterizes the time-dependent cloud size in each spatial dimension. Performing the full integral over space yields the complex formation rate:

$$\gamma(t) \propto \prod_i \frac{1}{\sqrt{\sigma_{i,\mathrm{Rb}}^2(t) + \sigma_{i,\mathrm{KRb}}^2(t)}} \tag{4.6}$$

We compute $\gamma(t)$ at each delay time t by averaging over 50 modulation cycles, as shown in Fig. 4.7(b). As expected, the average complex formation rate $\gamma(t)$ is anti-correlated with the sizes of the Rb and KRb clouds.

This time-dependent formation rate is used in the complex lifetime fitting model. It significantly improves the agreement between theory and experiment compared to exponential fits assuming a constant formation rate, as shown in Fig. 4.7(c)-(e).

Note that we choose to average over 50 modulation cycles here, which is sufficient to capture the dynamics accurately. While averaging over more cycles is possible, it does not significantly affect the final results.

To measure the KRb_2^* complex lifetimes in the absence of light, we follow a similar approach to that described in Ref. [99], in which the effective lifetimes are measured at several residual ODT intensities and extrapolated to $I_{\mathrm{ODT}} = 0$. This extrapolation is necessary because a small amount of leakage light on the order of a few W/cm^2 is always present in the experiment. For this measurement, we select five different ODT intensities for the $|1,1\rangle$ and $|1,0\rangle$ Rb hyperfine states. Due to limited signal strength in the $|1,-1\rangle$ state, we probe it only at the lowest ODT

intensity. The $|1,1\rangle$ and $|1,0\rangle$ data each yield linear trends with nearly identical slopes, corresponding to the photoexcitation rate of the complex. This agreement experimentally confirms that the complex photoexcitation rate is independent of the Rb hyperfine state. By extrapolating to zero ODT intensity, we extract the intrinsic complex lifetimes in the dark: 625(53) μs for $|1,1\rangle$ and 357(21) μs for $|1,0\rangle$. Assuming the same photoexcitation rate applies, we infer a lifetime of 356(108) μs for the $|1,-1\rangle$ state.

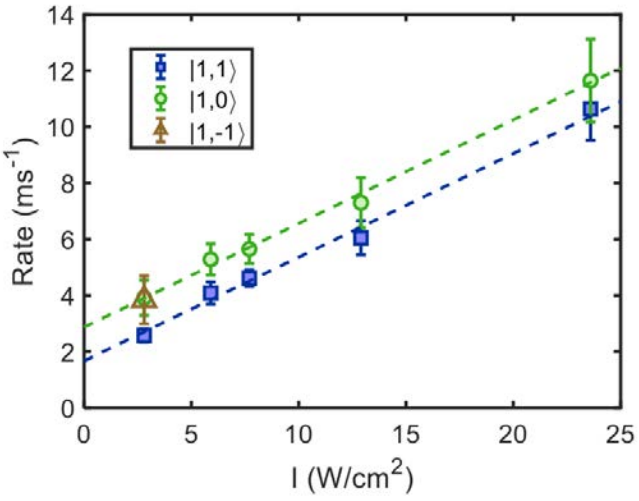

Figure 4.8: Total loss rate of the KRb_2^* intermediate complex as a function of residual ODT intensity (unpublished data). The dark-phase ODT intensity is varied by changing the modulation depth while maintaining a constant time-averaged intensity. Rb atoms are prepared in three different hyperfine states: $|1,1\rangle$ (blue squares), $|1,0\rangle$ (green circles), and $|1,-1\rangle$ (brown triangles). The dashed lines are linear fits to the data, constrained to have the same slope. All measurements are performed under an electric field of $E = 17$ V/cm and a magnetic field of $B = 30$ G.

Compared to the case where Rb is prepared in its lowest hyperfine state, the complex lifetime is reduced by approximately a factor of two when Rb is initialized in the $|1,0\rangle$ state. This observation is qualitatively consistent with RRKM theory, which predicts that the complex lifetime is inversely proportional to the number of energetically allowed exit channels. Naively, a Rb atom in the $|1,0\rangle$ state can dissociate to both $|1,0\rangle$ and $|1,1\rangle$ final states, whereas a Rb atom in $|1,1\rangle$ has only a single available dissociation channel. In theory, a more accurate analysis involves calculating the dissociation rates from each complex state to all energetically accessible atom–molecule exit channels, which the naive model assumes to be identical. We developed a simple model based on angular momentum coupling, which will be discussed later in this section.

$\lvert F_a, m_{F_a}\rangle$	$\lvert N, m_N, m_I^{\mathrm{K}}, m_I^{\mathrm{Rb}}\rangle$	τ_c (μs)
$\lvert 1,1\rangle$	$\lvert 0,0,-4,3/2\rangle$	609(106)
	$\lvert 0,0,-4,1/2\rangle$	625(53)
	$\lvert 0,0,-3,-1/2\rangle$	610(49)
	$\lvert 0,0,-4,-3/2\rangle$	702(80)
$\lvert 1,0\rangle$	$\lvert 0,0,-4,1/2\rangle$	357(21)
	$\lvert 0,0,-4,-3/2\rangle$	407(54)
$\lvert 1,-1\rangle$	$\lvert 0,0,-4,1/2\rangle$	356(108)
	$\lvert 0,0,-4,-3/2\rangle$	398(43)
$\lvert 1,1\rangle$	$\lvert 1,0,-4,3/2\rangle$	≤ 2.66
$\lvert 2,2\rangle$	$\lvert 0,0,-4,1/2\rangle$	≤ 1.54

Table 4.3: KRb_2^* complex lifetime for different initial state combinations of Rb and KRb at $B = 30$ G (unpublished data). Lifetimes are extrapolated from measurements taken at a minimum ODT intensity of 2.7 W/cm^2, assuming equal photoexcitation rates across all initial state combinations. For cases where the complex lifetime is very short, direct measurement is not possible, and only upper bounds can be set.

Before introducing our model, we extend our dataset by varying the KRb hyperfine state to enable a more comprehensive analysis. In this measurement, KRb molecules are transferred from the initial $|0,0,-4,1/2\rangle$ state to several other hyperfine states ($|0,0,-3,-1/2\rangle$, $|0,0,-4,-3/2\rangle$, $|0,0,-4,3/2\rangle$ and $|1,0,-4,3/2\rangle$), and the resulting complex lifetimes are recorded, as summarized in Tab. 4.3. These

KRb hyperfine states differ in energy by up to 100 kHz at a magnetic field of 30 G, which is above the typical collision energy of 20 kHz.

Interpreting the results is not straightforward. The observed consistency in complex lifetimes across different KRb hyperfine states suggests that the KRb nuclear spins may not influence the complex dynamics. Therefore, even though higher-energy hyperfine states allow additional exit channels to be energetically accessible, there may be no physical mechanism to effectively couple to those states. However, this interpretation is unsatisfying, especially given that nuclear spins are known to play a role in Rb + KRb collisions when Rb is prepared in the $|2, 2\rangle$ state [77], where the complex lifetime is estimated to be as short as 0.5 ns. It seems unlikely that nuclear spins are inactive in the current case, where the lifetime is six orders of magnitude longer.

An alternative explanation is that nuclear spins do participate in the short-range dynamics. In that scenario, the effective number of exit channels cannot vary significantly across different initial KRb hyperfine states. This is tied to how exit channels should be counted, a point we now examine in more detail.

We propose two models to estimate the number of allowed exit channels, both based on angular momentum algebra and the assumption that the dissociation rate from a complex state to an exit channel is proportional to the square of their angular momentum wavefunction overlapping, which is the square of the Clebsch–Gordan coefficient. The first model assumes that the nuclear spins of KRb do not actively participate in the complex dynamics, while the second explicitly includes them.

Although this assumption may not fully capture the complexity of the dissociation process, it serves as a helpful starting point for modeling the role of angular momentum coupling in complex decay.

To begin, we define the relevant angular momenta involved in the exit channels as follows:

$$\mathbf{N} : \text{Molecular rotation} \tag{4.7}$$

$$\mathbf{L} : \text{Partial wave (orbital angular momentum)} \tag{4.8}$$

$$\mathbf{F}_a : \text{Hyperfine angular momentum of the Rb atom} \tag{4.9}$$

$$\mathbf{I}_1 : \text{Nuclear spin of K in the KRb molecule} \tag{4.10}$$

$$\mathbf{I}_2 : \text{Nuclear spin of Rb in the KRb molecule} \tag{4.11}$$

Both models are based on decomposing the initial state into coupled complex states $|c\rangle$, labeled by the total angular momentum $\mathbf{J}$ of the complex and its projection $\mathbf{m_J}$ along the quantization axis. In addition to the total angular momentum and its projection, it is necessary to specify the intermediate quantum numbers by tracking the coupling process as two angular momenta are added each time. For example, if $J = J_1 + J_2 + J_3$, the quantum state should be properly labeled as $|J, m_J, J_1, J_2, J_3, J_{12}\rangle$, where $J_{12} = J_1 + J_2$ is the intermediate angular momentum formed by adding J_1 and J_2. This state-counting approach was used in our previous estimation of the $K_2Rb_2^*$ complex lifetime using RRKM theory [84]. In that analysis, where $J = N_{K_2} + N_{Rb_2} + L$ and $N_{tot} = N_{K_2} + N_{Rb_2}$, each complex state labeled

by $|J, m_J, N_{\mathrm{K}_2}, N_{\mathrm{Rb}_2}, L, N_{\mathrm{tot}}\rangle$ maps directly to a single exit channel. This labeling is particularly convenient, as the complex states correspond directly to observable product states labeled by $(N_{\mathrm{K}_2}, N_{\mathrm{Rb}_2})$, and the degeneracy of each exit channel can be determined by counting the allowed combinations of L and N_{tot} for each product pair.

The situation is, however, very different in the case of atom–molecule collisions, primarily due to the non-negligible Zeeman shifts arising from the atom's unpaired electron. In this context, the atomic Zeeman state $|F, m_F\rangle$ must be explicitly considered to determine whether an exit channel is energetically accessible. As a result, the exit channels are labeled in the uncoupled basis as $|F_a, m_{F_a}\rangle \otimes |N, m_N, m_{I_{\mathrm{K}}}, m_{I_{\mathrm{Rb}}}\rangle$. This labeling contrasts with the coupled basis used in the KRb + KRb system, where product states map directly onto complex states. Consequently, a basis transformation is required to relate the complex states to the asymptotic exit channels in atom–molecule collisions.

The basis transformation is performed by decomposing each complex state into all exit channel states. The dissociation rate of a given complex state is then assumed to be proportional to the total probability of overlap with these exit channels, quantified by the sum of $|\langle \mathrm{complex}|\mathrm{exit}\rangle|^2$ over all exit states $|\mathrm{exit}\rangle$. A similar treatment has been used in our recent work [77].

Model 1: Counting model without KRb nuclear spins engaged

We first present the model in which the KRb nuclear spins are not actively coupled. In this case, conservation of total angular momentum imposes the constraint:

$$\mathbf{F}_a + \mathbf{N} + \mathbf{L} = \mathbf{F}'_a + \mathbf{N}' + \mathbf{L}' \tag{4.12}$$

Here, unprimed quantities refer to the reactants and primed ones to the products. Given that the initial KRb rotational state is $N = 0$, rotational excitation of the products is energetically forbidden ($N' = 0$), and the collision proceeds via an s-wave ($L = 0$), the total angular momentum conservation condition simplifies to:

$$\mathbf{F}_a = \mathbf{F}'_a + \mathbf{L}' \tag{4.13}$$

An additional constraint originates from parity conservation, which can be expressed as:

$$(-1)^{N+L} = (-1)^{N'+L'} \tag{4.14}$$

Because $N = L = 0$ initially and $N' = 0$ by energy conservation, angular momentum and parity conservation require the final orbital angular momentum L' to be even. Therefore, given the aforementioned constraints, we can list the available exit channels.

- For the initial state $|1,1\rangle$ ($F_a = 1, m_{F_a} = 1$), only one dissociation channel is allowed:

$$|F_a' = 1, m_{F_a}' = 1, L' = 0, m_L' = 0\rangle$$

- For the initial state $|1,0\rangle$ ($F_a = 1, m_{F_a} = 0$), two dissociation channels are allowed:

$$|F_a' = 1, m_{F_a}' = 0, L' = 0, m_L' = 0\rangle$$

$$|F_a' = 1, m_{F_a}' = 1, L' = 2, m_L' = -1\rangle$$

- For the initial state $|1,-1\rangle$ ($F_a = 1, m_{F_a} = -1$), three dissociation channels are allowed:

$$|F_a' = 1, m_{F_a}' = -1, L' = 0, m_L' = 0\rangle$$

$$|F_a' = 1, m_{F_a}' = 0, L' = 2, m_L' = -1\rangle$$

$$|F_a' = 1, m_{F_a}' = 1, L' = 2, m_L' = -2\rangle$$

We note that in this picture, we implicitly consider that different complex states have different lifetimes, which is one of the key ideas in the 2023 paper [95] by Croft, Bohn, and Quemener. However, when the nuclear spins of KRb are not involved, there is only a single complex total angular momentum state.

After considering the spin wavefunction overlap (essentially Clebsch–Gordan coefficients) between the complex state to the asymptotic states, the effective number of dissociation channels are $1 : 1.3 : 1.9$ for $F_a = 1, m_{F_a} = 1$, $F_a = 1, m_{F_a} = 0$ and

$F_a = 1, m_{F_a} = -1$. This ratio does not precisely match the experimentally observed lifetimes, but it remains within the correct ballpark.

Here, we note that the energy released in m_{F_a}-changing collisions is sufficient to overcome the centrifugal barrier associated with $L' = 2$ [106].

Model 2: Counting model with KRb nuclear spins engaged

If we assume the nuclear spins in KRb are allowed to change freely while total angular momentum is conserved, the conservation condition becomes:

$$\mathbf{F}_a + \mathbf{N} + \mathbf{L} + \mathbf{I_1} + \mathbf{I_2} = \mathbf{F}'_a + \mathbf{N}' + \mathbf{L}' + \mathbf{I}'_\mathbf{1} + \mathbf{I}'_\mathbf{2} \tag{4.15}$$

Similar to the previous case, we assume $N = N' = 0$ and $L = 0$. The nuclear spins of K and Rb are $I_{\mathrm{K}} = 4$ and $I_{\mathrm{Rb}} = 3/2$, respectively. Due to the parity constraint, L' must be even. Additionally, the finite energy released when Rb changes its Zeeman state in a magnetic field of 30 G limits the accessible partial waves. In particular, we restrict L' to 0, 2, or 4, as higher partial waves introduce centrifugal barriers that exceed the available energy, thereby suppressing product formation. We then enumerate all energetically allowed exit channels, labeled by $|F_a, m_{F_a}\rangle \otimes |N, m_N, m_{I_{\mathrm{K}}}, m_{I_{\mathrm{Rb}}}\rangle$, and compute the angular momentum wavefunction overlaps between these exit channels and the complex states to estimate the relative dissociation probabilities. Essentially, we calculate the KRb_2^* complex population buildup profile using Eq. 4.16, by summing over all complex states i, each of which

follows an individual exponential buildup profile.

We first present the expected exponential buildup profiles for $F = 1$ Rb colliding with KRb in the $|0, 0, -4, 1/2\rangle$ state, as shown in Fig. 4.9. Interestingly, although the number of exit channels counted in $|F, m_F, I_{\mathrm{K}_2}, I_{\mathrm{Rb}_2}\rangle$, for the $|1, 1\rangle$, $|1, 0\rangle$, and $|1, -1\rangle$ initial states have a ratio of $1 : 19 : 33$, the resulting complex lifetimes exhibit a much less extreme ratio of approximately $13.5 : 8.2 : 2.2$. This ratio does not quantitatively match the experimentally observed lifetimes but remains within the correct ballpark, suggesting that even when nuclear spins are active, their impact on the complex lifetime may be less significant than one might naively expect.

$$n_c(t) = \sum_i p_i \tau_i (1 - e^{-t/\tau_i}) \tag{4.16}$$

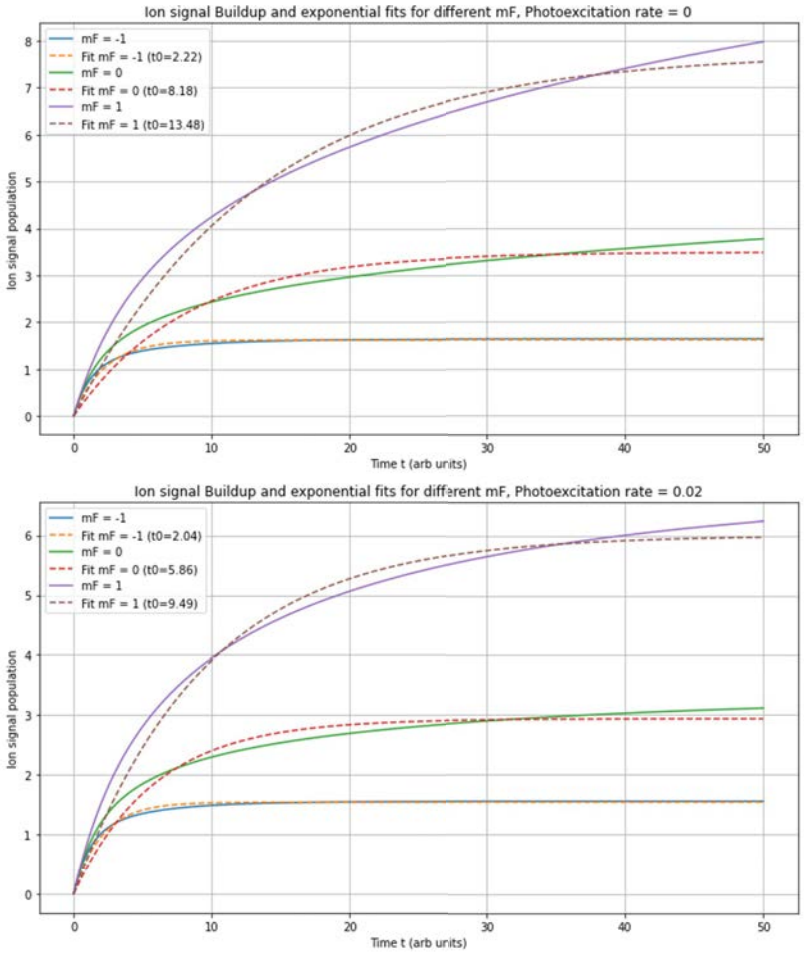

Figure 4.9: Simulated complex population growth for Rb in the $|1,1\rangle$, $|1,0\rangle$, and $|1,-1\rangle$ states. The KRb state is $|0,0,-4,1/2\rangle$. The dashed lines represent fits using a single exponential buildup function.

We then vary the KRb hyperfine state while keeping Rb fixed in the $|1,1\rangle$ state. Using the same set of KRb states studied experimentally, the results are shown in Fig. 4.10. Interestingly, similar to our approach in analyzing Rb hyperfine

dependence, the number of exit channels, counted in the $|F, m_F, I_{K_2}, I_{Rb_2}\rangle$ basis, has a ratio $1:1:1:2$ for the $|0,0,-4,1/2\rangle$, $|0,0,-4,3/2\rangle$, $|0,0,-4,-3/2\rangle$, and $|0,0,-3,-1/2\rangle$ states, respectively. Our simulation predicts a lifetime ratio of approximately $13.5:14.2:4.8:15.1$ across these four cases.

Although these predicted lifetimes fall within the same order of magnitude, they differ from experimental observations, where all four configurations exhibit nearly identical lifetimes. Two particularly interesting points emerge: 1. the stretched state $|0,0,-4,-3/2\rangle$ is predicted to have a shorter lifetime than measured experimentally in the state counting model, and 2. in naive RRKM theory, the $|0,0,-3,-1/2\rangle$ state, with twice as many exit channels, is expected to have a noticeably shorter lifetime than the others, yet our model predicts a similar lifetime, which better aligns with experimental results.

One common feature worth noting is that our detection method inherently favors long-lived complex states, which tend to dominate the fits used to extract complex lifetimes. However, it has not been experimentally confirmed that multiple distinct complex lifetimes exist, nor is there a clear understanding of the coupling between complex states and asymptotic product channels. In our model, these couplings are approximated using the angular momentum wavefunction overlap between complex states, defined by a specific set of quantum numbers, and the exit channels. Despite these simplifications, our state-counting approach can capture some essential aspects of the physics responsible for the remarkably long-lived complexes observed in ultracold collisions. Further experimental tests are needed to

validate and improve this framework.

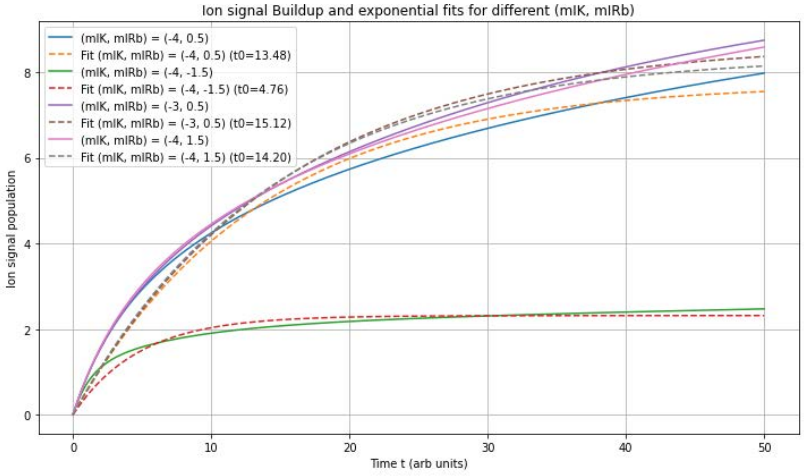

Figure 4.10: Simulated complex population growth for KRb in the $|0, 0, -4, 1/2\rangle$, $|0, 0, -4, 3/2\rangle$, $|0, 0, -4, -3/2\rangle$, and $|0, 0, -3, -1/2\rangle$ states. The Rb state is fixed to $|1, 1\rangle$. The dashed lines represent fits using a single exponential buildup function.

In addition, we investigate the electric field dependence of the complex lifetime, motivated by theoretical predictions [94, 93] suggesting that mixing of rotational states within the complex and the breaking of angular momentum conservation can both contribute to increased lifetimes with increasing electric field. Experimentally, we test this by measuring the complex lifetimes of the Rb $|1, 1\rangle$ + KRb $|0, 0, -4, 1/2\rangle$ state pair in electric fields ranging from approximately 0 V/cm to 1.6 kV/cm, with a magnetic field fixed at 2 G. As shown by the black line in Fig. 4.11(a), we observe that the lifetime increases by roughly a factor of three from 0 to 500 V/cm, then saturates at higher fields. These results indicate that complex lifetimes are influenced

by electric field strength, matching the trend predicted by theoretical expectations. Between the two models, the mixing of rotation states in the complex agrees better with our data, since it predicts a moderate increase (by an order of magnitude or so) at the experimental electric field range. However, this does not rule out the possibility of angular momentum conservation breaking, which happens at higher electric fields (probably over 10 kV/cm) that could lead to a more dramatic change in the complex lifetime. Even with the two models, the quantitative prediction of this dependence remains an open challenge, as exact calculations of complex lifetimes under different electric fields have yet to be performed for the Rb-KRb system.

Another noteworthy observation is that at a slightly higher magnetic field of 30 G, the complex lifetime exhibits no measurable dependence on electric field across the range of 0 to 1.6 kV/cm, as shown by the gray line in Fig. 4.11(a). This behavior is consistent with our previous findings [99], where the lifetimes measured at 17 V/cm and 343 V/cm under a 30 G field were found to be nearly identical, and comparable to those observed at high electric fields in the 2 G case. The interpretation of this phenomenon remains unclear, but we list two possible directions to explore: 1. The magnetic field may induce mixing among complex states, similar to the role of the electric field, and 2. the coupling between complex states and available exit channels may be magnetic-field dependent, thereby influencing the dissociation dynamics.

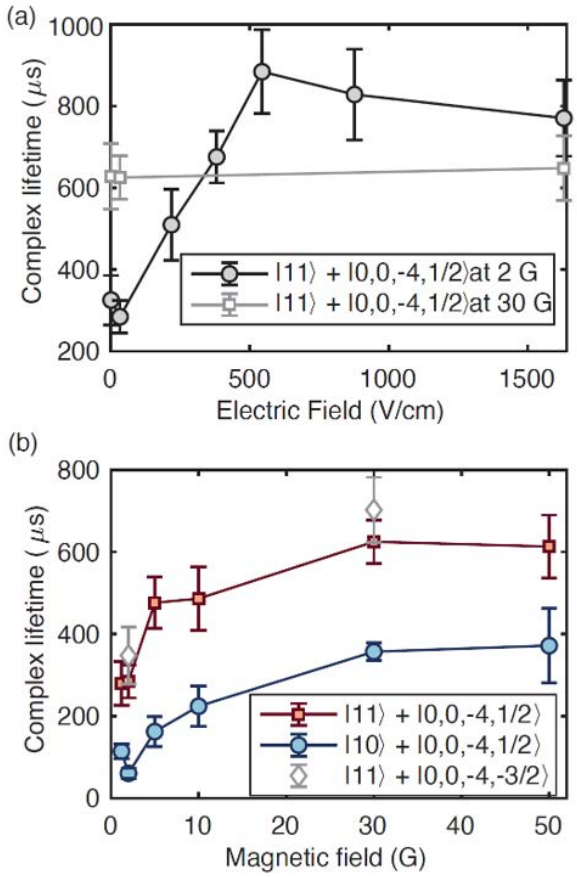

Figure 4.11: Complex lifetime measured at different electric and magnetic fields (unpublished data). (a) Complex lifetime as a function of electric field. Black circles correspond to measurements at 2 G with Rb in the $|1,1\rangle$ state and KRb in the $|-4,1/2\rangle$ state. Light gray squares show measurements at 30 G with the same initial states. Note that for magnetic fields $B \leq 10$ G, m_I^{K} and m_I^{Rb} are no longer good quantum numbers, and the molecular state is an eigenstate represented as a superposition of $|-4,1/2\rangle$, $|-3,-1/2\rangle$, and $|-2,-3/2\rangle$. However, we continue to label states using their high-field quantum numbers for consistency, as they evolve diabatically during magnetic field ramps. (b) Complex lifetime as a function of magnetic field, measured at a fixed electric field of 17 V/cm.

Between the two theoretical frameworks, the model based on rotational state mixing within the complex predicts a relatively weak dependence of complex lifetime on electric field. This effect typically manifests as a lifetime increase by a factor of unity to one order of magnitude, with a characteristic field strength of approximately 1 kV/cm [107], both of which are broadly consistent with our observations. However, this mechanism alone cannot account for the five orders of magnitude discrepancy between experimental lifetimes and RRKM predictions.

In contrast, the theory that allows for the breaking of total angular momentum conservation, both in magnitude and projection along the quantization axis, can lead to a substantial enhancement in the density of states, potentially resolving the long lifetime puzzle. However, we do not observe a sharp reduction in complex lifetime down to electric fields as low as 1 V/cm. Interestingly, while the critical electric field for angular momentum breaking in the Rb + KRb system has not yet been reported, it has been estimated to be 14.8 kV/cm for the NaK + K system [94]. For KRb + Rb, the threshold is likely to be in a similar range, with two competing effects: the smaller dipole moment of KRb tends to increase the critical field, while the larger reduced mass of the KRb + Rb system compared to NaK + K likely lowers it. These considerations suggest that the electric field required to break angular momentum conservation has likely not been reached in our experiments.

Finally, we explore the magnetic field dependence of complex lifetimes. So far, no theoretical predictions have been made on this topic, and our interpretation is based solely on our observations. Experimentally, we vary the magnetic field between

1 G and 50 G and measure the complex lifetimes for three initial state combinations: Rb $|1,1\rangle$ + KRb $|0,0,-4,1/2\rangle$, Rb $|1,0\rangle$ + KRb $|0,0,-4,1/2\rangle$, and Rb $|1,1\rangle$ + KRb $|0,0,-4,-3/2\rangle$, as shown in Fig. 4.11(b). In all three cases, we observe a gradual increase in the complex lifetime by a factor of 2 to 3 as the magnetic field increases, resembling the trend observed in the electric field dependence from low to high field.

While we do not currently have a definitive explanation for the magnetic field dependence of the complex lifetime, we can still examine our results to gain some insight. First, if total angular momentum is conserved during the collision, both the Rb $|1,1\rangle$ + KRb $|0,0,-4,1/2\rangle$ and Rb $|1,1\rangle$ + KRb $|0,0,-4,-3/2\rangle$ combinations must dissociate back through the original incoming channel due to energy conservation, even if the nuclear spins of KRb are allowed to change. The fact that these two combinations exhibit similar trends suggests that the observed magnetic field dependence likely does not originate from changes in the dissociation energy with magnetic field, but rather from the intrinsic dissociation rate of the complex to the exit channels.

On the other hand, if we relax the assumption of total angular momentum conservation, a different picture emerges. At lower magnetic fields, the energy spacing between different KRb nuclear spin states decreases significantly, from tens of kilohertz at 30 G to just a few kilohertz at 1 to 2 G, which falls below the thermal energy of the collisions. As a result, more exit channels become energetically accessible at lower fields, which could account for the reduction in complex lifetime.

However, this explanation is not consistent with the observed data: the complex lifetimes in the three cases shown in Fig. 4.11(b) differ only mildly, even though the Rb $|1,1\rangle$ + KRb $|0,0,-4,-3/2\rangle$ and Rb $|1,0\rangle$ + KRb $|0,0,-4,1/2\rangle$ combinations are expected to allow orders of magnitude more exit channels than the Rb $|1,1\rangle$ + KRb $|0,0,-4,1/2\rangle$ case.

4.7 Feshbach resonances in Rb-KRb system

The puzzling features of the KRb_2^* complex lifetimes motivate further investigation into the inelastic collision loss rates between Rb and KRb under various conditions. Several important questions arise: 1. Do Rb + KRb collisions follow a universal loss rate? 2. Can we observe distinct magnetic Feshbach resonances, similar to those reported in NaLi + Na and NaK + K systems [108, 109, 110], or do Rb + KRb collisions occur in the overlapping resonance regime? 3. Is it possible to extract the density of states of the intermediate complex from experimental measurements?

By studying magnetic Feshbach resonances in Rb + KRb collisions, we aim to address these three questions to gain deeper insight into the collision dynamics, which could be directly linked to the lifetime of the intermediate complex.

Experimentally, we probed magnetic Feshbach resonances between Rb and KRb over a magnetic field range of 0 to 542 G, using a variety of initial quantum states. In a typical sequence, we prepare an atom–molecule mixture similar to that used in the complex lifetime measurements. The magnetic field is ramped from 542 G down

to a target value x in 5 ms (though full stabilization typically requires up to 40 ms), and the mixture is held at that field for 50 ms. The field is then ramped back up over 70 ms for imaging. This ramp speed is limited by the voltage constraints of the Feshbach coil power supply, which caps the coil charging rate.

Since two-body inelastic loss is the dominant decay mechanism in this system, the Rb and KRb atom numbers are strongly correlated. To enhance the signal-to-noise ratio, we reverse-STIRAP the KRb molecules back to Rb atoms and image the total Rb number, representing the sum of both Rb and KRb.

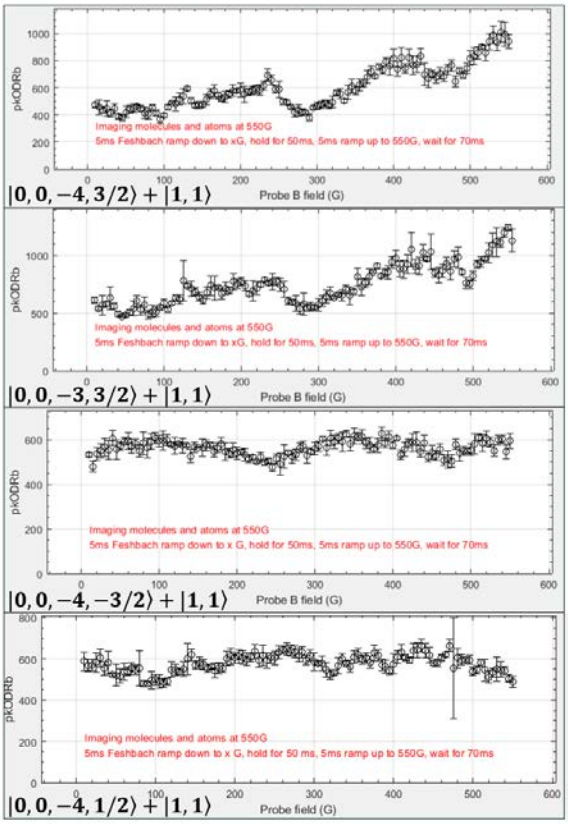

Figure 4.12: Magnetic field Feshbach resonance scans for various KRb + Rb state combinations (unpublished data). The KRb molecules are initially prepared in the $|0,0,-4,1/2\rangle$ state and subsequently transferred to the target state via two microwave π-pulses through the $N = 1$ manifold. Both atoms and molecules are imaged together using the reversed molecule association sequence, which converts KRb back into Rb atoms in the $|1,1\rangle$ state. Note that the state labels $|N, m_N, m_{I_\mathrm{K}}, m_{I_\mathrm{Rb}}\rangle$ are not strictly accurate below 20 G, where Zeeman interactions become weaker than the internuclear couplings in the molecular Hamiltonian. In such cases, the labels represent the initial molecular eigenstates before the magnetic field ramp.

In total, we explored four KRb nuclear spin states within the ground rotational manifold $N = 0$, as shown in Fig. 4.12. Unlike the KRb_2^* complex lifetime measurements, where all four configurations yield nearly identical lifetimes, the Feshbach resonance scans revealed both similarities and notable differences across these initial states.

The $|0, 0, -4, 3/2\rangle + |1, 1\rangle$ and $|0, 0, -3, 3/2\rangle + |1, 1\rangle$ configurations exhibit similar behavior: the two-body loss rates are significantly suppressed at high magnetic fields (above 400 G) compared to those at lower fields. Additionally, both cases demonstrated broad resonance features with widths on the order of 10–50 G, in contrast to the narrow Feshbach resonances typically observed in lighter systems. Interestingly, similar broad and shallow features are also observed in the $|0, 0, -4, -3/2\rangle + |1, 1\rangle$ and $|0, 0, -4, 1/2\rangle + |1, 1\rangle$ configurations. However, for these latter two state combinations, the overall two-body loss rates remain nearly constant across a wide range of magnetic fields and are close to the universal loss rate [98].

Although it would be interesting to explore the regime in which the Rb + KRb inelastic loss rate falls significantly below the universal limit (at magnetic fields above 400 G), such measurements are experimentally challenging. At these high fields, the Lorentz force acting on the charged ion products becomes substantial, deflecting them away from the MCP detector and preventing detection.

In addition to molecules in the ground rotational state, we also investigated magnetic Feshbach resonances involving the $N = 1$ state, $|1, 0, -4, 3/2\rangle + |1, 1\rangle$, as shown in Fig. 4.13.

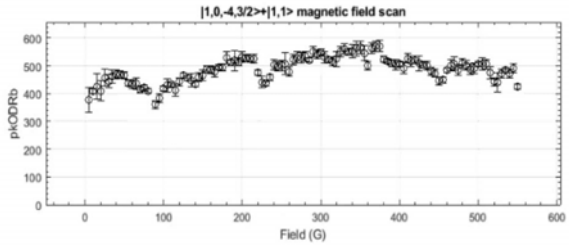

Figure 4.13: Magnetic field Feshbach resonance scans for $N = 1$ KRb + Rb (unpublished data). The KRb molecules are prepared in the $|1, 0, -4, 3/2\rangle$ state, the lowest hyperfine state in the $N = 1$ manifold.

In this scenario, the spectrum appears mostly flat. However, a few resonances with widths of approximately 10 G are observed at multiple magnetic field values, similar to the behavior seen in the $|0, 0, -4, -3/2\rangle + |1, 1\rangle$ and $|0, 0, -4, 1/2\rangle + |1, 1\rangle$ configurations.

Overall, the magnetic Feshbach resonance scans revealed two key features in Rb + KRb collisions: 1. the two-body loss rates for most state combinations are near the universal limit, with notable differences appearing only for a few configurations at high magnetic fields; and 2. the resonance features are broad, suggesting that the system lies in a strongly overlapping resonance regime [111, 112]. This observation is consistent with the conditions required for theoretical predictions of electric field dependence in complex lifetimes [93], which is still an active area of investigation.

4.8 Conclusion and Outlook

In this chapter, we have explored the dynamics of long-lived intermediate complexes formed during ultracold collisions between Rb atoms and KRb molecules. Our measurements reveal that the lifetimes of the KRb_2^* complex can reach hundreds of microseconds, exceeding predictions from statistical models, such as RRKM theory, by orders of magnitude. This discrepancy underscores the significance of quantum effects in ultracold collisions and motivates the development of theoretical frameworks that can accurately capture these observations.

By systematically varying the initial quantum states and external fields, we have shown that the complex lifetime is sensitive to the hyperfine state of the Rb atom and the applied electric and magnetic fields, while being relatively insensitive to the KRb nuclear spin state. In addition, our measurements of magnetic Feshbach resonances support the picture of a strongly overlapping resonance regime in the Rb + KRb collisions, where loss features are broad and exhibit near-universal inelastic loss rates in most cases. Altogether, our results provide valuable experimental benchmarks for ongoing theoretical efforts and underscore the need for a deeper understanding of intermediate complex dynamics in ultracold chemistry.

Chapter 5

Interference effects in chemical reactions

5.1 Quantum states of reactants and products

A key objective of our KRb experiment is to study chemical reactions with quantum state resolution. This involves characterizing the population of reaction products across all accessible quantum states, probing the phase relationships between them, and ultimately reconstructing the complete quantum state of both product molecules: potentially providing evidence for quantum entanglement. Achieving this goal requires first developing the ability to control and detect the quantum states of both reactants and products, followed by establishing a method to measure phase coherence between different states.

While we can prepare the reactants in well-controlled quantum states, detecting the quantum states of the reaction products is crucial to constructing a comprehensive picture of the reaction dynamics. Such measurements are particularly valuable for benchmarking theoretical models of chemical reaction processes. Moreover, gaining quantum-state sensitivity for the reaction products would enable coherent control of chemical reactions, where the quantum state of the reactants is tailored to steer the outcome toward a desired product state [113, 114, 115, 116].

Before beginning a detailed discussion in this chapter, we briefly introduce the relevant degrees of freedom of the reactants and products. Since the reactant atoms and molecules are prepared in their electronic ground states at ultracold temperatures, the relevant degrees of freedom include the vibrational and rotational states of the molecules, the orbital angular momentum between reaction products, and the electronic and nuclear spins. In this chapter, we focus on the chemical reaction $\mathrm{KRb} + \mathrm{KRb} \rightarrow \mathrm{K}_2(N = N_{\mathrm{K}_2}) + \mathrm{Rb}_2(N = N_{\mathrm{Rb}_2})$, which naturally occurs within the KRb cloud in our experiment.

In the KRb + KRb reaction, the exothermicity is 9.53 cm^{-1} [60]. As a result, the product molecules remain in their electronic singlet ground state, and both electronic and vibrational excitation of the products are energetically forbidden. On the other hand, the energy released is sufficient to populate excited rotational states. Meanwhile, the K_2 and Rb_2 products can also carry relative orbital angular momentum with respect to each other. Previous work has shown that nuclear spins tend not to play an active role in the chemical reaction [117, 35, 36]. Currently, we

lack a detection method with sufficient sensitivity to resolve the nuclear spin states of the products. Therefore, the relevant degrees of freedom in this reaction are the rotational states of K_2 and Rb_2 (N_{K_2}, N_{Rb_2}), and their relative orbital rotation L_{prod}.

5.2 Nuclear spin conservation in the KRb + KRb reaction

This experiment begins with KRb molecules prepared in a single hyperfine state via STIRAP [36]. By ramping the magnetic field from 542 G to an arbitrary value below 20 G, we can create an entangled KRb state. At low magnetic fields, the interaction between the two nuclei in KRb becomes comparable to the Zeeman interaction, leading to an entanglement between the K and Rb nuclear spins.

Experimentally, the KRb molecules start in a product state (in the nuclear spins basis of individual atoms) at 542 G: $|\psi_i\rangle = |N, m_N, m_{I_K}, m_{I_{Rb}}\rangle = |0, 0, -4, 1/2\rangle$, where N is the rotational quantum number, m_N is its projection along the magnetic field axis, and m_{I_K} ($m_{I_{Rb}}$) is the nuclear spin projection of K (Rb). We then ramp the magnetic field to a final value between 0 and 30 G within 10 ms. Throughout this ramp, the KRb molecules remain in an energy eigenstate and evolve into a superposition state: $|\psi_f\rangle = \alpha|0, 0, -4, 1/2\rangle + \beta|0, 0, -3, -1/2\rangle + \gamma|0, 0, -2, -3/2\rangle$, where the coefficients α, β, and γ can be calculated using the molecular Hamiltonian [36], as shown in Fig. 5.1.

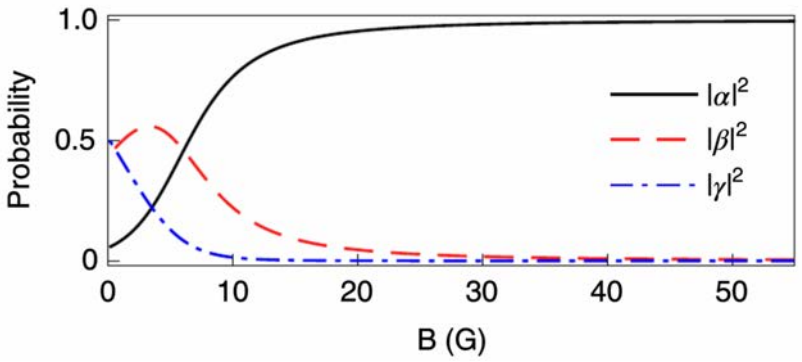

Figure 5.1: The state decomposition probabilities parameterized by α, β, γ as a function of external magnetic field [36].

At a magnetic field of 30 G, the KRb quantum state is predominantly $|-4, 1/2\rangle$. In this case, the Rb_2 products are primarily found in odd rotational states, as shown in Fig. 5.2, while the K_2 products are mainly in even rotational states. On the other hand, at 5 G, the KRb quantum state becomes $|\psi_f\rangle = 0.595|-4, 1/2\rangle + 0.719|-3, -1/2\rangle + 0.359|-2, -3/2\rangle$, which contains significant contributions from all three components. In this case, both the Rb_2 and K_2 products have a finite probability to populate both even and odd rotational states.

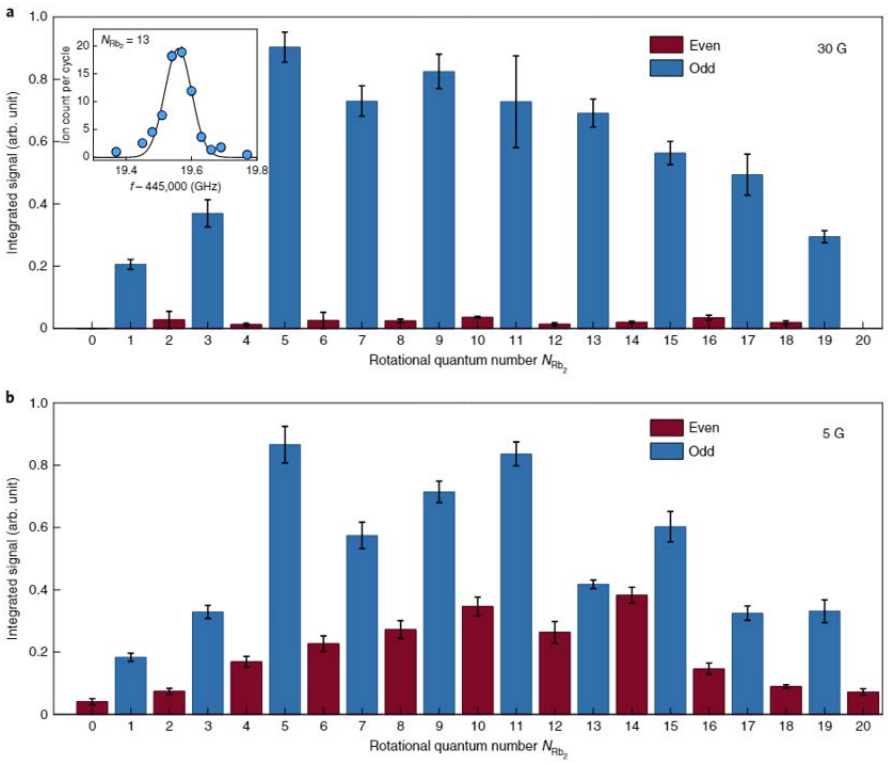

Figure 5.2: The rotational state distribution of the Rb_2 products [36]. (a) Rb_2 rotational state distribution at $B = 30$ G. (b) Rb_2 rotational state distribution at $B = 5$ G

Although this might seem difficult to interpret at first, it is consistent with the assumption that nuclear spins are not actively involved in the chemical reaction. To illustrate this, our group developed a simplified model to predict the nuclear spin state distribution of the reaction products [79]. In short, we assume that the nuclear spins are conserved throughout the reaction process, allowing us to treat the reaction simply as a basis transformation from the

reactant KRb nuclear spin basis to that of the K_2 and Rb_2 products. Without loss of generality, we assume the KRb molecules start in a superposition state: $|\psi_f\rangle = \alpha|-4,1/2\rangle + \beta|-3,-1/2\rangle + \gamma|-2,-3/2\rangle$, where the coefficients α, β, γ depend on the magnetic field as shown in Fig. 5.1. In a single KRb + KRb reaction event, the four-atom-system wavefunction can be written as: $|\psi_f\rangle \otimes |\psi_f\rangle =$ $\alpha^2|-4,1/2\rangle\otimes|-4,1/2\rangle+\beta^2|-3,-1/2\rangle\otimes|-3,-1/2\rangle+\gamma^2|-2,-3/2\rangle\otimes|-2,-3/2\rangle+$ $\alpha\beta(|-4,1/2\rangle\otimes|-3,-1/2\rangle+|-3,-1/2\rangle\otimes|-4,1/2\rangle)+\alpha\gamma(|-4,1/2\rangle\otimes|-2,-3/2\rangle+$ $|-2,-3/2\rangle\otimes|-4,1/2\rangle)+\beta\gamma(|-3,-1/2\rangle\otimes|-2,-3/2\rangle+|-2,-3/2\rangle\otimes|-3,-1/2\rangle)$

In the above notation, we use the basis $|m_{\mathrm{K1}}, m_{\mathrm{Rb1}}\rangle \otimes |m_{\mathrm{K2}}, m_{\mathrm{Rb2}}\rangle$ to represent the quantum state of the four atoms involved. For simplicity, we omit the explicit values of the nuclear spins, $I_{\mathrm{K}} = 4$ and $I_{\mathrm{Rb}} = 3/2$, to avoid redundancy. After the reaction, the two K atoms and two Rb atoms combine to form K_2 and Rb_2 molecules. We then transform to the coupled nuclear spin basis of the product molecules, written as $|I_{\mathrm{K_2}}, m_{\mathrm{K_2}}\rangle \otimes |I_{\mathrm{Rb_2}}, m_{\mathrm{Rb_2}}\rangle$. The result of this transformation is shown in the following equation [79]:

$$
\begin{aligned}
&\psi_{\mathrm{K_2,Rb_2}} \\
&= \alpha^2|8,-8\rangle \otimes \left(\sqrt{\frac{3}{5}}|3,1\rangle - \sqrt{\frac{2}{5}}|1,1\rangle\right) \\
&+ \beta^2\left(-\sqrt{\frac{7}{15}}|6,-6\rangle + \sqrt{\frac{8}{15}}|8,-6\rangle\right)\otimes \\
&\left(\sqrt{\frac{3}{5}}|3,-1\rangle - \sqrt{\frac{2}{5}}|1,-1\rangle\right)
\end{aligned}
$$

$$
\begin{aligned}
&+\gamma^2\left(\sqrt{\frac{45}{143}}|4,-4\rangle-\sqrt{\frac{14}{55}}|6,-4\rangle+\sqrt{\frac{28}{65}}|8,-4\rangle\right)\otimes\\
&|3,-3\rangle\\
&+\alpha\beta\left(-\sqrt{\frac{1}{2}}|7,-7\rangle+\sqrt{\frac{1}{2}}|8,-7\rangle\right)\otimes\\
&\left(-\frac{1}{2}|0,0\rangle-\frac{1}{2\sqrt{5}}|1,0\rangle+\frac{1}{2}|2,0\rangle+\frac{3}{2\sqrt{5}}|3,0\rangle\right)\\
&+\alpha\beta\left(\sqrt{\frac{1}{2}}|7,-7\rangle+\sqrt{\frac{1}{2}}|8,-7\rangle\right)\otimes\\
&\left(\frac{1}{2}|0,0\rangle-\frac{1}{2\sqrt{5}}|1,0\rangle-\frac{1}{2}|2,0\rangle+\frac{3}{2\sqrt{5}}|3,0\rangle\right)\\
&+\alpha\gamma\left(\frac{2}{\sqrt{15}}|6,-6\rangle-\sqrt{\frac{1}{2}}|7,-6\rangle+\sqrt{\frac{7}{30}}|8,-6\rangle\right)\otimes\\
&\left(\sqrt{\frac{3}{10}}|1,-1\rangle+\sqrt{\frac{1}{2}}|2,-1\rangle+\sqrt{\frac{1}{5}}|3,-1\rangle\right)\\
&+\alpha\gamma\left(\frac{2}{\sqrt{15}}|6,-6\rangle+\sqrt{\frac{1}{2}}|7,-6\rangle+\sqrt{\frac{7}{30}}|8,-6\rangle\right)\otimes\\
&\left(\sqrt{\frac{3}{10}}|1,-1\rangle-\sqrt{\frac{1}{2}}|2,-1\rangle+\sqrt{\frac{1}{5}}|3,-1\rangle\right)\\
&+\beta\gamma\left(\frac{3}{\sqrt{26}}|5,-5\rangle-\sqrt{\frac{1}{10}}|6,-5\rangle-\sqrt{\frac{2}{13}}|7,-5\rangle+\sqrt{\frac{2}{5}}|8,-5\rangle\right)\\
&\otimes\left(\sqrt{\frac{1}{2}}|2,-2\rangle+\sqrt{\frac{1}{2}}|3,-2\rangle\right)\\
&-\beta\gamma\left(\frac{3}{\sqrt{26}}|5,-5\rangle+\sqrt{\frac{1}{10}}|6,-5\rangle-\sqrt{\frac{2}{13}}|7,-5\rangle-\sqrt{\frac{2}{5}}|8,-5\rangle\right)\\
&\otimes\left(-\sqrt{\frac{1}{2}}|2,-2\rangle+\sqrt{\frac{1}{2}}|3,-2\rangle\right). \qquad (5.1)
\end{aligned}
$$

Since the product molecules are homonuclear, the symmetry of their nuclear spin states can be determined by evaluating $I_{\mathrm{K(Rb)}}+I_{\mathrm{K(Rb)}}-I_{\mathrm{K_2(Rb_2)}}$: the result

is symmetric if even and antisymmetric if odd. This symmetry constraint links the nuclear spin and rotational degrees of freedom of the products, allowing us to infer their nuclear spin parities by probing their rotational states. As a result, we can map the nuclear spin states onto the rotational state parities and extract the population distribution across the four parity combinations of the product molecules: $|N_{\mathrm{K}_2} = \text{even, odd}, N_{\mathrm{Rb}_2} = \text{even, odd}\rangle$ (abbreviated as $|e,e\rangle$), $|e,o\rangle$, $|o,e\rangle$, and $|o,o\rangle$:

$$\begin{aligned} P_{|o,e\rangle} &= |\alpha\beta|^2 + |\alpha\gamma|^2 + |\beta\gamma|^2 \\ P_{|e,o\rangle} &= 1 - P_{|o,e\rangle} \\ P_{|e,e\rangle} &= P_{|o,o\rangle} = 0 \end{aligned} \tag{5.2}$$

The result from this model agrees well with experimental measurements when we focus on a single product species, such as Rb_2, as shown in Fig. 5.2. At a magnetic field of 30 G, where $\alpha \sim 1$ and $\beta, \gamma \sim 0$, nearly all Rb_2 products end up in odd rotational states. In contrast, at a magnetic field of 5 G, α, β, and γ all become finite, and we begin to observe a noticeable population of Rb_2 products in even rotational states.

Although the validity of the model could be further supported by detecting the Rb_2 and K_2 products separately, the theoretical model also predicts an anti-correlation between the rotational state parity of the two product species. This anti-correlation, especially when combined with potential phase coherence between them, suggests that the product molecules may be quantum mechanically entangled.

Therefore, it becomes essential to perform coincidence detection (Chapter 3) to probe both product species originating from the same reaction event. This approach not only reveals correlations between the rotational and nuclear spin states but also naturally allows us to determine the probability of dissociation into all possible exit channels of the chemical reaction.

5.3 Product state distribution in KRb + KRb reactions

One of the main objectives of our experiment is to carry out a state-to-state study of the outcomes in the $\mathrm{KRb} + \mathrm{KRb} \rightarrow \mathrm{K_2} + \mathrm{Rb_2}$ reaction. Experimentally, this means preparing all reactants in a single quantum state and measuring the final population distribution of the products. Ideally, one would also probe the relative phases between product states, but this remains highly challenging (see outlook). Since the released energy can only excite the rotational states of the products, the exit channels are labeled by the rotational quantum numbers of $\mathrm{K_2}$ and $\mathrm{Rb_2}$: ($N_{\mathrm{K_2}}$, $N_{\mathrm{Rb_2}}$). Measuring the population in each of these exit channels requires the use of coincidence detection (Chapter 3). In 2020, our group conducted a detailed study to measure the product state distributions across all 57 energetically allowed exit channels [43] at a magnetic field of $B = 30$ G, with the results presented in Fig. 5.3.

Given the long lifetime of the $\mathrm{K_2Rb_2^*}$ intermediate complex measured in [84],

which agrees with predictions from RRKM theory, we expect the internal energy to fully redistribute among the available degrees of freedom, primarily vibration and rotation, within the tetra-atomic complex. As a result, the system is expected to behave statistically, meaning that all energetically allowed exit channels should be equally likely to be populated, with the probability of scattering into a particular (N_{K_2}, N_{Rb_2}) channel proportional to its degeneracy. Experimentally, we find that the populations in most channels follow this statistical model [43], although a few outliers exhibit clear deviations from statistical behavior.

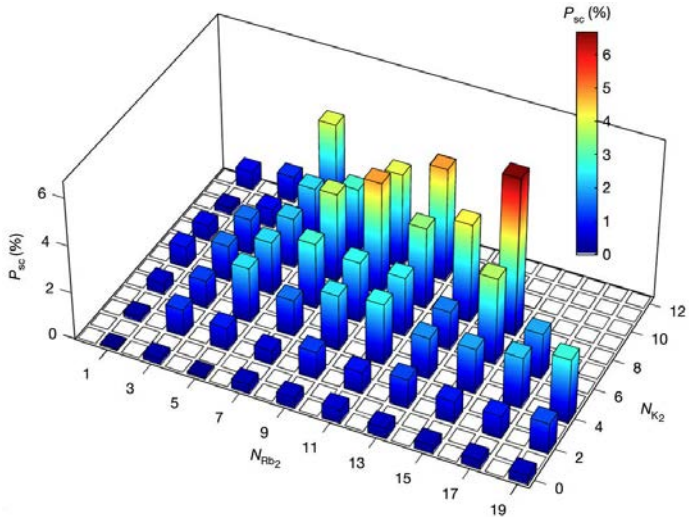

Figure 5.3: We measured the scattering probabilities into various exit channels of the KRb + KRb $\rightarrow$ K_2 + Rb_2 reaction [43]. These measurements were carried out at a magnetic field of $B = 30$ G, with the reactant KRb molecules prepared in the $|-4, 1/2\rangle$ hyperfine state. We focused on detecting even rotational states of K_2 and odd rotational states of Rb_2, as no significant signal was observed (and predicted) in other parity combinations.

Formally, the reactants and products must satisfy angular momentum conservation:

$$\boldsymbol{N}_{\mathrm{K_2}} + \boldsymbol{N}_{\mathrm{Rb_2}} + \boldsymbol{L}_{\mathrm{prod}} = \boldsymbol{J}_{\mathrm{tot}}.$$

Here, $\boldsymbol{L}_{\mathrm{prod}}$ is the relative orbital angular momentum between the two product molecules, and $\boldsymbol{J}_{\mathrm{tot}}$ is the total angular momentum, which remains conserved throughout the reaction. Since the KRb molecules collide via p-wave, we know that $J_{\mathrm{tot}} = 1$. The degeneracy of a given product channel is determined by counting all combinations of (N_{prod}, L_{prod}), where N_{prod} is the total angular momentum from adding $\boldsymbol{N}_{\mathrm{K_2}}$ and $\boldsymbol{N}_{\mathrm{Rb_2}}$. For each rotational state pair $(N_{\mathrm{K_2}}, N_{\mathrm{Rb_2}})$, we apply triangular inequalities to find the allowed values of N_{prod}. Then, for each N_{prod}, we find all possible L_{prod} that satisfy the constraint $\boldsymbol{N}_{\mathrm{prod}} + \boldsymbol{L}_{\mathrm{prod}} = \boldsymbol{J}_{\mathrm{tot}}$. Additionally, total parity must be conserved [106], requiring:

$$(-1)^{N_{\mathrm{K_2}}}(-1)^{N_{\mathrm{Rb_2}}}(-1)^{L_{\mathrm{prod}}} = -1.$$

As an example, for $(N_{\mathrm{K_2}}, N_{\mathrm{Rb_2}}) = (2, 3)$, the possible values of N_{prod} range from 1 to 5. Applying the angular momentum and parity constraints, we find 8 allowed product channels: $(N_{\mathrm{prod}}, L_{\mathrm{prod}}) = (1, 0)$, (1,2), (2,2), (3,2), (3,4), (4,4), (5,4), and (5,6). This same approach can be used to compute the degeneracy of any exit channel.

5.4 Interference effects

The works and methodologies described in the previous two sections were pioneered by the first generation of graduate student and postdoc, Yu Liu and Ming-Guang Hu. Their efforts laid the foundation for our understanding of how reaction products are distributed among different quantum states. Building on this knowledge, and with the ultimate goal of probing entanglement between the products, our next step is to investigate the phase relationships between different product quantum states.

Among the various degrees of freedom available, we begin by probing phase coherence in the nuclear spin subspace. This choice is motivated by prior evidence indicating that nuclear spins remain conserved throughout the reaction, making them a promising candidate for exhibiting coherence. In addition, we can reasonably propose a hypothesis where the chemical reaction itself redistributes the entanglement between the reactant nuclei to the two product molecules, as shown in Fig. 5.4. This hypothesis, although theoretically plausible, is non-trivial to prove experimentally. To move closer to such a goal, we present the observation of quantum interference effects that reveal quantum coherence in the nuclear spin degree of freedom, which is an essential prerequisite for establishing entanglement between the product molecules.

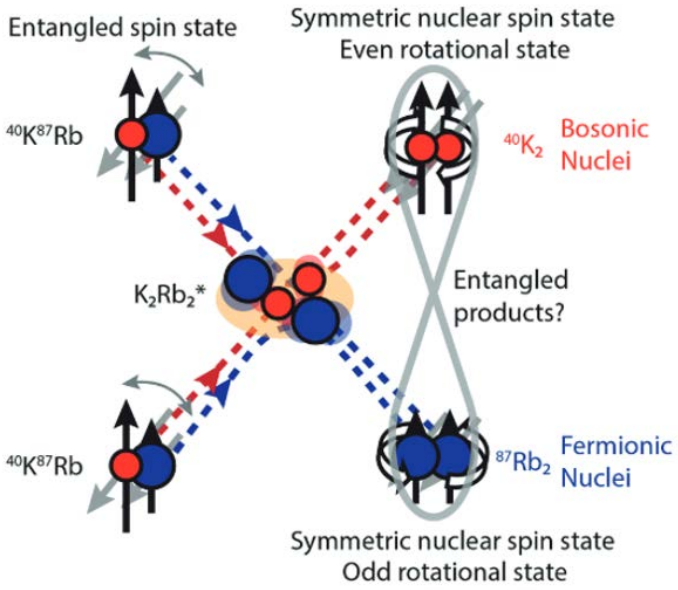

Figure 5.4: A demonstration of entanglement distribution in the KRb + KRb reaction process: When the nuclear spins of K and Rb atoms begin in an entangled state, the chemical reactions could redistribute such entanglement between product molecules.

5.4.1 Destructive interference for reactants in a superposition state

If we return to the mathematical description of the model that assumes nuclear spins are conserved throughout the reaction, as described in Eq. 5.1, an interesting feature emerges: the absence of the $|e, e\rangle$ and $|o, o\rangle$ channels is actually the result of destructive interference. This interference arises from two terms with equal

magnitude but opposite sign in the Clebsch–Gordan coefficients. The cancellation of these terms is visualized in Fig. 5.5. The mathematical origin of this effect can be found by carefully examining Eq. 5.1, where the terms corresponding to (even, even) and (odd, odd) nuclear spin states cancel exactly due to their opposite signs.

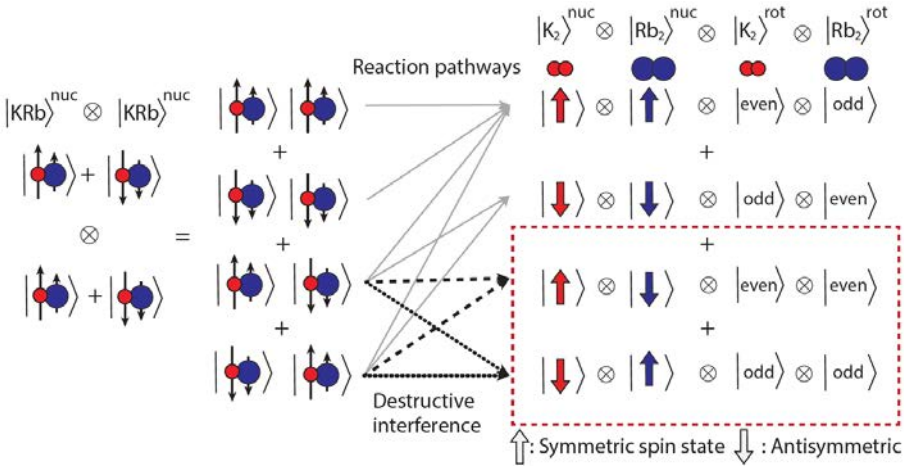

Figure 5.5: A demonstration of the destructive interference that cancels out the $|e, e\rangle$ and $|o, o\rangle$ product channels [79]. Blue and red spheres represent Rb and K atoms, respectively, and the up/down arrows indicate different nuclear spin projections. This example illustrates the case of a superposition of two nuclear spin states, where interference between terms leads to cancellation.

Experimentally, we test this by performing coincidence detection on the reaction products at a magnetic field of $B = 5$ G, where the KRb molecules are in a superposition state in the $|\mathrm{m_K}, \mathrm{m_{Rb}}\rangle$ basis. Instead of measuring all ∼200 energetically allowed exit channels across the full range of $(N_{\mathrm{K_2}}, N_{\mathrm{Rb_2}})$ pairs, we focus on a smaller subset consisting of four exit channels: $(N_{\mathrm{K_2}} = 9, 10; N_{\mathrm{Rb_2}} = 9, 10)$,

which is sufficient to probe the parity of the products. These states are selected for two main reasons: 1. they have relatively large degeneracies, and 2. the products in these channels store most of their energy in the rotational degrees of freedom, resulting in low kinetic energies that are ideal for efficient ionization detection. Additional details about these four states can be found in Tab. 5.1.

Description	$\|10,9\rangle$	$\|10,10\rangle$	$\|9,10\rangle$	$\|9,9\rangle$
velocities (v_{K_2}, v_{Rb_2}) (m/s)	(19.1,8.8)	(16.6,7.6)	(22.3,10.3)	(24.3,11.2)
Detection efficiency C	0.2757(9)	0.3447(6)	0.2055(6)	0.1741(8)
Degeneracy D	29	31	29	28
Calibration factor c	0.2709(8)	0.3621(6)	0.2019(6)	0.1651(8)

Table 5.1: Relevant information of the four product channels of choice [79]. The calibration factors are proportional to the theoretically calculated overall detection efficiencies, taking into account the degeneracy of each channel and the product velocity.

The coincidence detection result is shown in Fig. 5.6, where we observe prominent signals in the (10,9) and (9,10) channels. In contrast, the signal levels in the (10,10) and (9,9) channels are comparable to the background. To extract the actual distribution across the four parity channels ($|e,e\rangle$, $|o,o\rangle$, $|e,o\rangle$, and $|o,e\rangle$), we normalize the raw ion counts by accounting for the detection efficiencies of each channel, as summarized in Tab. 5.1.

The ionization efficiency used for normalization is deliberate and nontrivial. Two major sources of detection bias are the velocity-dependent detection efficiency, denoted by C, and the product state degeneracy, denoted by D. The expected number of coincidence ion counts for a given product state $|i, j\rangle$ is proportional to $P_{ij}C_{ij}D_{ij}$, where P_{ij} is the distribution in each parity channel (a.k.a. branching ratio) that we aim to extract and compare with theoretical predictions as shown in Eq. 5.1.

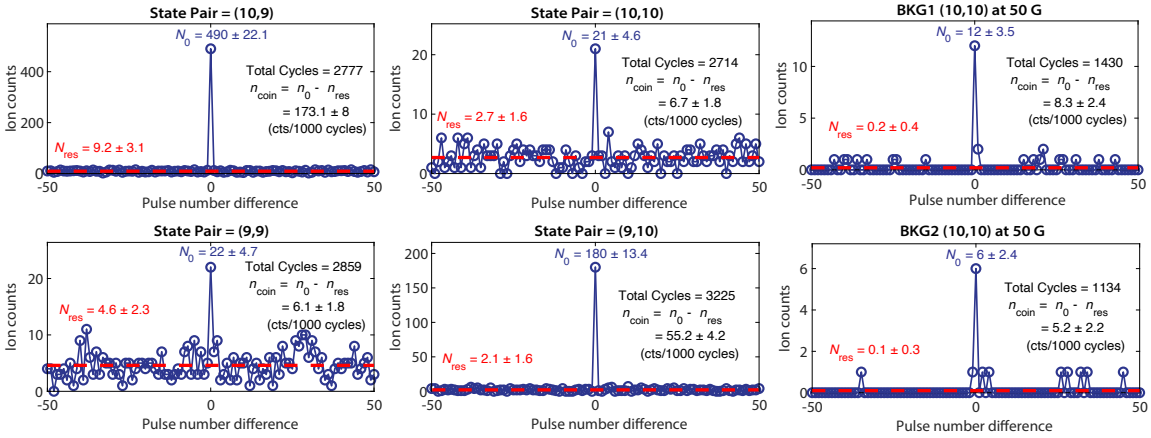

Figure 5.6: Coherent reaction data taken at 5 G, along with background measurements at 50 G [79]. The number of K_2-Rb_2 ion pairs passing both momentum and time-of-flight filtering is plotted as a function of the pulse number difference. The background ion signal measured at 50 G, where the KRb state is nearly pure $|-4, 1/2\rangle$, serves as a reference for coincidence counts arising from off-resonant ionization and other background processes.

The dependence of the detection efficiency on product velocity arises from two

major effects: 1. faster products are more likely to exit the detection region covered by the REMPI beams before the ionization pulses are applied, and 2. products with higher velocity along the propagation direction of the REMPI beams experience larger Doppler shifts in the bound-to-bound transition, which reduces the probability of being promoted to the excited state. To account for these effects, we perform a Monte Carlo simulation to calculate the normalization factors that incorporate both contributions to the detection efficiency.

In the simulation, we sample 10^5 K_2-Rb_2 pairs in each state and compute the total coincidence counts for each exit channel. The magnitudes of the product velocities are calculated using energy conservation, the previously reported total exothermicity of 9.77 cm^{-1} [60], and the rotational constants of $^{40}K_2$ and $^{87}Rb_2$ [43]. The total kinetic energies of the product pairs for the four relevant rotational state combinations are:

- $E(N_{K_2} = 9, N_{Rb_2} = 9) = 2.871$ cm^{-1}
- $E(N_{K_2} = 10, N_{Rb_2} = 9) = 1.776$ cm^{-1}
- $E(N_{K_2} = 9, N_{Rb_2} = 10) = 2.434$ cm^{-1}
- $E(N_{K_2} = 10, N_{Rb_2} = 10) = 1.338$ cm^{-1}

The corresponding product pair velocities are listed in Table 5.1. For each K_2-Rb_2 pair, the velocity direction of K_2 is sampled from a uniform spherical distribution, and Rb_2 is assigned a velocity in the opposite direction to conserve momentum.

The creation time of each product pair is uniformly sampled between $t = 0$ and $t = 45$ μs to represent the random timing of individual reaction events. All products are initialized at the same starting location, which is set to the center of the REMPI beams. We then track the position of each product molecule at $t = 45$ μs, corresponding to the moment when the REMPI beams are turned on.

We model the resonant excitation in REMPI using a two-level system with decay from the excited state [43] representing spontaneous emission. The dynamics of the ground state $|0\rangle$ in the $X^1\Sigma$ manifold and the intermediate state $|1\rangle$ in the $B^1\Pi$ state are described by the following rate equations:

$$\begin{aligned}
\frac{d}{dt}\rho_{00} &= -\frac{i}{2}(\Omega_{01}\rho_{10} - \text{c.c.}), \\
\frac{d}{dt}\rho_{11} &= -\Gamma\rho_{11} + \frac{i}{2}(\Omega_{01}\rho_{10} - \text{c.c.}), \\
\frac{d}{dt}\rho_{10} &= -\frac{1}{2}\Gamma\rho_{10} + i\Delta\rho_{10} + \frac{i}{2}\Omega_{01}(\rho_{11} - \rho_{00}),
\end{aligned} \tag{5.3}$$

where c.c. denotes the complex conjugate, and Ω_{01} is the Rabi frequency of the bound-to-bound transition. The detuning Δ arises from the Doppler shift for each molecule, to the 648 nm (for K_2) or 674 nm (for Rb_2) transition. The decay rate Γ of the excited state $|1\rangle$ is taken as $2\pi \times 14$ MHz for both K_2 and Rb_2 [43].

The Rabi frequency Ω_{01} is position-dependent, with a peak value of $2\pi \times 15$ MHz and a Gaussian spatial profile characterized by a $1/e^2$ beam waist of 750 μm, as measured from the experiment. We assume the same Rabi frequency for all initial rotational states, as they are all Q-branch transitions. In the experiment, we apply a disk-shaped dark mask to shield the reactants from the REMPI beams. The inner

dark region has a radius of 125 μm, and the beam is truncated at a 1 mm radius by the outer dimension of the mask. These geometric constraints are also incorporated into the simulation, where we ignore product molecules outside the beam.

We calculate the excited state populations ρ_{11,K_2} and ρ_{11,Rb_2} 20 ns after the 648 nm or 674 nm beam turns on, corresponding to the firing time of the 532 nm laser pulse. In the simulation, we assume that the ionization rate from the 532 nm pulse is constant in all cases, so the final K_2 (Rb_2) ion signal is proportional to the population term in the density matrix: ρ_{11,K_2} (ρ_{11,Rb_2}). We then sum up the product of excited state populations, $\rho_{11,K_2}\rho_{11,Rb_2}$ over all ionization events, which represents the simulated coincidence counts for each state pair. The overall detection efficiencies for all four relevant state pairs are reported in Tab. 5.1.

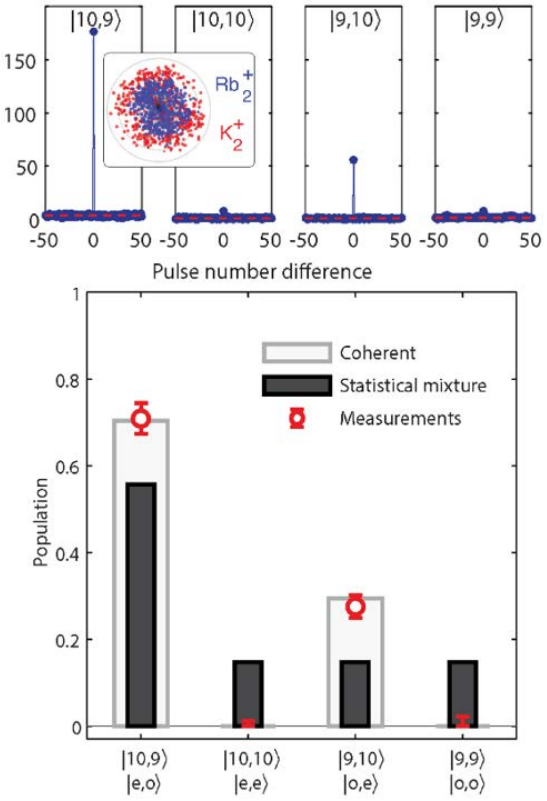

Figure 5.7: Conversion of the raw coincidence counts to measured branching ratios [79]. Theoretical predictions are presented for two scenarios: one in which nuclear spin coherence is preserved throughout the chemical reaction, and another in which coherence is completely lost.

With the normalization factors, we convert the raw coincidence counts into branching ratios for the four rotational parity channels, as shown in Fig. 5.7. If the nuclear spin wavefunction remains pure and coherent throughout the reaction, meaning the basis transformation described in Eq. 5.1 holds, the resulting population distribution is given by the gray bars. In contrast, if the nuclear spin coherence is

lost and the wavefunction fully dephases, the expected distribution corresponds to the black solid bars, which are calculated by summing the probabilities (rather than amplitudes) for each parity channel. The measured results match those of the fully coherent case, indicating that nuclear spin coherence is preserved during the reaction process. Quantitatively, we found the coherence parameter Γ is no lower than 0.9014 (with 95% confidence), where Γ is defined as the branching ratio for the reaction to proceed coherently.

5.4.2 Beyond energy eigenstates

In the previous section, we restricted our analysis to the reaction outcomes following a magnetic field ramp to 5 G, where the nuclear spin state of the reactants becomes $|\psi_f\rangle = \alpha|-4, 1/2\rangle + \beta|-3, -1/2\rangle + \gamma|-2, -3/2\rangle$. Although this state is a superposition in the uncoupled nuclear spin basis, it remains an energy eigenstate. One can attempt to interpret the observed destructive interference from a symmetry-based perspective: since both KRb molecules are prepared in the same quantum state, the two K atoms and the two Rb atoms are symmetric under particle exchange, and this symmetry must be preserved during the reaction. As a result, the two product molecules must also share the same overall symmetry to maintain the symmetry of the full wavefunction. Therefore, only the $|e, o\rangle$ and $|o, e\rangle$ channels satisfy the symmetry constraints. This symmetry-based argument is consistent with our experimental observations. However, it cannot produce quantitative predictions on its own, such as the branching ratios between the channels. Our theoretical

model, based on nuclear spin basis transformation, is necessary to provide the numerical values that match the measured outcomes.

To further test the validity of the theory, we extend our investigation to cases where the reactant quantum states are no longer energy eigenstates. This is achieved by using a two-photon microwave transfer scheme to prepare the molecules in an equal superposition of two hyperfine states within the ground rotational manifold. Due to limitations in our microwave control and the initial STIRAP state of $|m_{\mathrm{K}} = -4, m_{\mathrm{Rb}} = 1/2\rangle$, we select a few target ground states to form superpositions with: $|m_{\mathrm{K}} = -3, m_{\mathrm{Rb}} = -1/2\rangle$, $|m_{\mathrm{K}} = -3, m_{\mathrm{Rb}} = 3/2\rangle$, and $|m_{\mathrm{K}} = -4, m_{\mathrm{Rb}} = -3/2\rangle$.

The general scheme for our microwave-based state preparation is illustrated in Fig. 5.8. It involves selecting an appropriate intermediate state in the $N = 1$ manifold that couples efficiently to both hyperfine states. The microwave sequence consists of three steps: first, a π-pulse transfers the initial state to the intermediate rotational excited state; second, a $\pi/2$-pulse creates an equal superposition between the intermediate state and the target state; and finally, a π-pulse transfers the intermediate component back to the initial state.

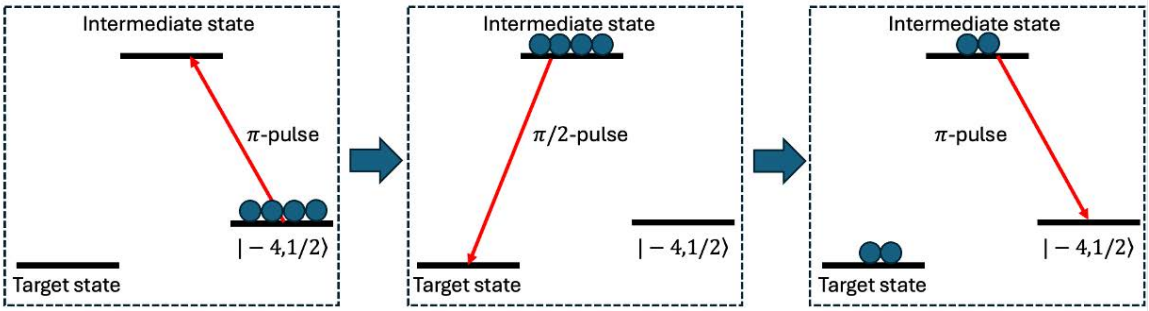

Figure 5.8: The microwave state preparation scheme to prepare reactant molecules in an equal superposition of two hyperfine states in the ground rotational manifold.

The experimental procedure typically proceeds as follows. We begin by using the Diatomix package [67] to identify suitable intermediate states in the $N = 1$ manifold that exhibit strong electric dipolar couplings to both hyperfine states. At the same time, we exclude intermediate states with nearby strong transitions, as those could degrade the fidelity of the microwave transfer sequence.

Once a candidate intermediate state is chosen, we perform spectroscopy to precisely determine the transition frequency for the first leg of the microwave transfer, resolving it to the kilohertz level. We then fix the microwave frequency at this value and measure Rabi oscillations by varying the pulse duration, which allows us to determine the π-pulse time. The same procedure is repeated for the second leg of the transfer.

To verify coherence between the two hyperfine states, we perform a Ramsey

measurement by inserting a variable wait time t between two preparation sequences (π–$\pi/2$–π). If coherence is preserved, we expect to observe oscillations in the initial state population as a function of t.

Case 1: $|m_{\mathrm{K}} = -4, m_{\mathrm{Rb}} = 1/2\rangle + |m_{\mathrm{K}} = -3, m_{\mathrm{Rb}} = -1/2\rangle$

We first explore the reaction outcomes by preparing the reactants in a superposition state of $\frac{1}{\sqrt{2}}(|m_{\mathrm{K}} = -4, m_{\mathrm{Rb}} = 1/2\rangle + |m_{\mathrm{K}} = -3, m_{\mathrm{Rb}} = -1/2\rangle)$. We find that the results closely resemble the predictions for a fully coherent reaction, with minimal population observed in the $|e, e\rangle$ and $|o, o\rangle$ channels. This suggests that coherence is largely preserved throughout the chemical process.

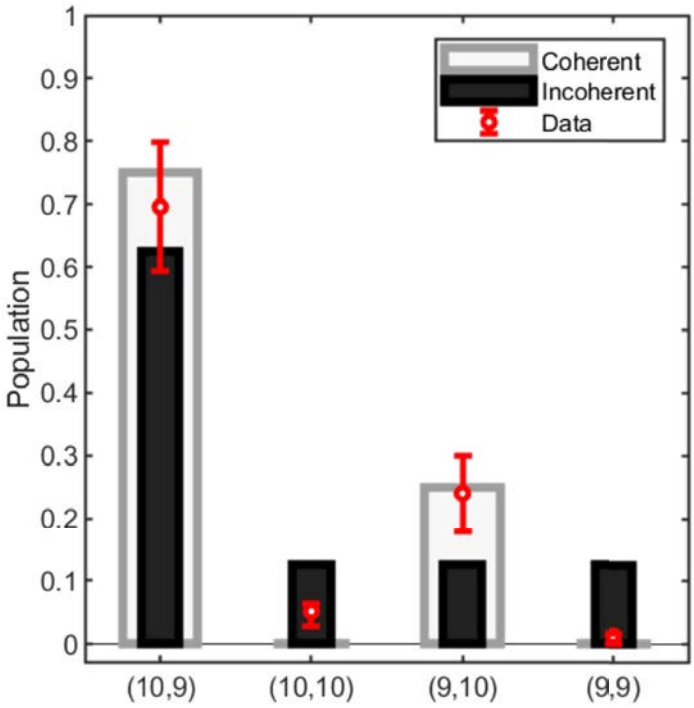

Figure 5.9: Branching ratios of the four parity channels with reactants prepared in $\frac{1}{\sqrt{2}}(|m_{\mathrm{K}} = -4, m_{\mathrm{Rb}} = 1/2\rangle + |m_{\mathrm{K}} = -3, m_{\mathrm{Rb}} = -1/2\rangle)$ (unpublished data). Theoretical predictions are presented for two scenarios: one in which nuclear spin coherence is preserved throughout the chemical reaction, and another in which coherence is completely lost. This measurement is taken at a magnetic field of 30 G.

Separately, we verified the coherence between the two hyperfine states used in the initial state preparation via the Ramsey sequence described earlier, as shown in Fig. 5.10. We observed clear oscillations for wait times shorter than 150 ms, consistent with expectations for a Ramsey measurement. At longer wait times, the oscillations become washed out. We attribute this to shot-to-shot magnetic field

fluctuations in our system, which introduce a random distribution of oscillation frequencies. Over longer timescales, these variations lead to dephasing across experimental shots, resulting in the averaged signal losing contrast.

Importantly, we do not interpret this decay in contrast as evidence of decoherence between the two hyperfine states. If the superposition had decohered, the molecules would become distinguishable, and we would expect faster losses due to s-wave collisions. Instead, the overall slow decay of the molecule number ($\sim$ 300 ms) is consistent with p-wave-dominated loss, similar to what is observed for molecules in the STIRAP state. There are two possibilities for the contrast decay: the shot-to-shot variation of the DC magnetic field, and the existence of a mysterious magnetic field gradient in our system as large as 7.7 mG/cm per Gauss of magnetic field generated by the Feshbach coils.

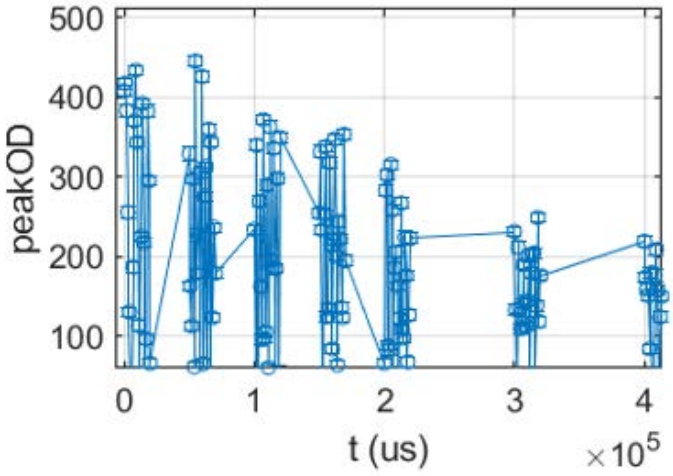

Figure 5.10: Ramsey measurement probing the coherence between the hyperfine states $|m_{\mathrm{K}} = -4, m_{\mathrm{Rb}} = 1/2\rangle$ and $|m_{\mathrm{K}} = -3, m_{\mathrm{Rb}} = -1/2\rangle$ (unpublished data). The y-axis shows the population of molecules remaining in the initial hyperfine state as a function of the wait time between the two halves of the Ramsey pulses.

Case 2: $|m_{\mathrm{K}} = -4, m_{\mathrm{Rb}} = 1/2\rangle + |m_{\mathrm{K}} = -3, m_{\mathrm{Rb}} = 3/2\rangle$

Similarly, we probe the reaction outcomes by preparing the reactants in a superposition state of $\frac{1}{\sqrt{2}}(|m_{\mathrm{K}} = -4, m_{\mathrm{Rb}} = 1/2\rangle + |m_{\mathrm{K}} = -3, m_{\mathrm{Rb}} = 3/2\rangle)$, as shown in Fig. 5.11. In this case, the results deviate from the predictions of a fully coherent reaction, with significant population observed in the $|e, e\rangle$ and $|o, o\rangle$ channels. This suggests that coherence may not be preserved throughout the chemical process. Furthermore, the population in the $|e, e\rangle$ channel is unexpectedly high, exceeding the maximum possible value predicted even under full decoherence.

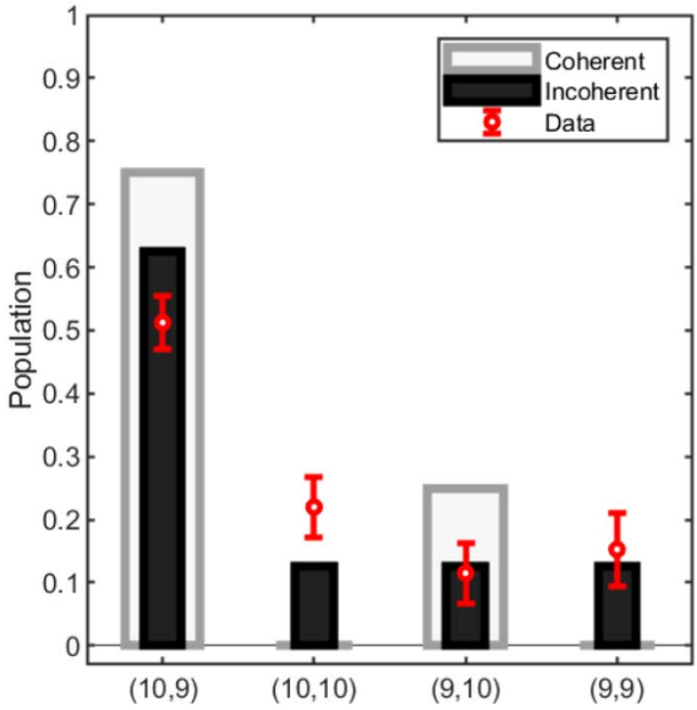

Figure 5.11: Branching ratios of the four parity channels with reactants prepared in $\frac{1}{\sqrt{2}}(|m_{\mathrm{K}} = -4, m_{\mathrm{Rb}} = 1/2\rangle + |m_{\mathrm{K}} = -3, m_{\mathrm{Rb}} = 3/2\rangle)$ (unpublished data). This measurement is taken at a magnetic field of 50 G.

Similar to the previous case, we verified the presence of Ramsey oscillations for this superposition state. For simplicity, we do not discuss the details here.

Case 3: $|m_{\mathrm{K}} = -4, m_{\mathrm{Rb}} = 1/2\rangle + |m_{\mathrm{K}} = -4, m_{\mathrm{Rb}} = -3/2\rangle$

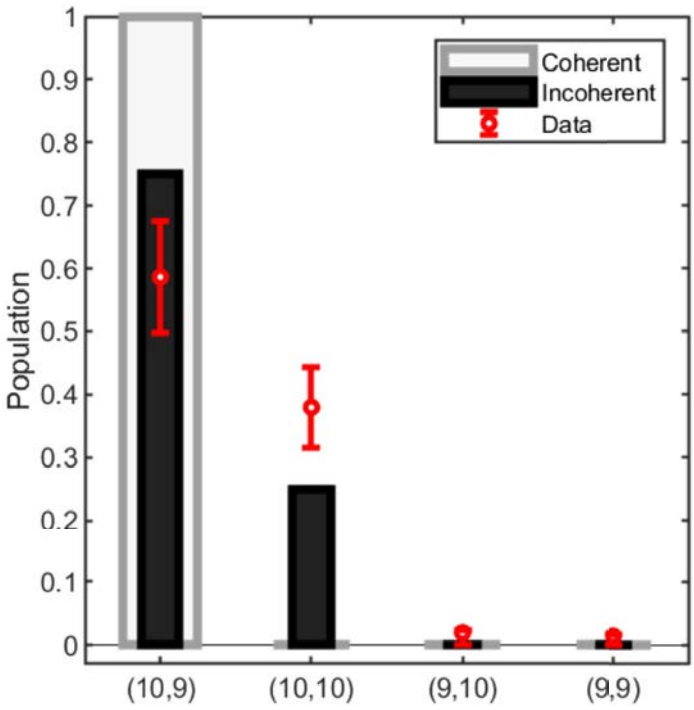

Figure 5.12: Branching ratios of the four parity channels with reactants prepared in $\frac{1}{\sqrt{2}}(|m_{\mathrm{K}} = -4, m_{\mathrm{Rb}} = 1/2\rangle + |m_{\mathrm{K}} = -4, m_{\mathrm{Rb}} = -3/2\rangle)$ (unpublished data). This measurement is taken at a magnetic field of 30 G.

Lastly, we probe the reaction outcomes by preparing the reactants in a superposition state of $\frac{1}{\sqrt{2}}(|m_{\mathrm{K}} = -4, m_{\mathrm{Rb}} = 1/2\rangle + |m_{\mathrm{K}} = -4, m_{\mathrm{Rb}} = -3/2\rangle)$, as shown in Fig. 5.12. In this case, the results deviate significantly from the predictions of a fully coherent reaction, with significant population observed in the $|e, e\rangle$ channel. Similar to case 2, the population in the $|e, e\rangle$ channel is also unexpectedly high, which cannot be explained by full decoherence.

Summary of all cases and speculation

Based on the evidence presented for all four cases (the eigenstate and the three superposition states), we find that the reaction outcomes align with predictions for a coherent process in some instances, but not in others. Interestingly, in the two cases where coherence appears to be preserved, the two hyperfine states involved share the same total magnetic quantum number m_{total}. This suggests a possible explanation: the system may maintain coherence within a single m_{total} manifold, while coherence between different m_{total} manifolds may be lost.

However, this hypothesis alone cannot explain the unexpectedly high population observed in the $|e, e\rangle$ channel, which exceeds even the fully incoherent prediction. This discrepancy raises questions about the general validity of the nuclear spin conservation assumption, particularly for reactants prepared in superposition states. It also opens the possibility that the reaction process itself may imprint an additional phase onto different quantum pathways, leading to constructive interference in certain channels (such as $|e, e\rangle$) and enhancing their population beyond the expected limit.

5.4.3 Magnetic field dependence of $|m_{\mathrm{K}} = -4, m_{\mathrm{Rb}} = 1/2\rangle$ + $|m_{\mathrm{K}} = -4, m_{\mathrm{Rb}} = -3/2\rangle$

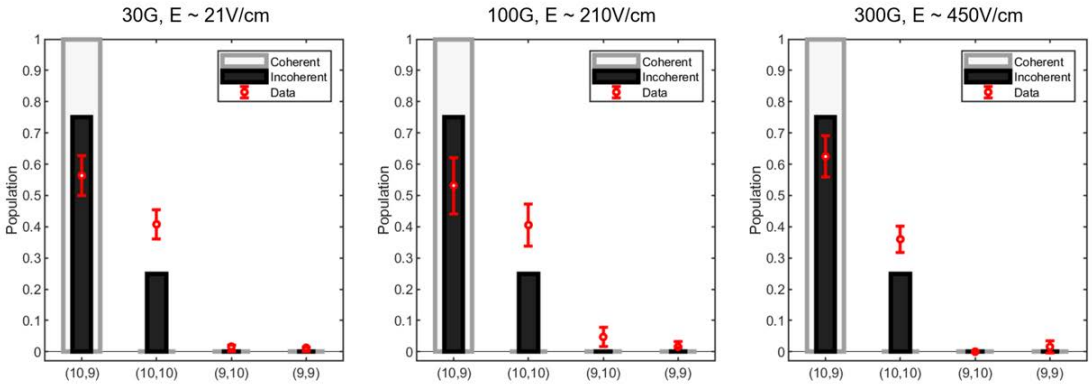

Figure 5.13: Branching ratios of the four parity channels with reactants prepared in the superposition state $\frac{1}{\sqrt{2}}\left(|m_{\mathrm{K}} = -4, m_{\mathrm{Rb}} = 1/2\rangle + |m_{\mathrm{K}} = -4, m_{\mathrm{Rb}} = -3/2\rangle\right)$ at magnetic fields of 30, 100, and 300 G (unpublished data). To capture the reaction products at higher magnetic fields, we increase the acceleration voltages on the repeller electrode, thus enhancing the electric field in the system. We note that this increased field should not affect the hyperfine states of the rotational ground state, as they are relatively insensitive to electric fields below the kV/cm level.

Here, we explore whether the magnetic field has an effect on the product branching ratios. Initially, we hypothesized that the excess population observed in the $|e, e\rangle$ channel might result from nuclear spin-changing reactions, particularly in cases

where the initial KRb quantum state is not an energy eigenstate. To test this, we increased the magnetic field, reasoning that at higher fields, the larger Zeeman splitting of the nuclear spin states could suppress any potential spin-changing dynamics. Under this hypothesis, nuclear spin conservation would be more robust at higher magnetic fields.

We performed measurements at magnetic fields of 30, 100, and 300 G. As shown in Fig. 5.13, we observe little to no variation in the branching ratios across this range. This suggests that nuclear spins may not actively participate in the reaction or that the critical magnetic field required to suppress nuclear spin-changing dynamics lies beyond our current experimental capabilities.

While we cannot draw a definitive conclusion from this study, we present these results as a reference for future investigations exploring the role of nuclear spins in ultracold chemical reactions.

5.4.4 Probing the role of phases and coherence: Reaction interferometer

While the results of the three cases beyond energy eigenstates remain puzzling and await a theoretical explanation, we can still test whether coherence is preserved in these reactions by manually introducing a phase between the reactants and observing whether the reaction outcomes depend on this phase. If coherence is indeed maintained throughout the chemical reaction in more general settings, such

a dependence would serve as a demonstration of coherent control of a bimolecular reaction, which has not yet been experimentally realized. We illustrate this idea schematically in Fig. 5.14.

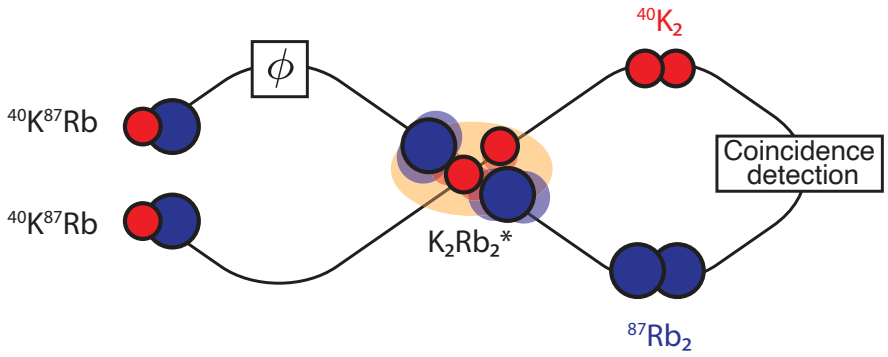

Figure 5.14: The conceptual picture of a reaction interferometer [118]. Two reactant KRb molecules are initialized in the same coherent superposition state $\frac{1}{\sqrt{2}}(|0\rangle + |1\rangle)$. Before the reaction, one molecule acquires a controllable phase ϕ (from microwaves), resulting in the state $\frac{1}{\sqrt{2}}(|0\rangle + e^{i\phi}|1\rangle)$. Here, one can arbitrarily choose state $|0\rangle$ and $|1\rangle$ (two nuclear spin states in our case). The resulting interference patterns can be measured in the branching ratios of the product states. These patterns provide a tool to quantify coherence in the reactants and offer a pathway to coherently control the formation of products across all reaction channels.

We follow the theoretical framework illustrated in Eq. 5.1, with an additional phase ϕ applied to one of the reactant molecules (the method for introducing this phase will be discussed later). For simplicity and without loss of generality, we define $|0\rangle = |-4, 1/2\rangle$ and $|1\rangle = |-3, -1/2\rangle$ for this discussion. With this, the initial

two-particle reactant state can be written as:

$$\psi_{\mathrm{KRb}} \otimes \psi_{\mathrm{KRb}} = \frac{1}{\sqrt{2}}(|-4, \frac{1}{2}\rangle + |-3, -\frac{1}{2}\rangle) \otimes \frac{1}{\sqrt{2}}(|-4, \frac{1}{2}\rangle + e^{i\phi}|-3, -\frac{1}{2}\rangle). \quad (5.4)$$

After transforming to the basis of the product molecules, the overall nuclear spin wavefunction becomes [118]:

$$\begin{aligned}
\psi^{\mathrm{nuc}}_{\mathrm{K_2,Rb_2}} = & \frac{1}{2}|8,-8\rangle \otimes (-\sqrt{\frac{2}{5}}|1,1\rangle + \sqrt{\frac{3}{5}}|3,1\rangle) \\
& + \frac{1}{2}e^{i\phi}(-\frac{1}{\sqrt{2}}|7,-7\rangle + \frac{1}{\sqrt{2}}|8,-7\rangle) \otimes (-\frac{1}{2}|0,0\rangle \\
& \quad - \frac{1}{2\sqrt{5}}|1,0\rangle + \frac{1}{2}|2,0\rangle + \frac{3}{2\sqrt{5}}|3,0\rangle) \\
& + \frac{1}{2}(\frac{1}{\sqrt{2}}|7,-7\rangle + \frac{1}{\sqrt{2}}|8,-7\rangle) \otimes (\frac{1}{2}|0,0\rangle \\
& \quad - \frac{1}{2\sqrt{5}}|1,0\rangle - \frac{1}{2}|2,0\rangle + \frac{3}{2\sqrt{5}}|3,0\rangle) \\
& + \frac{1}{2}e^{i\phi}(-\sqrt{\frac{7}{15}}|6,-6\rangle + 2\sqrt{\frac{2}{15}}|8,-6\rangle) \otimes (-\sqrt{\frac{2}{5}}|1,-1\rangle + \sqrt{\frac{3}{5}}|3,-1\rangle). \quad (5.5)
\end{aligned}$$

The total wavefunction of the system includes both the rotational and nuclear spin components. Due to the symmetry constraints for the homonuclear molecules, it can be written in the form:

$$\psi^{\mathrm{tot}}_{\mathrm{K_2,Rb_2}} = |SS\rangle|e,o\rangle + |AA\rangle|o,e\rangle + |SA\rangle|e,e\rangle + |AS\rangle|o,o\rangle \quad (5.6)$$

Here, S and A denote the symmetric and antisymmetric combinations of nuclear spin states, while e and o represent even and odd rotational states. By decomposing the terms in Eq. 5.5 into their corresponding nuclear spin symmetry components, we obtain:

$$\begin{aligned}
|SS\rangle &= -\frac{1}{2}\sqrt{\frac{2}{5}}|8,-8\rangle \otimes |1,1\rangle + \frac{1}{2}\sqrt{\frac{3}{5}}|8,-8\rangle \otimes |3,1\rangle \\
&\quad - \frac{1}{4\sqrt{10}}(1+e^{i\phi})|8,-7\rangle \otimes |1,0\rangle + \frac{3}{4\sqrt{10}}(1+e^{i\phi})|8,-7\rangle \otimes |3,0\rangle \\
&\quad + \frac{\sqrt{14}}{10\sqrt{3}}e^{i\phi}|6,-6\rangle \otimes |1,-1\rangle - \frac{\sqrt{7}}{10}e^{i\phi}|6,-6\rangle \otimes |3,-1\rangle \\
&\quad - \frac{2}{5\sqrt{3}}e^{i\phi}|8,-6\rangle \otimes |1,-1\rangle + \frac{\sqrt{2}}{5}e^{i\phi}|8,-6\rangle \otimes |3,-1\rangle, \qquad (5.7)
\end{aligned}$$

$$|AA\rangle = \frac{1}{4\sqrt{2}}(1+e^{i\phi})|7,-7\rangle \otimes |0,0\rangle - \frac{1}{4\sqrt{2}}(1+e^{i\phi})|7,-7\rangle \otimes |2,0\rangle, \qquad (5.8)$$

$$|SA\rangle = \frac{1}{4\sqrt{2}}(1-e^{i\phi})|8,-7\rangle \otimes |0,0\rangle - \frac{1}{4\sqrt{2}}(1-e^{i\phi})|8,-7\rangle \otimes |2,0\rangle, \qquad (5.9)$$

$$|AS\rangle = -\frac{1}{4\sqrt{10}}(1-e^{i\phi})|7,-7\rangle \otimes |1,0\rangle + \frac{3}{4\sqrt{10}}(1-e^{i\phi})|7,-7\rangle \otimes |3,0\rangle. \qquad (5.10)$$

Due to the one-to-one correspondence between the four nuclear spin symmetry channels and the rotational parity channels, $|SS\rangle \leftrightarrow |e,o\rangle$, $|SA\rangle \leftrightarrow |e,e\rangle$, $|AS\rangle \leftrightarrow |o,o\rangle$, and $|AA\rangle \leftrightarrow |o,e\rangle$, the population in each channel is proportional to the sum of the squared magnitudes of the probability amplitudes for all terms within that channel. As the applied phase ϕ is varied from 0 to 2π, the branching ratios exhibit a sinusoidal dependence on ϕ, as shown in Fig. 5.15. When $\phi = 0$, the two reactant molecules are identical, and the theory predicts complete suppression of the $|e,e\rangle$ and $|o,o\rangle$ channels—consistent with the symmetry-based argument discussed

earlier. In contrast, if no coherence is preserved throughout the reaction, the situation is equivalent to having a random phase ϕ uniformly distributed between 0 and 2π. Therefore, this approach provides a direct method to test whether quantum coherence is preserved throughout the reaction: by applying a phase ϕ and varying it from 0 to 2π, one expects to observe a modulation in the branching ratios if coherence is maintained.

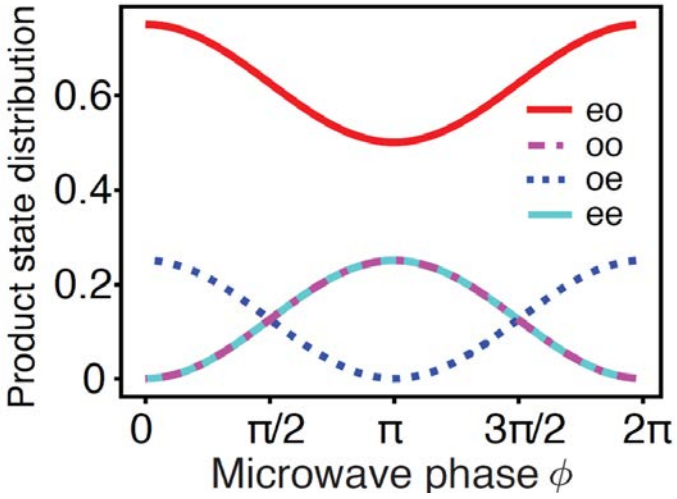

Figure 5.15: Product state distributions as a function of applied phase ϕ through microwave [118].

The above calculations demonstrate the possibility of coherently controlling reaction products. Next, we propose an experimental scheme to realize the microwave phase control of ϕ. An overview of the experimental sequence is shown in Fig. 5.16a. The KRb molecules, initially prepared in a single, well-defined quantum state, are first split into two spatially separated parts. Each cloud is then sequentially

addressed by microwaves and prepared in a superposition state with a controllable relative phase.

To enable this addressability, the individual optical traps holding the two molecular clouds are pulsed alternately, creating an AC Stark shift that shifts the resonance frequency of each cloud. While one cloud is momentarily dark, a microwave pulse with a tunable phase is applied to resonantly drive transitions, selectively preparing that cloud into the target superposition state while leaving the other largely unaffected. After both clouds are sequentially addressed, they are merged to initiate the chemical reactions.

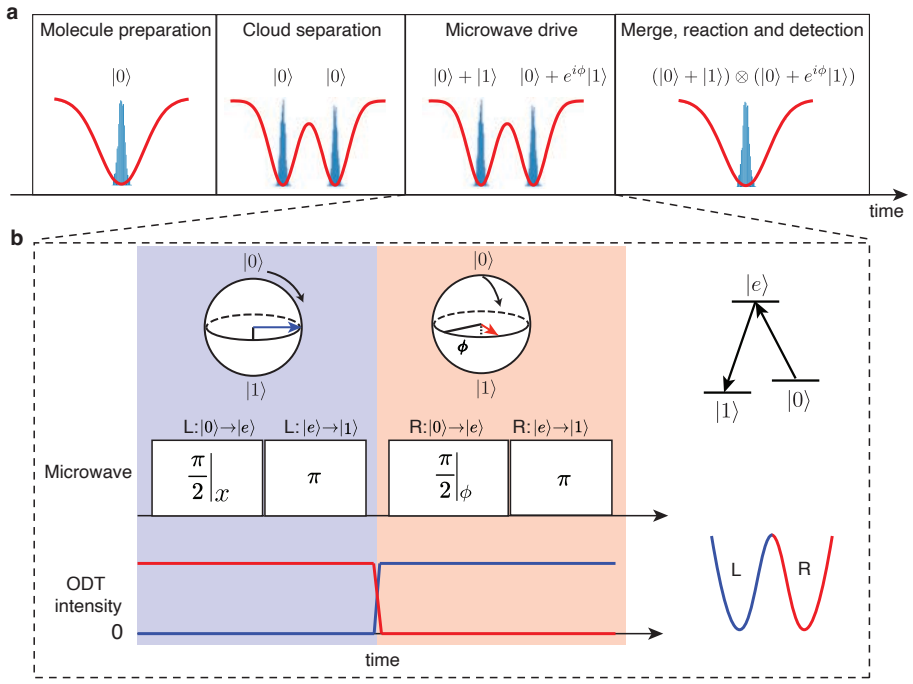

Figure 5.16: Experimental timing sequence [118]. (a) After molecule formation, the traps are adiabatically separated, which splits the molecular cloud into two spatially distinct regions. A microwave sequence is then used to imprint a relative phase ϕ between the two clouds. Finally, the clouds are merged, and the product state distribution is measured via coincidence detection. (b) Details of the microwave addressing scheme. By alternating the dark time between the left (L, blue) and right (R, red) traps, local AC Stark shifts are introduced, allowing for the selective addressing of each cloud. An arbitrary waveform generator can be used to control the relative phase ϕ between the two $\frac{\pi}{2}$ microwave pulses.

5.5 Conclusion and Outlook

In this section, we explored how the quantum state of the reactants influences the outcomes of ultracold chemical reactions, focusing on the KRb + KRb $\rightarrow$ K_2 + Rb_2 reaction. This was achieved by preparing KRb molecules in well-defined quantum states, including both energy eigenstates and coherent superposition states, allowing us to systematically investigate how reaction outcomes depend on the initial state.

Our results show that when reactants are prepared in a pure energy eigenstate (which can be a superposition in the Zeeman basis), the product distributions align with theoretical predictions based on nuclear spin conservation, provided that coherence is maintained throughout the reaction. However, when the reactants are prepared in superposition states, the outcomes become more complex: in some cases, the results are consistent with coherent evolution, while in others, coherence appears to be lost. Notably, we observed excess population in certain product channels that cannot be explained by our current theoretical model. This raises the possibility that nuclear spins may not be strictly conserved in these cases, or that the reaction pathway itself may imprint an additional phase, modifying the interference between different channels.

To further investigate these effects, we proposed a phase-sensitive interferometric scheme designed to test the presence of quantum coherence during the reaction process in a more general setting. Theoretical calculations predict that, if coherence is preserved, the branching ratios into different product channels should exhibit

sinusoidal dependence on the applied phase. In addition to testing coherence in ultracold reactions, this scheme opens up a promising pathway toward achieving coherent control of bimolecular reactions.

While we have investigated the existence of coherence within the nuclear spin degree of freedom during the reaction process for a specific initial state, a more fundamental and general question arises: Are the product K_2 and Rb_2 molecules quantum mechanically entangled? Addressing this question requires us not only to confirm the presence of nuclear spin coherence but also to establish coherence across different rotational states. In other words, can the bimolecular reaction be described as a coherent scattering process in which the products emerge in a pure quantum state, which is a coherent superposition of all allowed product channels labeled by their rotational and nuclear spin quantum numbers, rather than as a statistical mixture?

To prove this, it is necessary to demonstrate that the relative phases between different product channels are well-defined, rather than being completely random. The key challenge in this investigation is that the observable phase difference between any two channels (labeled as 1 and 2), ϕ_{total}, is composed of three contributions: a spatial evolution phase $\phi_s = (k_1 - k_2)r$, a time evolution phase $\phi_t = (\omega_1 - \omega_2)t$, and the intrinsic phase ϕ_0 imparted by the reaction process—which is the quantity of interest. Unfortunately, ϕ_s and ϕ_t are typically very large for most channel pairs, and their fluctuations can easily overwhelm the signal from ϕ_0.

To overcome this, the energy and momentum differences between the two

product channels must be made extremely small to minimize ϕ_s and ϕ_t. Achieving this requires high precision in both spatial and temporal resolution during detection. One possible strategy is to identify two nearly degenerate product channels, for which $k_1 - k_2$ and $\omega_1 - \omega_2$ approach zero. Realizing such conditions would demand extremely precise control over experimental parameters (potentially requiring stabilization of energy level differences between states 1 and 2 down to a hertz level) but could open the door to probing entanglement between reaction products.

Chapter 6

Resonant interaction between Rydberg Rb with KRb molecules

6.1 Rydberg excitation of Rb atoms

Dipolar interactions between cold and controlled species have been widely explored in various systems, as they can be utilized for entanglement, which serves as the basis for many quantum computing, quantum simulation, and sensing applications. Among these systems, significant progress has been made in the tweezer-trapped ultracold Rydberg atoms and polar molecules communities [119, 120, 121, 122]. While Rydberg atoms have large dipole moments and stronger interactions, polar molecules have a more complex internal structure, characterized by long-lived internal states and intrinsic, tunable interactions. Therefore, it would be beneficial to

combine technologies from both worlds by having an interacting Rydberg atom-polar molecule system, where one can utilize the dipolar interactions for applications.

Recently, a theory of using a hybrid system of Rydberg atoms and polar molecules had been proposed [123, 124], and an experimental demonstration of the inter-species blockade in the Rb*-RbCs system had been observed [125]. However, resonant inter-species dipolar interaction at ultracold temperatures has yet to be achieved. In this work, we study the resonant interactions between ultracold Rb Rydberg atoms and KRb molecules through two approaches: (1) direct observation of the products, and (2) broadening of the Rydberg excitation transition resulting from the resonant interactions. We then developed a dipolar interaction model to explain our observations.

6.1.1 Choosing the quantum state

Since we aim to study the resonant dipolar interaction between Rb and KRb, finding a pair of Rydberg states whose energy difference is close to the KRb rotation transition (at 2.227 GHz) is critical. Previous resonant energy transfer experiments in molecular beams [126, 127, 128] mainly used molecules with large transition frequencies, for example, ammonia, whose inversion transition frequency is $\sim$24 GHz [129]. The large transition frequency in those experiments allowed them to use a much lower Rydberg state in the range of n = 40 to 50. However, this is not the case for KRb molecules, as the rotation transition is only 2.227 GHz, meaning that

we must work with a pair of Rydberg states with much larger principal quantum numbers to match the transition frequencies.

Additionally, we employed a two-photon Rydberg excitation scheme to excite Rb atoms to the Rydberg state. This is a standard choice in the community as one-photon excitation requires significant power in the UV regime, which is experimentally very challenging, and multi-photon (more than 2) excitation is unnecessarily complicated and requires multiple lasers to be locked to each other. The two-photon excitation scheme we picked is a 420 nm that couples the ground state $5S_{1/2}$ to an intermediate excited state $6P_{3/2}$, which is then coupled to a Rydberg nS or nD state with a 1011 nm photon. Note that there exists another two-photon excitation scheme to the Rydberg state, which is 780 nm ($5S_{1/2}$ to $5P_{3/2}$) + 480 nm ($5P_{3/2}$ to nS or nD). We picked the 420 nm + 1011 nm scheme since generating high power (since the transition dipole is small) at 480 nm is technically challenging and expensive, as it typically requires frequency doubling of a Ti: Sapphire laser.

In a two-photon Rydberg excitation scheme, the atoms could only occupy an S or a D state at the end. We selected a D state as the target state because the nD to (n+1)P state energy separation is smaller, given a principal quantum number n. Nevertheless, we found that the closest state pairs are (98D, 99P), whose principal quantum numbers are large compared to typical Rydberg experiments in tweezer-based systems. We utilize the differential DC Stark shift of the two states to control the energy separation between them, which enables tuning the Rydberg atom and KRb molecule system into resonance.

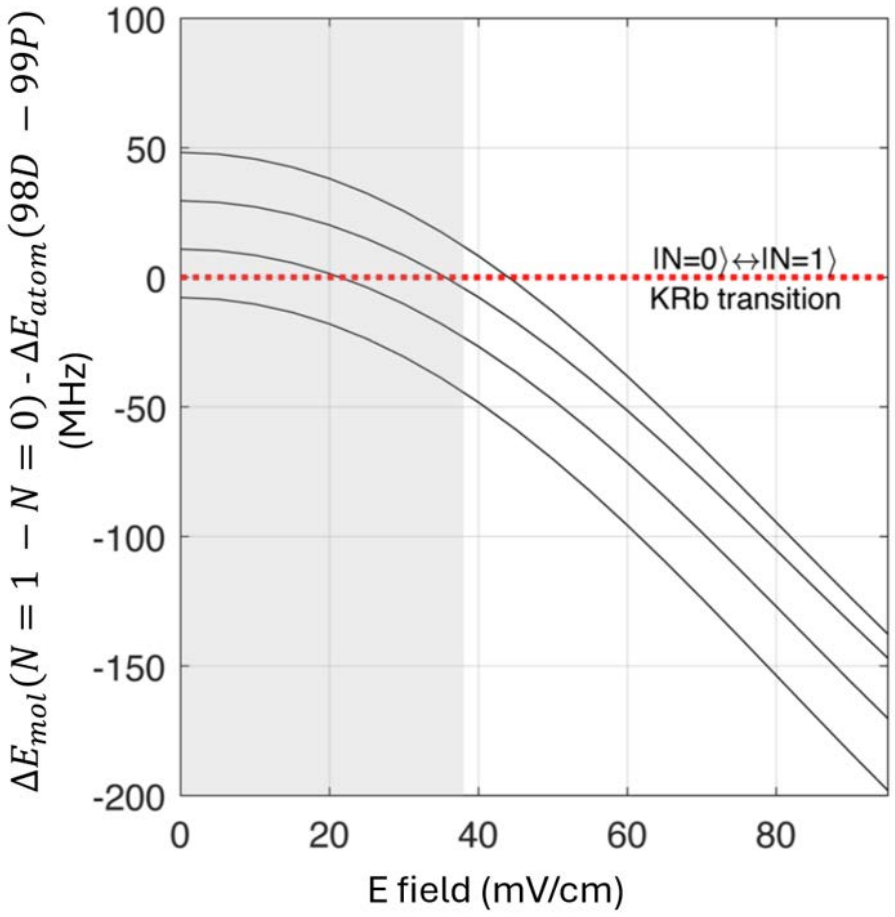

Figure 6.1: Energy spacing between the highest energy state in the $98D_{5/2}$ manifold and $99P_{3/2}$ states [130]. The y-axis stands for the pair state detuning between KRb $N = 0 \rightarrow N = 1$ and Rb 98 $D_{5/2} \rightarrow 99P_{3/2}$ transitions. The magnetic field is at 10 G. Starting with the highest energy eigenstate in the 98 $D_{5/2}$ manifold, it couples to four lower states in the 99 $P_{3/2}$ manifold. The energy differences are then computed under electric fields ranging from 0 to 100 mV/cm, as shown by the four black curves. For each 99 $P_{3/2}$ state, the resonant condition is satisfied at a particular electric field, represented by the intersection between the red dashed line and the corresponding black curve. Due to constraints of the residual electric field and geometries of our electrodes, we cannot reduce the electric field below E = 38 mV/cm.

6.1.2 Laser system

Our Rydberg laser system comprises two lasers, operating at 420 nm and 1011 nm, along with their respective control and locking electronics. The 420 nm laser (Toptica DL pro) is an ECDL with a maximum power of approximately 50 mW at the time of our initial purchase. The 1011 nm laser (Home-built based on an Innolume gain module) is also an ECDL with both fiber and free-space outputs. Originally, we chose this particular 1011 nm gain module and design, hoping to achieve high power without multi-moding and mode hops, which turned out to be highly challenging. Therefore, we operate at a current of approximately 160 mA (corresponding to less than 20 mW from the fiber output and 2 mW from the free-space output) to avoid multimoding. Since the transition dipole moments between the $6P_{3/2}$ state and the Rydberg states are very small, we need sufficient power at this frequency. Ideally, one would use a Yb-doped fiber amplifier to gain laser power on the Watt level. However, we had to use a semiconductor optical amplifier (SOA, Innolume), which only provides a power of $100 \sim 200$ mW due to budget constraints.

As shown in Fig. 6.2, we split the 420 nm laser beam into three paths: a frequency monitor with a wavelength meter, a locking path that goes to a transfer cavity, and a path to the experiment. On the other hand, the 1011 nm laser has two outputs: a fiber output and a free-space output. The free space output accounts for approximately 10% of the total power and is used for frequency locking. It's sent through a fiber-based EOM modulated with two frequency tones f_s and f_m for sideband locking. Typically, we select $f_m = 10$ MHz to generate sidebands for PDH

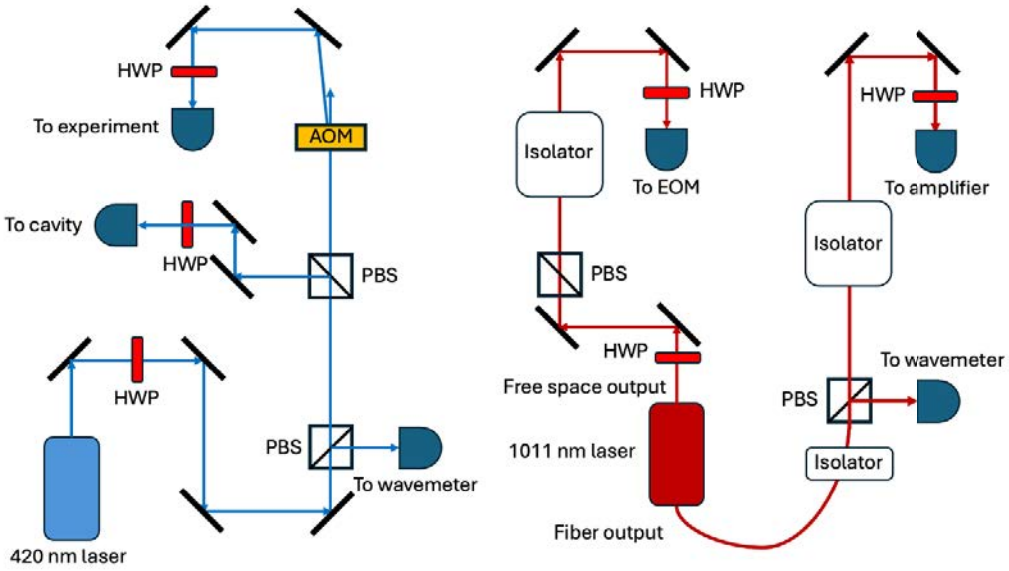

Figure 6.2: Rydberg laser system (cavity locking and amplifier excluded).

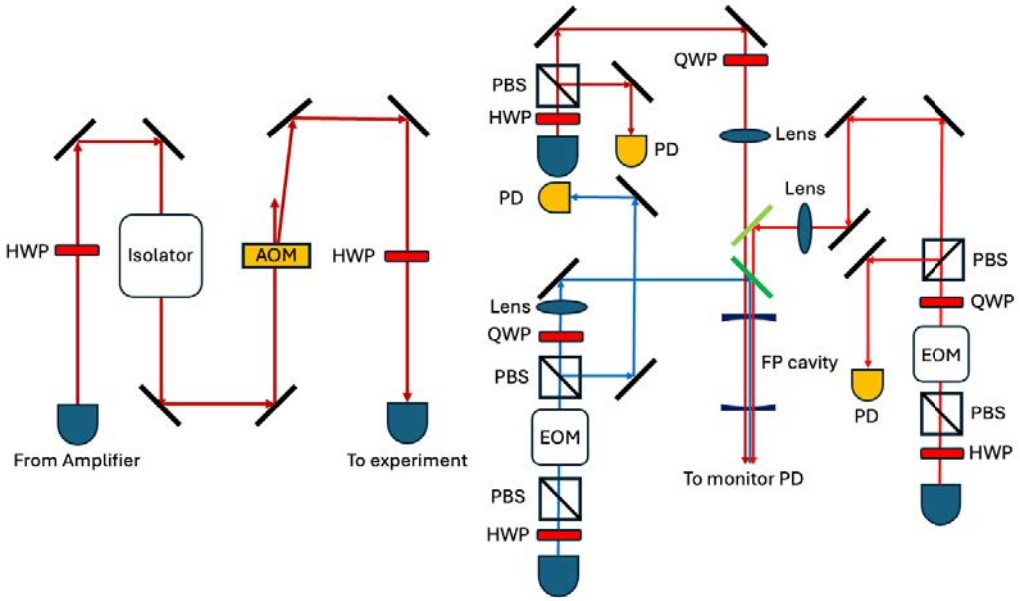

Figure 6.3: The amplifier setup of the 1011 nm laser and the locking setup for the Rydberg lasers.

locking, while f_s can vary between 30 MHz and 1.5 GHz (ultimately limited by the cavity). This allows us to lock one of the sidebands to a reference cavity, and the carrier frequency can be dynamically tuned as we sweep f_s. Formally, we denote the carrier frequency of the laser as f_c, then the two sidebands would be at $f_c + f_s$ and $f_c - f_s$. Assuming the reference cavity resonance is at f_0, we could have either $f_c + f_s = f_0$ or $f_c - f_s = f_0$ when we lock the positive or negative sidebands to the cavity. In both cases, f_c (the laser frequency) can be tuned by changing f_s.

Both 420 nm and 1011 nm beams are sent to their locking paths (shown in Fig.6.3), and are locked to the transfer cavity through a standard PDH locking technique. We modulate the 420 nm beam with a free-space EOM (phase modulation) at 10 MHz, which is then sent to the Fabry-Perot cavity. The reflection of the cavity is picked up by a photodetector and is mixed with the modulation signal to generate the error signal used for frequency locking and stabilization. The 1011 nm beam, on the other hand, has been modulated by a fiber-based EOM, so we could directly couple it to the cavity.

Since we reference both Rydberg lasers to the cavity, it is critical to keep the cavity as a stable reference. Specifically, the cavity length must be maintained stable against changes in environmental conditions, such as temperature, humidity, and air pressure. An example of such cavities is an ultra-stable cavity (Stable Laser Systems) that we used to lock our STIRAP lasers, which utilizes ULE glass as the spacer and is placed inside a high vacuum (10^{-7} Torr) with temperature stabilization down to the mK level. ULE glass typically has a thermal expansion

coefficient of as low as 10^{-8}/K [131]. When operating near their near-zero coefficient of thermal expansion (CTE) temperatures (since their CTEs are generally nonlinear as a function of temperature), one can achieve maximal cavity length stabilization by placing the entire system in an enclosure with a temperature servo, which reduces temperature fluctuations to below 5 mK. In addition to controlling the physical cavity length, the cavity is also pumped to a high vacuum to prevent changes in ambient air pressure from affecting the cavity resonances. With all the aforementioned techniques, a stable cavity can achieve frequency stability on the order of the kHz level. While a stable cavity would be ideal for our applications (and many other Rydberg experiments), the cost of such a system is significant. In addition, Rydberg excitation is a bulk gas system that has intrinsically significant decoherence rates [132], so that a simpler system could be used to achieve a similar performance.

Therefore, we select a simpler transfer cavity system, where one can use a stable laser as a reference, and stabilize the cavity length to the reference laser. Here, we choose the 968 nm laser (STIRAP first leg) as the reference since it is locked to an ultra-stable cavity. The transfer cavity follows a confocal cavity design as shown in Fig. 6.4. We use Invar (64% Fe, 36% Ni) as the cavity spacer material due to its low thermal expansion property (CTE: 1.2×10^{-6}/K). Note that the CTE of Invar is two orders of magnitude larger than that of the ULE glass, but it is significantly easier to source, machine, and handle. We attach one plano-concave mirror to one end of the spacer and a ring piezo on the other end with vacuum-compatible

epoxy (Masterbond EP21TCHT-1). The ring piezo (Thorlabs PA44M3KW) is then sandwiched between the cavity spacer and the second plano-concave mirror. The two plano-concave mirrors are half-inch in diameter and have a radius of curvature of r = 50 mm. The two curved surfaces are coated with a 99.92% reflection coating at 0° angle of incidence (AOI) for wavelengths of 410-440 nm and 950-1030 nm, and the two flat surfaces are coated with an anti-reflective coating (0.1% reflection) for the same wavelengths. We place the transfer cavity under a vacuum of 10^{-8} Torr. Note that we did not have to bake the vacuum chamber to achieve this pressure.

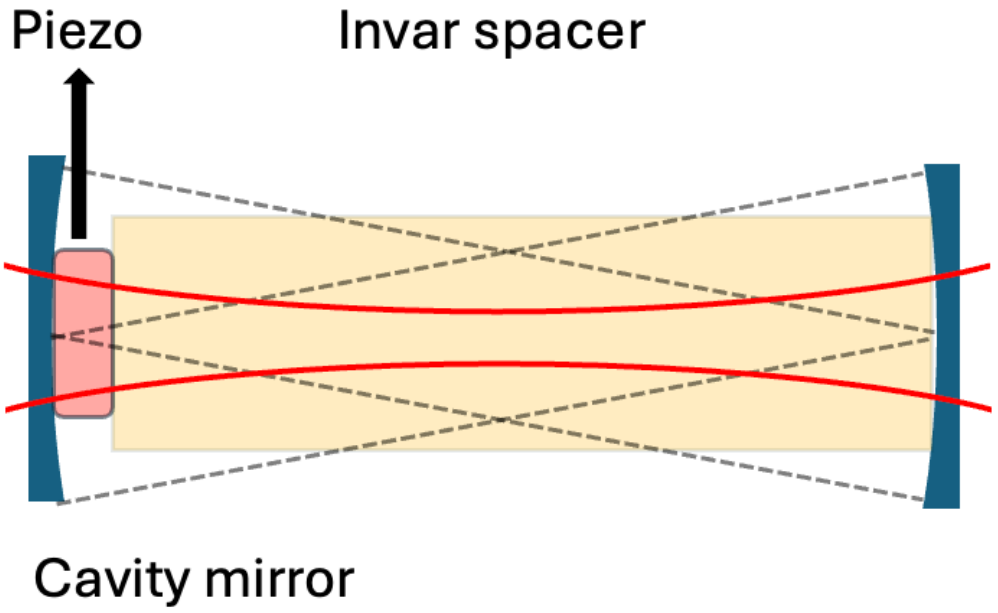

Figure 6.4: Confocal transfer cavity schematics. The transfer cavity consists of a hollow metallic cylinder made of Invar. Two plano-concave mirrors are glued to the cavity spacer, with an additional ring piezo sandwiched between one of the mirrors and the spacer. Before assembly, we sonicated the Invar spacer in Simple Green and then in acetone to remove the residual grease attached to the spacer during machining. In practice, one can choose any length for the spacer as long as the cavity satisfies the stability condition: $0 \leq (1 - \frac{L}{R_1})(1 - \frac{L}{R_2}) \leq 1$, where R_1 and R_2 are the radius of curvature of the concave side of the mirrors.

While an ultra-stable cavity relies on its passive stability, our transfer cavity is stabilized in a closed-loop configuration with feedback on the ring piezo, which expands/contracts under an external voltage. This is achieved by setting up a PDH

locking scheme for the 968 nm reference laser. Instead of feedback on the 968 nm laser itself, we send the feedback voltage to the ring piezo. After the transfer cavity is stabilized to the reference laser, we apply standard PDH locking of the 420 nm and 1011 nm lasers to the cavity. In this way, we effectively transfer the 968 nm laser lock to the 420 nm and 1011 nm lasers.

The transfer cavity has its characteristic spatial modes, which are the Gaussian modes [133]. In most cases, one would want to couple to the TEM_{00} mode. This requires the incoming laser beam to have the same spatial mode as the TEM_{00} mode. Therefore, the choice of beam diameter and focusing lens is essential. To calculate the TEM_{00} mode beam waist ($1/e^2$ beam radius) at the center of the cavity, we follow its expansion at the mirrors, where the radius of curvature of the wavefront equals the curvature of the mirror. Therefore, we have:

$$R = \frac{L}{2}(1 + \frac{4z_R^2}{L^2}) \tag{6.1}$$

where z_R is the Reyleigh range:

$$z_R = \frac{\pi\omega_0^2}{\lambda} \tag{6.2}$$

with ω_0 and λ being the beam waist and wavelength. Given design parameters R (radius of curvature of the plano-concave mirror) and L (cavity length), one can then calculate ω_0.

Before we move on to the Rydberg spectroscopy section, I will include some

discussions on earlier iterations of the Rydberg locking system.

In the original design of the Rydberg excitation system (late 2019 - early 2020), we planned to use a vapor cell + EIT system to lock the two lasers. First, the 420 nm laser is locked to a Rb transition with saturated absorption spectroscopy via a Rb vapor cell. Then we could use EIT to lock the 1011 nm laser to a Rydberg transition with 420 nm as the probe light and 1011 nm as the control light. However, we were unable to observe the EIT transmission peak after extensive experimental efforts. This can be attributed to an intricate mechanism causing EIT peaks to disappear inside vapor cells when the probe frequency is significantly larger than the control frequency. A quantitative analysis of this effect could be found in [134].

The very first transfer cavity (late 2020 - early 2021) that we built contained a cavity spacer held together with springs pressing against three piezo chips (Thorlabs Fabry-Perot cavity spacers). Although we could generate an error signal with the PDH technique, the locking performance was very poor. After investigation, we found that the mechanical resonance frequency of the system was too low, resulting in a phase-shifted feedback signal that caused instability in the lock. Therefore, in the following version of the transfer cavity, we intentionally designed the system to be free from springs and maintained a small effective mass load on the piezo ring (approximately equal to the mass of the cavity mirror) to increase the mechanical resonance frequency.

The second generation of transfer cavity (mid-2021 to early 2023) had a similar structure to the latest version. However, we did not realize the importance of

placing the cavity under vacuum. We naively thought that the feedback mechanism could cancel out changes in the air pressure (the refractive index). While we could successfully excite Rb atoms to the Rydberg states and perform spectroscopy, we found that the sideband modulation frequency f_s of the Rydberg resonance had a slow, random drift on the order of 10 MHz, making it very challenging for us to perform long scans. It turned out that this long-term drift is caused by air dispersion. To demonstrate the physics behind such an effect, we assume the refractive index of air to have a linear dependence on the pressure $n = 1 + \alpha P$, when the effective cavity length is L_0 for one frequency, the actual length of the cavity is:

$$L = \frac{L_0}{1 + \alpha_1 P} \tag{6.3}$$

where the subscript denotes the frequency used for reference. The optical path length for a different frequency is:

$$L = L_0 \frac{1 + \alpha_2 P}{1 + \alpha_1 P} \tag{6.4}$$

When the pressure changes to $P + \delta P$, the change in the effective optical path length of the second frequency is:

$$\delta L = L_0 \left(\frac{1 + \alpha_2 (P + \delta P)}{1 + \alpha_1 (P + \delta P)} - \frac{1 + \alpha_2 P}{1 + \alpha_1 P}\right) \simeq L_0 \frac{\alpha_2 - \alpha_1}{(1 + \alpha_1 P)^2} \delta P \tag{6.5}$$

We showed that this effective path length has a linear dependence on the change in air pressure δP, which is non-negligible when exposed in the atmosphere.

To overcome this issue, we designed the third-generation transfer cavity (2023-present) to be vacuum-compatible and placed it under high vacuum. To this

end, we have not observed slow drifts of the Rydberg excitation frequency beyond the wavemeter resolution of 1 MHz.

6.1.3 Rydberg laser beam path into the experiment

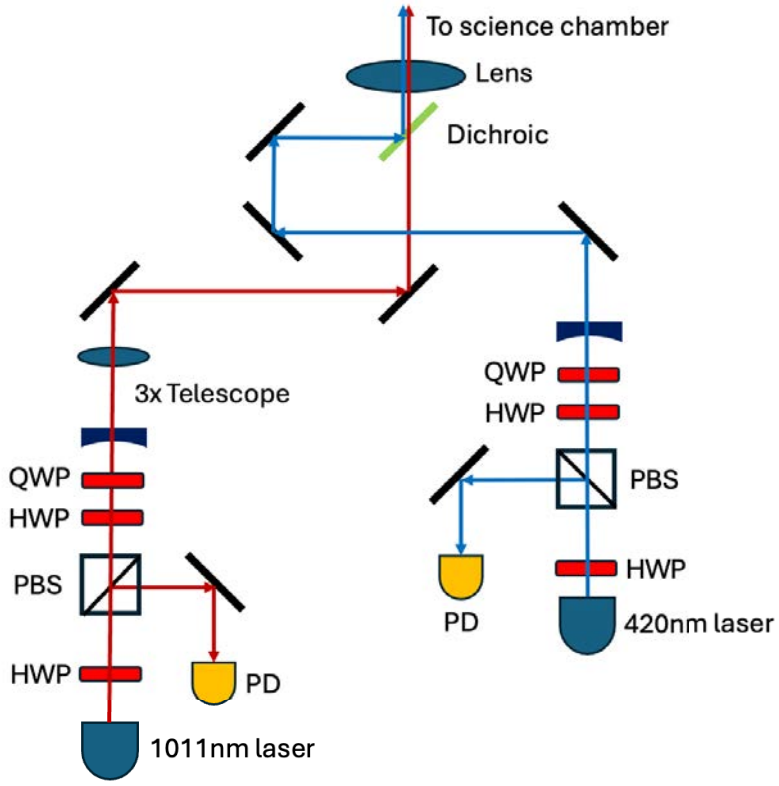

Figure 6.5: Rydberg beam path on the science table before being delivered to the science chamber.

Typically, we obtain 1-2 mW of 420 nm laser power and 25-50 mW of 1011 nm laser power directly from the fibers on the science table. We use a setup shown in

Fig. 6.5 to focus the Rydberg beams and deliver them to the experiment. Our design Rydberg beam size is 60 μm ($1/e^2$ beam radius) for both wavelengths. If the beam size is too small, any mechanical motion (either vibration or thermal) would cause significant shifts in the beam pointing, resulting in drastic changes in the Rabi rate. If the beam size is too large, the Rabi rate would be lower. Our choice of beam size strikes a balance between maintaining reasonable mechanical stability and achieving a sufficiently high Rabi rate.

To achieve this small beam size, we magnify the 420 nm and 1011 nm beams before a final focusing lens with a focal length of f = 500 mm. This is because we have to combine the Rydberg beams before merging them with the K/Rb imaging beams. Since the imaging beam path is about 500 mm long, it means that the final focusing lens of the Rydberg light would have a focal length longer than 500 mm.

6.1.4 Field ionization and detection of Rydberg Rb atoms

Detection of Rydberg atoms is achieved through electric field ionization. In this process, we increase the voltage on the plate electrodes, creating an electric field around the Rydberg atoms. When the applied electric field is large enough, it allows quantum tunneling of the loosely bound Rydberg electron and ionizes the Rydberg atom, by changing the potential energy curve the valence electron experiences. The core potential effectively creates a local minimum that traps the outer electron. When the external field is sufficiently large, the outer electron could tunnel out at a

fast rate and therefore cause ionization of the atom.

The field ionization threshold depends on the principal quantum number n. A quick order-of-magnitude estimate of the threshold electric field could be found in [135]:

$$E_c = \frac{5.7 * 10^8 \mathrm{V/cm}}{n_{\mathrm{eff}}^4} \tag{6.6}$$

where n_{eff}= n - δ_L and δ_L is the L-dependent quantum defect. It should be noted that the above estimation ignores the on-time of the electric field, which plays a critical role in the field ionization process [136, 137]. Experimentally, we attempted to measure the ionization threshold for the $35D$ state by measuring the number of Rb ions as a function of the electric field. We observed a continuously growing trend in Rb ion counts as the electric field was increased until a threshold of 58 V/cm, at which point the ion signal began to saturate. This threshold appeared lower than what one would expect from Eq. 6.6. We believe the reason is that we used a very long E field pulse of 30 μs, which allows tunneling of the Rydberg electron from potentially more pathways. This is consistent with a long time-of-flight (TOF) tail we observed for the Rb ion signal at low electric fields.

6.1.5 Rydberg spectroscopy - An example

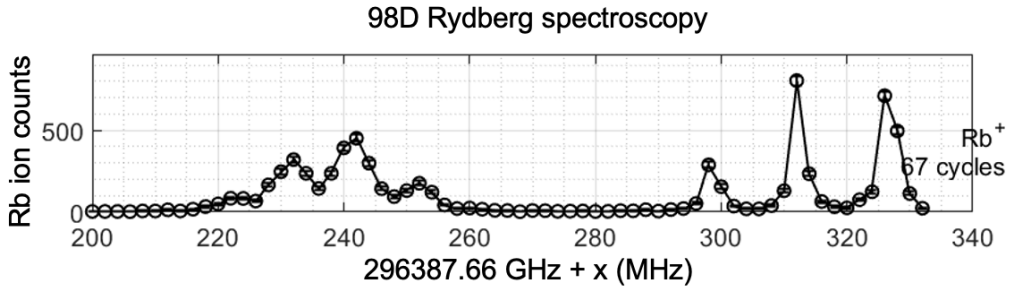

Figure 6.6: The 98D state spectroscopy as we scanned the 1011 nm laser frequency. The electric field is 54 mV/cm, and the magnetic field is 0 G in the system.

Here, we provide an example for a Rydberg excitation spectroscopy scan of the 98D state, which involves both $98D_{3/2}$ and $98D_{5/2}$ as the fine structure splitting at n = 98 is as small as tens of MHz, comparable to the Stark shift. The spectrum shown in Fig.6.6 was taken at an electric field of 54 mV/cm and a magnetic field of zero. Therefore, some 'Zeeman states' ('Zeeman state' is not very appropriate here as Stark shift is the dominant perturbation) are degenerate, so we did not observe all 10 states in the 98D manifold. We note that the electric field of 54 mV/cm is not directly obtained from the experiment, but rather from comparing the peak locations with theoretical predictions.

6.1.6 Electric field calibration

In the previous section, we showed an example of a Rydberg spectroscopy measurement. The splitting between the Zeeman states depends on the external electric and magnetic fields. We could utilize the splitting in spectroscopic measurements to compare with theory and extract the electric field inside the system at different applied voltages.

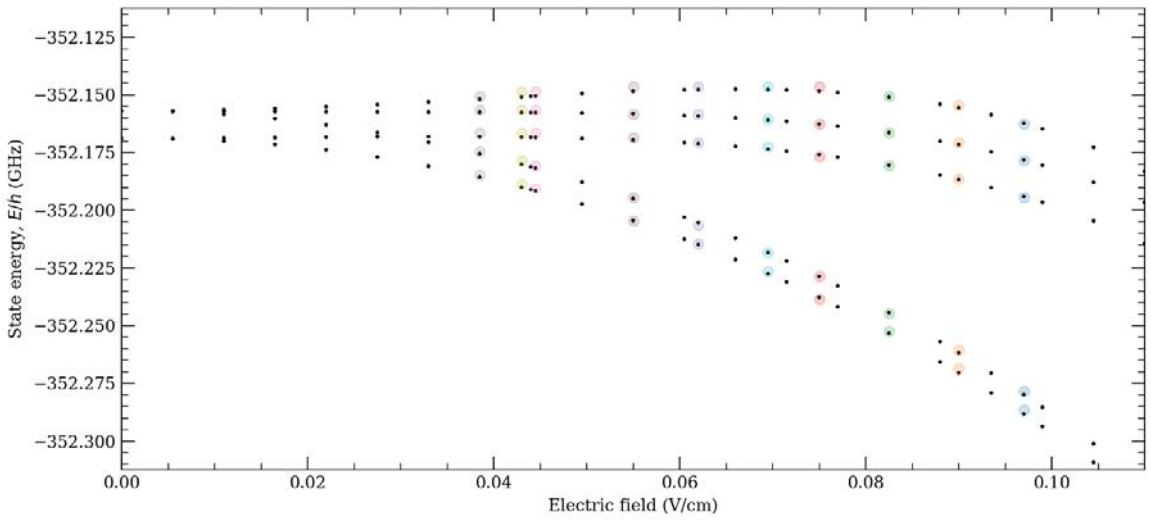

Figure 6.7: Extracting electric field from Rydberg spectroscopy measurements. Black dots represent theoretical predictions, and colored dots denote experimentally measured peaks. The magnetic field is set to zero for all calculations and experiments. The relative spacing of the peaks can be used to extract the electric field, up to ∼2 mV/cm precision.

Additionally, a conversion is required between the applied voltage on the extractor plate and the electric field within the system. The geometry of the electric

fields is shown in Fig. 6.8. Our goal is to measure the projection of the residual electric field E_{res} in the x,y,z directions. In this coordinate system, the x-axis is the direction of the magnetic field (vertical in real space), and the z-axis is the time-of-flight axis (along the time-of-flight tube). Due to the concentric geometry of the plate electrodes, the applied compensation electric field E_{applied} is along the z-axis. The total electric field E_{tot} with an applied voltage on the repeller plate V_{rep} is:

$$E_{\text{tot}} = \sqrt{E_{\text{minimal}}^2 + (E_{\text{res},z} + \alpha V_{\text{rep}})^2} \tag{6.7}$$

E_{minimal} and $E_{\text{res},z}$ are the perpendicular and parallel components of the residual electric field relative to the z-axis. α is a conversion factor between the applied voltage and the electric field E_{applied}. As we scanned V_{rep}, we performed Rydberg spectroscopy scans for the $98D$ states similar to Fig. 6.6, which were compared with theoretical calculations to extract the electric fields as shown in Fig. 6.7. These extracted electric fields were then plotted against the V_{rep} and fitted using Eq. 6.7, where we determined $E_{\text{minimal}} = 38.6$ mV/cm and $E_{\text{res},z} = 88.5$ mV/cm.

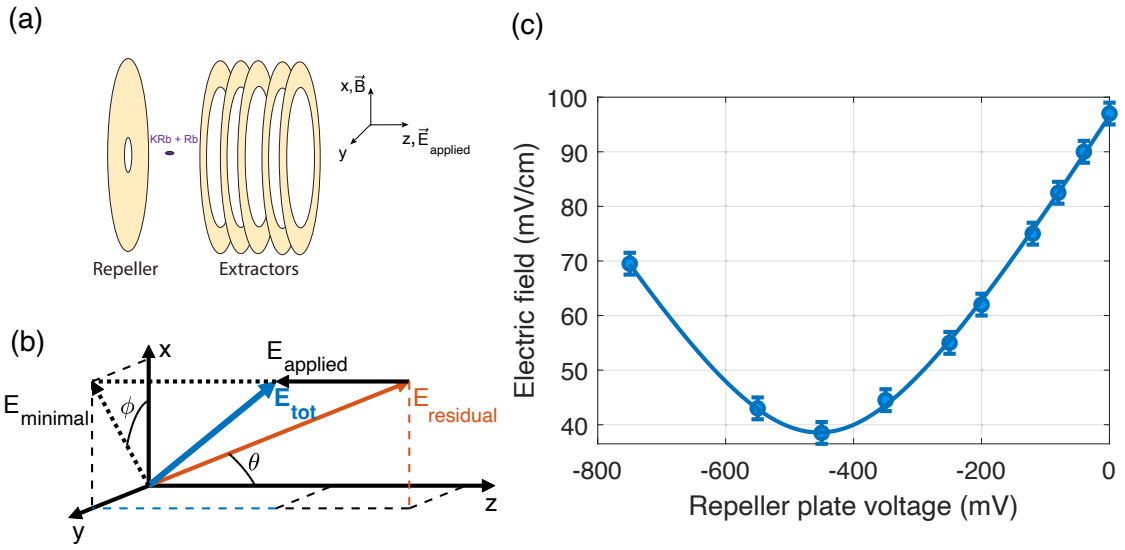

Figure 6.8: Geometry and calibration of electric field [130]. All data points were taken at a magnetic field of 0 G. The black curve is fitted using Eq. 6.7.

In addition to determining the field magnitude, we also aim to measure the angle ϕ between the x-axis and the direction of the minimal electric field, E_{minimal}. This angle was extracted by comparing the Rydberg excitation spectrum at a finite magnetic field of $B = 10$ G with theoretical predictions. Although the theoretical model does not perfectly reproduce all spectral peaks, we found that $\theta = 55°$ provides the best match to the experimental data. Notably, a mysterious peak appears in the spectrum that is not captured by the theory. We speculated that such a feature may arise from a two-body excitation process leading to the formation of a Rydberg long-range molecule [138, 139]. Despite this, we used $\theta = 55°$ in the Monte Carlo simulations of Rydberg broadening presented in the following sections, as we

found that the linewidth is largely insensitive to small variations in θ.

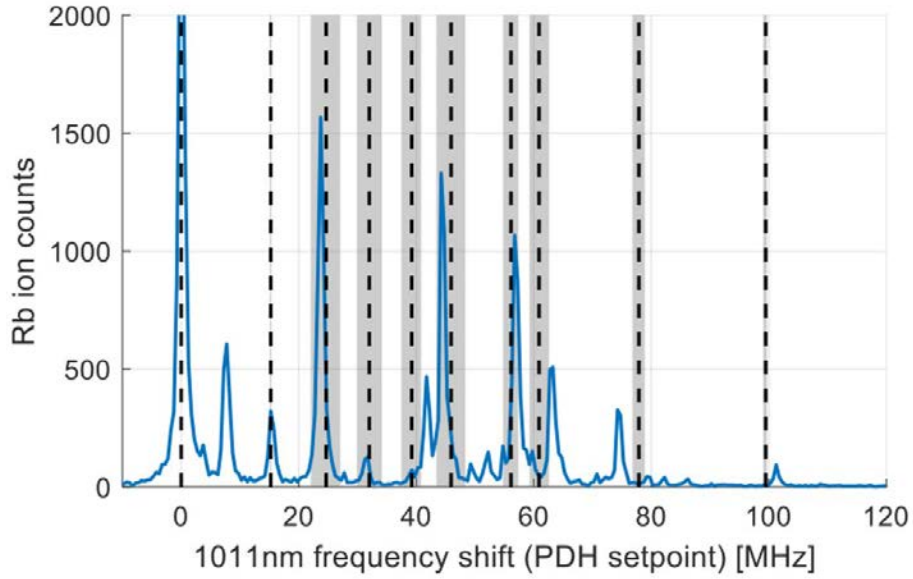

Figure 6.9: Calibration of the angle θ between the minimal electric field and the magnetic field. The blue curve is the measured Rydberg excitation spectrum. The black dashed vertical lines are theoretical predictions at a magnetic field of B = 10 G, E = 38.6 mV/cm and $\phi = 55°$, and the gray bars represent the range of predictions with ± 5 degrees uncertainty of ϕ. We aligned the leftmost (the highest in energy) theory line and experimental transitions at x = 0 for a direct comparison. We note that a MHz-level mismatch in frequencies (x-coordinates) may exist between theory and experiment, primarily due to the accuracy of theoretical calculations.

6.2 Resonant interaction between Rydberg Rb atoms and KRb molecules

After selecting the appropriate Rydberg states, constructing the Rydberg excitation lasers and the locking system, and determining the ion detection system, we could study the interactions between the Rydberg atoms and molecules. In particular, we investigated the outcomes of resonant interactions between Rydberg Rb atoms and KRb molecules. We began our experiment by creating a mixture of electronic, rovibronic ground-state KRb molecules and Rb atoms in the electronic and hyperfine ground-state, at a temperature of ~ 400 nK. The atom-molecule mixture was spatially confined in the XODT and the initial quantum state of KRb molecules was $|m_{I_{\mathrm{K}}} = -4, m_{I_{\mathrm{Rb}}} = 1/2\rangle$, where m_I represents the projection of nuclear spins onto the quantization axis defined by the magnetic field. The Rb atoms were prepared in the lowest energy hyperfine state $|F = 1, m_F = 1\rangle$. Following the creation of the atom-molecule mixture, we ramped down the magnetic field to 10 G in 10 ms. We waited an additional 40 ms to allow the magnetic field to stabilize, after which we were ready for Rydberg excitation.

Our excitation-detection sequence is as follows: We fired 5000 excitation-detection pulses over the course of 1 second to drive the Rb atoms to the Rydberg state and probe the resonant interaction between KRb and the Rydberg atoms. In each pulse, we first turned off the ODT light to keep the atom-molecule cloud in the dark, followed by a Rydberg excitation laser pulse for 3 μs driving the Rb atoms

from the ground state to the 98 $D_{5/2}$ state. Since the 98 $D_{5/2}$ state has a large principal quantum number, the blockade radius is about 20 μm, which is comparable to our atom-molecule cloud sizes. Therefore, we excited at most a few Rydberg atoms per laser pulse.

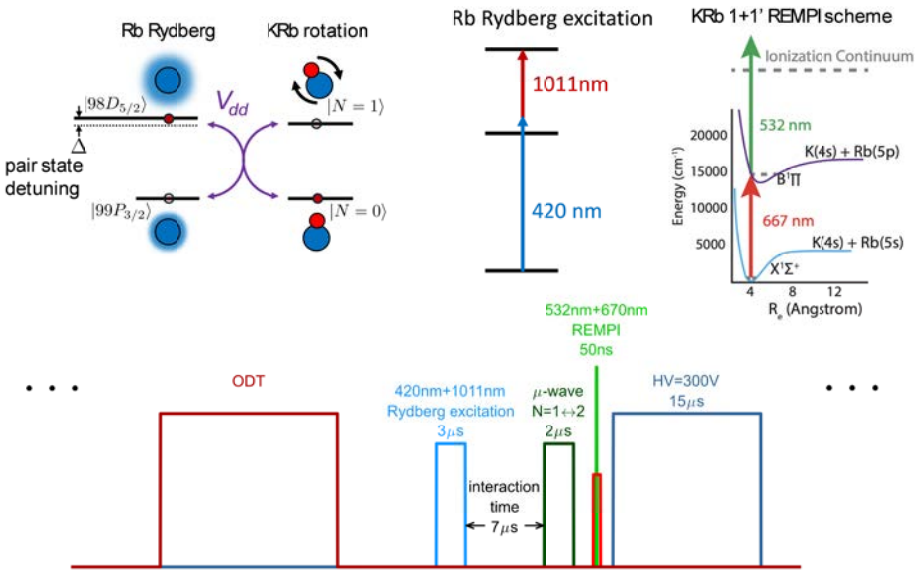

Figure 6.10: Schematics of the experimental sequence to probe resonant interactions between Rydberg Rb atoms and KRb molecules [130]. (a) The pair state detuning Δ, now defined as $\Delta = \Delta E_a(98D_{5/2} - 99P_{3/2}) - \Delta E_m(N = 1 - N = 0)$, can be tuned external electric and magnetic fields. (b) Two-photon excitation scheme of Rb atoms to the $98D_{5/2}$ state through the $6P_{3/2}$ intermediate state. (c) REMPI detection scheme of KRb molecules. We use a 4.454 GHz microwave pulse to drive $N = 1$ molecules to the $N = 2$ state before applying the ionization laser pulse. The REMPI laser pulse consists of two parts: a 667 nm pulse transferring the KRb molecules from $X^1\Sigma^+$, $\nu = 0$, $N = 2$ to the electronic excited state $B^1\Pi, \nu' = 0, N' = 1$, and then a 532 nm pulse ionizing the excited molecules. Implementing this scheme helped us reduce the off-resonant ionization of $N = 0$ KRb in the ensemble, compared to directly ionizing $N = 1$ molecules. (d) Experimental sequence for an excitation-detection cycle. We switched off the ODT light and applied the Rydberg excitation pulse for 3 μs. After waiting for 7 μs for the Rydberg atoms to interact with KRb, the Rydberg atoms were field ionized and extracted along with the KRb ions.

6.2.1 Excitation of KRb molecules

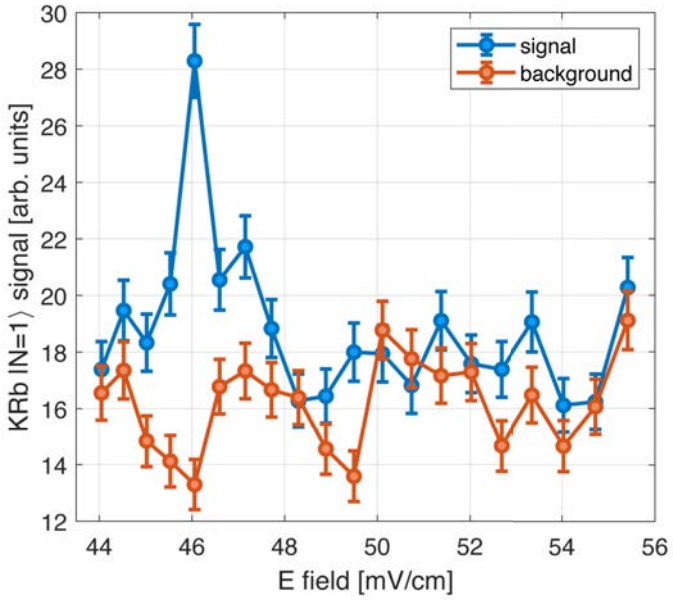

Figure 6.11: Electric field dependence of resonant interactions between KRb molecules and Rydberg Rb atoms [130]. The blue circles and orange circles represent the signal and background. The signal data were taken with the Rydberg excitation light resonant to the two-photon transition $5S_{1/2} \rightarrow 98D_{5/2}$. The background data were measured with the excitation light 70 MHz detuned (by increasing the IR frequency), such that no Rydberg excitation can be observed (zero Rb ion signal). We observed a prominent feature at $E = 46$ mV/cm at the Rydberg atom-molecule resonance.

The first step of our experiment is to directly prove and demonstrate the resonant energy transfer process by directly probing excited KRb molecules in the rotational

excited state N = 1 using REMPI [77]. Intuitively, our REMPI light should target the $N = 1$ molecules. However, we found that the off-resonant ionization of $N = 0$ molecules became significant, resulting in a large background noise floor. Therefore, we first drive these $N = 1$ molecules to $N = 2$ with a 4.454 GHz microwave pulse and then ionize them with a REMPI scheme that targets $N = 2$. This method enabled us to increase the REMPI down-leg detuning by a factor of three, thereby minimizing the off-resonant ionization of $N = 0$ KRb.

As shown in Fig. 6.11, we observed a narrow and prominent KRb ion signal at $E = 46$ mV/cm. This peak, which is close to the calculated resonance based on [140], corresponds to the transition to the highest energy state in the $99P_{3/2}$ manifold. We did not observe any additional resonances at higher electric fields, consistent with theoretical predictions. We note that we observe a small discrepancy between the measured resonance E field and the prediction (near $E = 44$ mV/cm). Such a small discrepancy may originate from two sources: 1. uncertainties of our electric field calibration, and 2. uncertainties of the $99P_{3/2} \rightarrow 98D_{5/2}$ transition frequency that we obtained from the ARC package [140], which we suspect to have an accuracy of a few MHz for the state pair we chose.

6.2.2 Broadening of the Rydberg excitation transition

While we can directly probe the excited KRb molecules resulting from the resonant interactions, we can also study the other involved species: Rydberg atoms. In

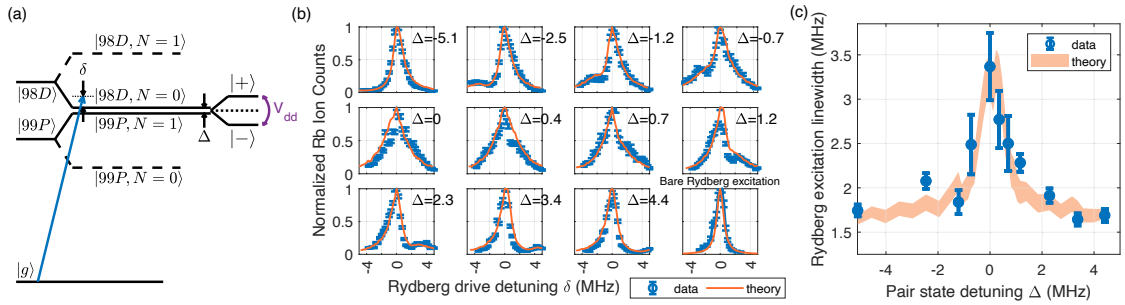

Figure 6.12: Broadening of Rydberg excitation linewidth [130]. (a) A dressed-state picture of an interacting Rydberg Rb atom and a KRb molecule. The eigenstates $|+\rangle$ and $|-\rangle$ are linear combinations of the bare states and are functions of the pair state detuning Δ and the interaction strength V_{dd}. δ represents the Rydberg drive detuning here. (b) The experimental (blue) and theoretically calculated Rydberg excitation spectra (orange) for all pair state detuning Δ in units of MHz. The theoretical spectra are simulated using a Monte Carlo method based on a dipolar interaction model. (c) The FWHM of the Rydberg excitation transition as a function of pair state detuning. The experimental uncertainties represent shot noise in the ion signal, and the theoretical uncertainties include both Monte Carlo sampling error and uncertainties in the input parameters (mainly dimensions of the Rb-KRb cloud).

fact, the detection of Rydberg atoms yields a significantly improved signal-to-noise ratio in the data, enabling a more quantitative analysis of the interaction strength and characteristics. Here, we measure the Rydberg excitation spectrum to extract information for the resonant interaction. To study the resonant aspect of this interaction, we measure the Rydberg excitation spectrum at varying electric fields, which allows us to control the pair state detuning Δ. We observe a broadening of the Rydberg excitation transition near the atom-molecule resonance (zero pair state detuning) as shown in Fig.6.12(b). We can quantify the broadening by applying a Savitzky-Golay smoothing filter and then extracting the corresponding FWHM, which are shown in Fig.6.12(c) [141]. In general, we observe an additional broadening of about 2 MHz at a peak KRb density $4.29 \pm 0.36 \ \times 10^{11}/\mathrm{cm}^3$.

Intuitively, near the atom-molecule resonance ($\Delta \lesssim V_{dd}$), the interspecies interaction couples the pair states $\{|98D, N = 0\rangle, |99P, N = 1\rangle\}$ and forms two dressed states $|+\rangle$ and $|-\rangle$ as illustrated in Fig. 6.12(a), both of which can be excited to from the atomic ground state. The existence of the two excited states leads to a double-peak excitation spectrum with the spacing set by V_{dd}. However, due to the random spatial distribution of the atoms and molecules in the ensemble, V_{dd} varies, leading to an inhomogeneous broadening of the Rydberg excitation as we observe (Fig. 6.12(b)).

To better understand and quantify our findings, we model the Rydberg atom-molecule interactions as a dipolar interaction and perform a Monte Carlo simulation based on the dipolar Hamiltonian (special thanks to Jeshurun Luke, who

implemented this simulation):

$$H_{DD} = \frac{1}{4\pi\epsilon_0} \frac{\mathbf{d}_{\text{atom}} \cdot \mathbf{d}_{\text{mol}} - 3(\mathbf{d}_{\text{atom}} \cdot \hat{\mathbf{r}})(\mathbf{d}_{\text{mol}} \cdot \hat{\mathbf{r}})}{r^3} \tag{6.8}$$

where $\mathbf{d}_{\text{atom}}$, $\mathbf{d}_{\text{mol}}$ are the dipole operators of the Rydberg atom and molecule, respectively, and $\mathbf{r}$ is the displacement vector from the atom to the molecule ($\hat{\mathbf{r}}$ is the unit vector of $\mathbf{r}$). Because our experiment is based on a bulk ensemble, we perform a Monte-Carlo simulation to account for the randomness of the atom-molecule distances and orientations. Specifically, we generated two clouds of Rb atoms and KRb molecules following 3-dimensional Gaussian distributions with sizes Rb : $(\sigma_x = 7.3 \pm 0.25, \sigma_y = 53.2, \pm 4.3, \sigma_z = 7.3 \pm 0.25)\,\mu$m and KRb : $(\sigma_x = 6.0 \pm 0.34, \sigma_y = 36.3 \pm 1.7, \sigma_z = 6.0 \pm 0.34)\,\mu$m. We choose a random Rb atom to excite to the Rydberg state and then locate the 10 nearest KRb molecules in the cloud. We consider the pairwise interaction between the Rydberg atom and every molecule. As we include more molecules (farther ones) in the model, their corresponding interaction strength V_{dd} decreases dramatically due to its $1/r^3$ dependence. Therefore, including the three nearest molecules can reproduce about 90% of the observed broadening, and incorporating additional neighbors leads to a saturation of the simulated broadening, as shown in Fig. 6.13. This demonstrates a collective effect, meaning that more than one KRb molecule interacts with the Rydberg atom, causing the broadening to increase beyond the single-neighbor picture. Physically, this indicates that the single quanta of dipolar excitation is distributed among the Rydberg atom and all nearby molecules.

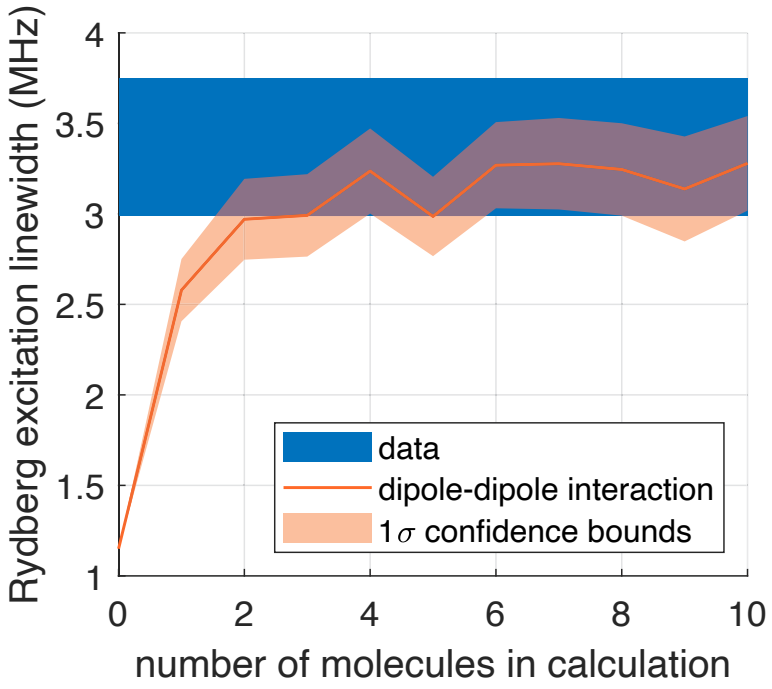

Figure 6.13: Simulated Rydberg excitation linewidth as a function of the number of nearest KRb molecules in the simulation [130]. Blue and orange: 1-σ confidence interval of the measured broadening and the simulated Rydberg spectrum's FWHM.

Because the dipolar interaction strength V_{dd} depends on the atom-molecule distance, a reduction in the Rydberg spectral linewidth is expected at lower KRb densities. Additionally, as the separation between Rb atoms and neighboring KRb molecules increases, the aforementioned collective enhancement effect diminishes, further contributing to the decrease in the Rydberg linewidth. To verify this dependence, we controllably reduce the KRb density with a microwave shelving scheme, as shown in Fig. 6.15. We start by exciting a desired portion of the KRb

molecules to $N = 1$ with a microwave pulse (2.227 GHz) that rotates the state in the Bloch sphere with a θ angle (θ-rotation pulse). After this, we dissociate the remaining $N = 0$ molecules into atoms with a reversed STIRAP pulse and magnetic field ramp and remove all K atoms and part of the Rb atoms using the imaging light. Finally, we use a microwave π-pulse to transfer the remaining $N = 1$ population back to $N = 0$. As shown in Fig. 6.14, the excitation linewidths increase from 1.1 MHz to 3.2 MHz as we increased the KRb density from 0 to $3.38 \times 10^{11}/\text{cm}^3$.

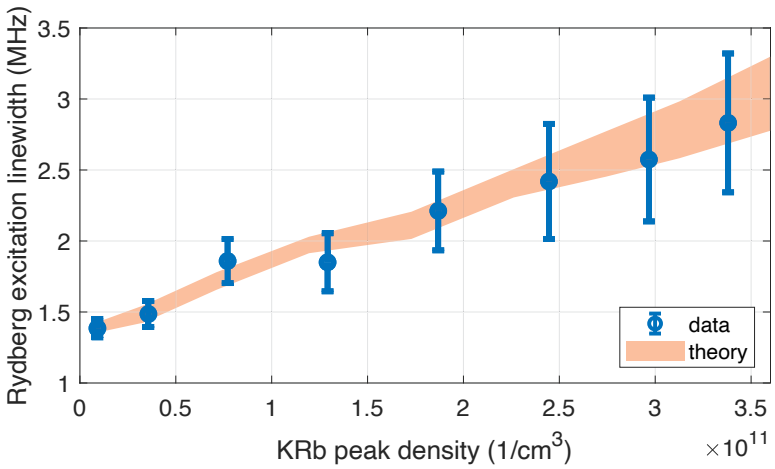

Figure 6.14: Rydberg excitation linewidth as a function of peak KRb molecule density [130]. We varied the KRb density between 0 and $3.38 \times 10^{11}/\text{cm}^3$.

We note that we inevitably lose some KRb molecules during this process, which primarily occurs during the reversed STIRAP step, where a short 690 nm pulse is applied near-resonant to the $N = 1$ molecules. This may lead to some off-resonant excitations of the hide-out $N = 1$ molecules. We consider these as pure losses and

ignore them entirely since the decayed molecules would most likely end up in some rovibronic excited states, which cannot be imaged. They do not participate in any resonant dipolar interactions.

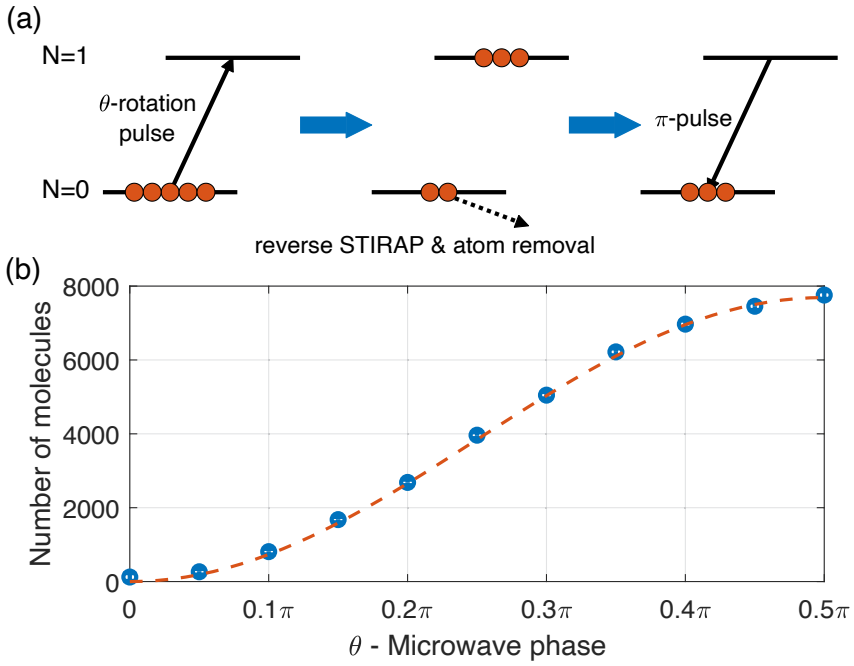

Figure 6.15: Microwave sequence controlling the KRb number density [130]. (a) The microwave shelving sequence is used to partially remove KRb molecules. (b) Measured remaining KRb molecule number versus the rotation angle θ. We fit the result to a sinusoidal function due to the nature of Rabi oscillations.

During the process, the Rb density is also affected by the second removal pulse and is generally lower than in previous experiments. However, this should not be an issue: Because the resonant interaction that we care is between atoms and molecules,

the Rydberg excitation linewidth should not depend on the Rb atom density in a low atom density regime ($\sim 10^{10}/\text{cm}^3$) [142]. Here, we provide an experimental test by measuring the Rydberg excitation linewidths at various Rb atom densities. We remove a controllable portion of the Rb atoms in the ensemble with a microwave ARP pulse, transferring some Rb atoms to the $|F = 2, m_F = 2\rangle$ state, which are subsequently expelled by a resonant laser pulse. We maintain a constant KRb density and keep the atom-molecule system on resonance as we vary the Rb density. In the end, we find that the Rydberg excitation linewidth has no dependence on the Rb density, as shown in Fig. 6.16.

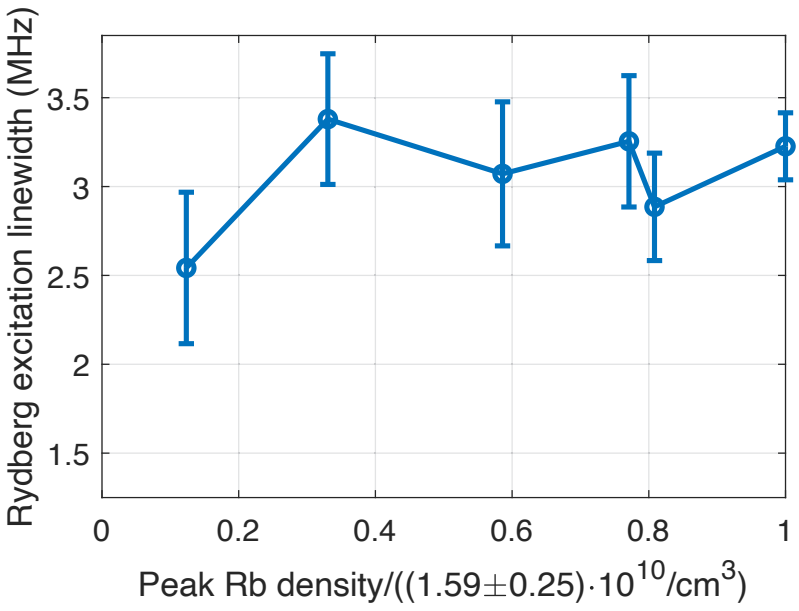

Figure 6.16: Rydberg excitation linewidth as a function of Rb atom density [130].

6.3 Conclusion and Outlook

In summary, we observed the resonant energy transfer process between Rb Rydberg atoms and KRb molecules at ultracold temperatures. We perform direct ionization detection of the rotational excited N = 1 KRb molecules and measure the broadening of the Rydberg excitation transition of Rb atoms, both of which are strong proof of the resonant interaction. To explain our observations quantitatively, we develop a dipole-dipole interaction model with a Monte Carlo simulation, which shows good agreement with the experimental data. Additionally, it is crucial to incorporate multiple nearby KRb molecules into the simulation model to accurately reproduce the observed broadening data, indicating that collective effects are significant. Our work paves the way for utilizing these interactions for various quantum applications in a hybrid system, such as computing and simulation. Specifically for our experiment, a natural next step would be exploring the central spin model at higher KRb densities, where the collective effect is stronger. For the broader community, demonstrating coherent dynamics of this interaction in a more spatially confined setting, such as inside optical-tweezer-based systems, would allow the demonstration of interspecies gates.

While the dipolar interaction model explains our results very well, the highest KRb density we used in our experiment is close to the threshold where a significant portion of Rydberg Rb atoms have a KRb neighbor within their Rydberg electron cloud, as shown in Fig. 6.17. We determined the Rydberg atom radius to be 1 μm

(dashed line in the figure) as the wavefunction falls off dramatically beyond it. This radius corresponds to a characteristic KRb density threshold of $1 \times 10^{12}/\text{cm}^3$. At the maximum KRb density that we have in the experiment ($4.29 \pm 0.36 \times 10^{11}/\text{cm}^3$), there is a 39% probability of finding a single KRb molecule within the Rydberg orbit and a 14% probability of finding two.

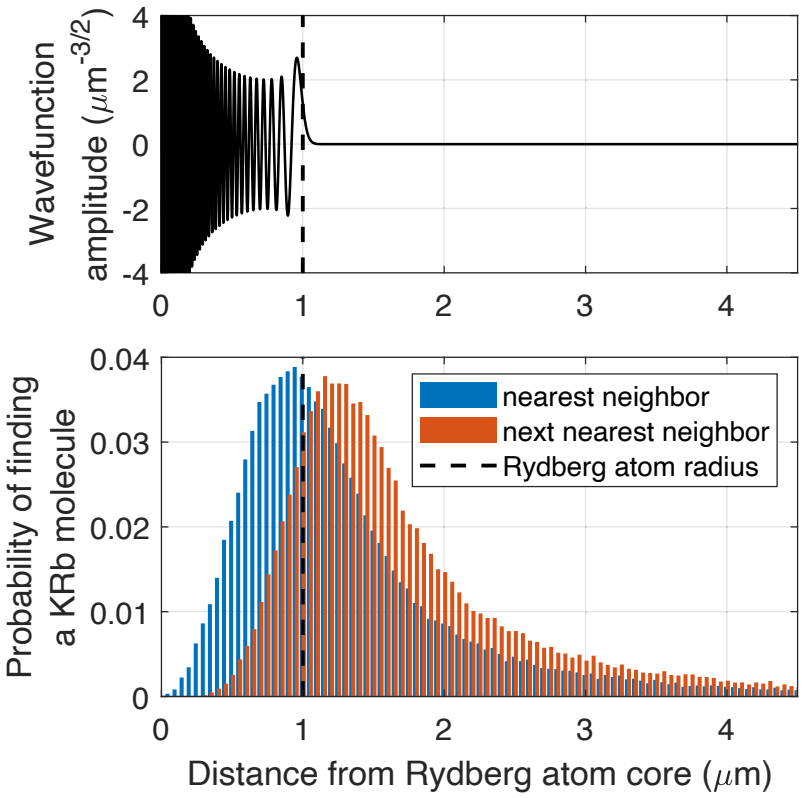

Figure 6.17: Wavefunction of the $98D_{5/2}$ Rydberg electron and the distance distribution of the nearest and the next nearest KRb molecules from a Rydberg atom [130].

When a KRb molecule is located inside the Rydberg electron orbit, the dipolar

interaction model becomes inaccurate as the point dipole approximation starts to deviate significantly. This is shown in Fig. 6.18, where the two potential energy curves diverge for interparticle distances within 1 μm.

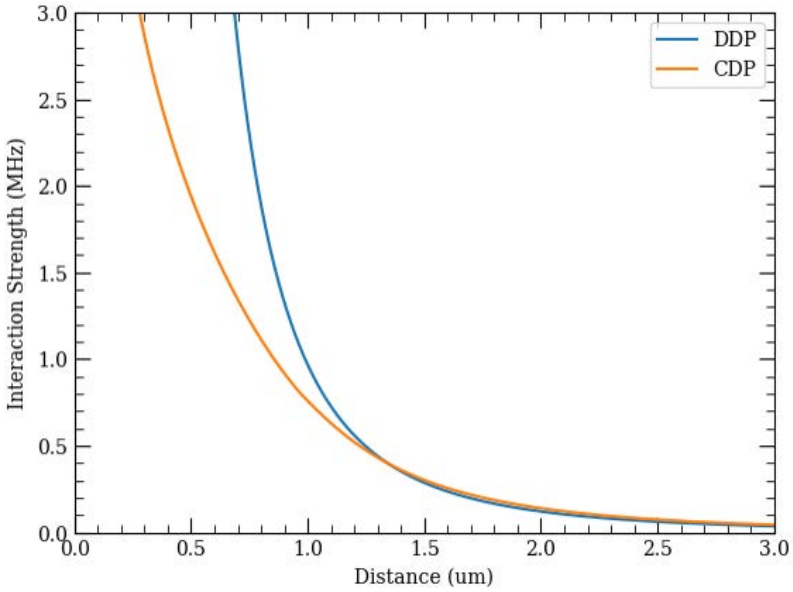

Figure 6.18: Comparison between the charge–dipole and dipole–dipole interactions between Rydberg Rb and KRb. In both cases, the relative orientation is fixed: the intermolecular axis and the internuclear axes of both species are aligned along the z-direction.

Approximately 40% of KRb molecules lie within the Rydberg orbit, and the notable deviation between the charge-dipole and dipole-dipole interaction energy curves at short range (Fig. 6.18) suggests that a charge-dipole interaction model may be necessary. However, this discrepancy is mitigated by geometric considerations: the volume of a spherical shell scales as $r^2\delta r$, which vanishes as the distance r

approaches zero. Consequently, although the interaction energy difference becomes increasingly pronounced at short distances, the likelihood of finding a KRb molecule in that regime is correspondingly suppressed, thereby reducing the observable impact of the deviation. This effect is further enhanced by the interaction blockade effect that happens at short range, which significantly limits Rydberg excitation. However, since the dipolar Hamiltonian has a steeper slope compared to the charge-dipole interaction, one would naively expect a difference between the two models.

When we use both models in our simulation, we illustrate them in Fig. 6.19, where the FWHM of the predicted broadening deviates significantly at high KRb densities. At our highest accessible KRb density, the results favor the dipole-dipole interaction model. This seemingly puzzling finding can be attributed to two additional effects that are neglected in the simulation: motion-induced decoherence and short-range chemical reactions.

1. **Motion-induced decoherence.** At small atom-molecule distances, the frozen-gas approximation fails, which is a fundamental assumption of our simulation model. During the 3 μs excitation pulse, the atom-molecule wavepacket (de Broglie wavelength $\sim$ 300 nm) evolves significantly under the interaction potential, causing decoherence that reduces the Rydberg excitation.

2. **Chemical reactions.** Close-range Rydberg atom-molecule pairs can undergo fast reactions that limit their lifetime. This type of loss mechanism has been observed in Rb Rydberg-Rb systems, displaying lifetimes of $\sim$ 10 μs [143].

Similar processes in our system would also occur, leading to a reduction of Rydberg signals at short range.

With these two additional effects, Rydberg excitation at short atom-molecule distances is strongly suppressed. Therefore, the Rydberg spectroscopy signal predominantly comes from the long-range interacting pairs, which matches the prediction from the dipole-dipole model.

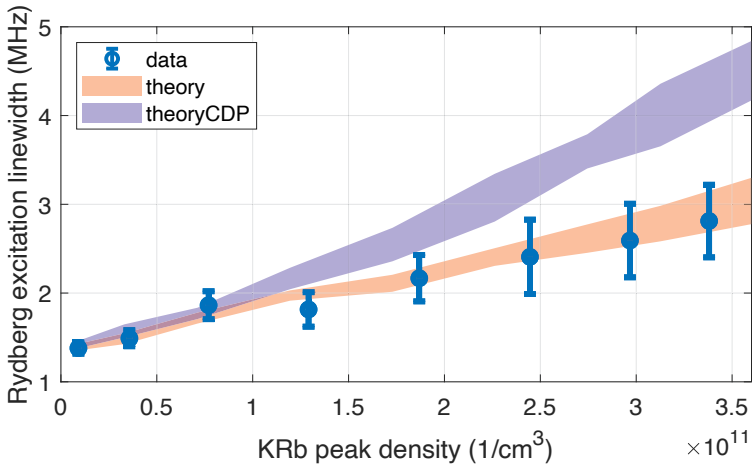

Figure 6.19: Comparison between the charge-dipole and dipole-dipole interaction Hamiltonian. The purple and orange shaded regions represent the 1-σ confidence interval of the simulated Rydberg spectrum's FWHM under the charge-dipole and dipole-dipole Hamiltonian, respectively. We overlay the experimental data presented in Fig. 6.14 as blue circles. We assume the atom-molecule resonance condition is met and include the 10 nearest KRb molecules in both models.

Additionally, we note that state-selective Rydberg ionization, which is commonly

used in molecular beam experiments [126, 127, 128], is not yet feasible in our setup, as it would require precise control over high-voltage electric field ramps on the plate electrodes. The large principal quantum numbers of the Rydberg atoms further reduce the energy separation between adjacent states, making state discrimination more challenging. Nevertheless, developing the capability to distinguish between the $98D$ and $99P$ states would provide valuable insights into the dynamics of the dipolar interactions.

Lastly, we note that although we perform 5000 excitation-detection cycles over the course of one second, the majority of the Rb ion signal originates within the first few tens of cycles, during which the KRb density remains relatively constant. In this regime, we observe a decrease in KRb density of less than 10% before the depletion of Rb.

Chapter 7

Hyperfine-to-rotation energy transfer in KRb + Rb inelastic collisions

7.1 Introduction

In this section, we shift focus to the inelastic collision process $\mathrm{Rb}(|F_a, M_{F_a}\rangle = |2,2\rangle) + \mathrm{KRb}(N=0) \rightarrow \mathrm{Rb}(|1,1\rangle) + \mathrm{KRb}(N=0,1,2)$. In this Rb + KRb inelastic collision, the exothermicity associated with the Rb hyperfine transition is 6.9 GHz. This released energy is sufficient to excite the KRb molecule to its first or second rotational excited state ($N = 1, 2$). Although this process is energetically allowed, we had not previously considered it, as we believed the dominant loss mechanism

for the inelastic collision is the photoexcitation of KRb_2 complexes (see Chapter 4). Interestingly, we stumbled upon evidence of this inelastic collision process by accident while performing initial scans for the Rydberg experiment. Upon closer examination, we found that the branching ratios into the KRb rotational states $N = 0$, 1, and 2 reveal deeper insights when compared to theoretical predictions.

7.2 Mysterious appearance of $N = 1$ molecules

In our early attempts to excite Rb atoms to Rydberg states, we began with Rb atoms in the $|2, 2\rangle$ state by default. This choice was primarily motivated by the fact that driving the σ^+ transition $|5S_{1/2}, F = 2, m_F = 2\rangle \rightarrow |6P_{3/2}, F' = 3, m'_F = 3\rangle$ prepares the atom in a stretched state, which offers a simpler state decomposition in the intermediate magnetic field regime, where the Zeeman and hyperfine interactions are comparable.

As we attempted to probe excited KRb molecules in the $N = 1$ state due to resonant dipolar interactions (Chapter 6), we encountered large background readings. In particular, we observed a persistent background signal of KRb molecules in $N = 1$, even in the absence of Rydberg excitation. This motivated us to perform a systematic investigation into the origin of the $N = 1$ population.

We prepared a mixture of KRb molecules in the rotational ground state and Rb atoms either in the $|1, 1\rangle$ or $|2, 2\rangle$ hyperfine state, with the only difference being a microwave transfer pulse used to drive the Rb atoms from $|1, 1\rangle$ to $|2, 2\rangle$. We then

tuned the REMPI lasers to selectively ionize KRb molecules in $N = 1$ and recorded the statistics of the KRb ion signal over approximately 30 experimental cycles for each case, as shown in Fig. 7.1. A clear distinction can be seen between the two cases: a significant excess KRb ion signal. To verify that these signals originated from $N = 1$ KRb molecules, we detuned the REMPI laser frequency away from resonance. In this case, the two signal distributions converged, confirming that the observed difference was indeed due to selective detection of $N = 1$ molecules. We therefore conclude that $N = 1$ KRb molecules can be produced in the Rb + KRb mixture, but only when Rb atoms are in the $|2, 2\rangle$ hyperfine state.

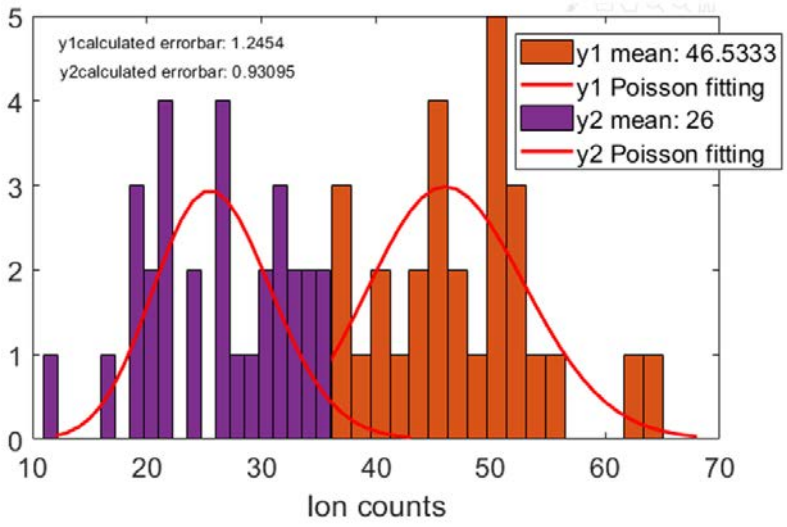

Figure 7.1: Statistics of KRb ion signals in an Rb + KRb mixture, with REMPI tuned to selectively detect the $N = 1$ state. The Rb atoms are prepared either in the $|1, 1\rangle$ state (purple) or the $|2, 2\rangle$ state (orange). Data is collected over approximately 30 experimental cycles for each case to generate a statistical distribution, which is expected to follow Poissonian statistics.

Since energy is transferred to the KRb molecules without the involvement of external sources such as photons, the only plausible source of energy is the Rb atoms themselves. This leads us to hypothesize that Rb atoms undergo a hyperfine relaxation process during collisions with the molecules, transitioning from the $|2, 2\rangle$ to the $|1, 1\rangle$ state, which releases approximately 6.9 GHz of energy at a magnetic field of 30 G. This energy can be transferred to the internal degrees of freedom of the KRb molecules, such as rotation. Given KRb's rotational constant $B = 1.114$ GHz, the released energy is sufficient to excite the molecule up to the $N = 2$ rotational

state.

7.3 Measurement and calibration of branching ratio

Now that we know rotational excited KRb can be produced from collisions between Rb in the $|2,2\rangle$ state and KRb in the $N = 0$ state, a natural question arises: what is the physical mechanism behind this process? To address this, we need to quantitatively examine the outcomes of these inelastic collisions. Specifically, measure the branching ratios of both KRb and Rb after the interaction has occurred. For KRb, this involves determining the population distribution among the three energetically allowed rotational states: $N = 0$, 1, and 2. For Rb, we measure the hyperfine state $|F', m'_F\rangle$ of the outgoing atoms. In an ideal scenario, access to the rotational projection and nuclear spin states of the KRb products would offer deeper insight into the short-range interactions. However, it requires a detailed resolution of the spectroscopic lasers and microwaves that is beyond our current capability.

To probe the outcomes, we perform state-selective ionization of both KRb and Rb. For KRb, this first requires identifying a strong transition suitable for ionization, followed by a careful scheme that avoids significant disturbance to the remaining molecular cloud. In contrast, the Rb analysis is more straightforward, as we can leverage the spectroscopic knowledge gained from the Rydberg experiments

discussed in Chapter 6.

7.3.1 Choice of KRb transition and the dark line

Although we know the STIRAP transition at 689.3 nm very well from the molecule-making process, we found that this transition is too weak for REMPI, as it couples to an excited state with mixed singlet and triplet character. Instead, we aim to identify a purely singlet excited state with a large transition dipole moment from the ground state. Based on calculated energy levels for ^{40}K^{87}Rb [144], and considering the wavelength range accessible with our existing lasers, we identified a promising candidate: the $B^1\Pi$, $\nu' = 119$ state, with a predicted transition frequency of 449928 GHz from the rovibronic ground state.

As this transition had not been previously observed experimentally, we performed a spectroscopic scan to locate the resonance. Using a laser power of 10 mW, a pulse duration of 1 ms, and a $1/e^2$ beam radius of 1 mm, we scanned the frequency range from 449820 GHz to 449941 GHz. Within this range, we observed several weak features and one prominent resonance near 449850 GHz, as shown in Fig. 7.2.

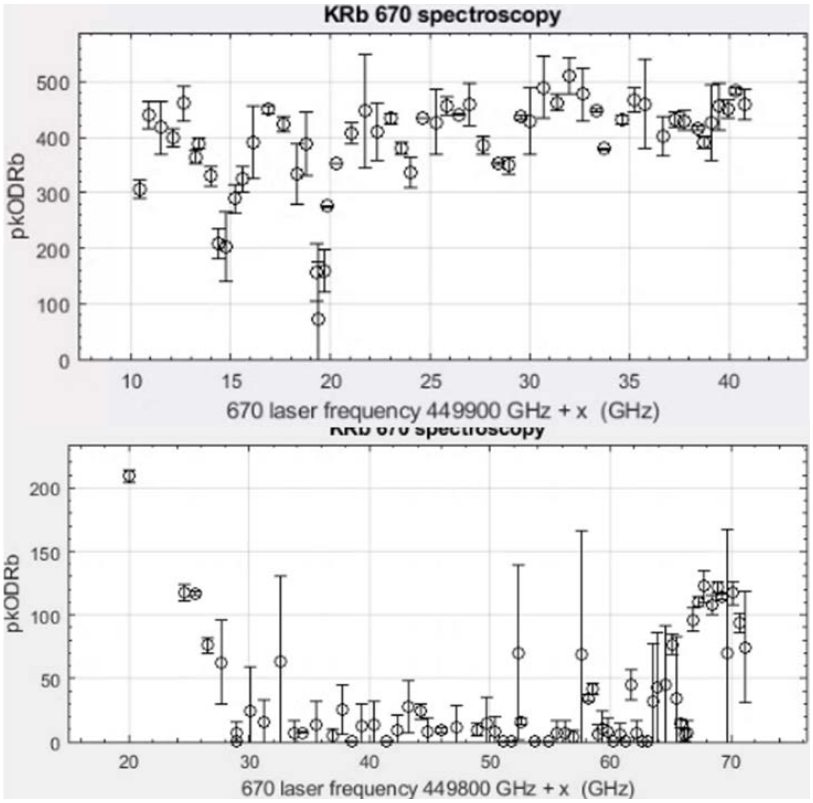

Figure 7.2: KRb REMPI spectroscopy scans. The upper panel shows several narrow dips, corresponding to weak and isolated transitions. In contrast, the lower panel exhibits a broad and well-defined dip, representing the strong transition of interest.

Once we identified the approximate transition frequency, we refined the search using lower laser power and shorter pulse durations. We determined the transition frequency to be 449846.4 GHz (666 nm), corresponding to a REMPI transition for detecting molecules in the $N = 0$ rotational state. For spectroscopy of $N = 1$ and $N = 2$ states, we first transfer the ground state molecules to the desired rotational level using microwaves, followed by a similar depletion spectroscopy procedure.

While we successfully identified suitable transitions for KRb ionization, we also needed a method to protect the remaining molecular cloud from unwanted scattering, given the large transition dipole moment. Inspired by the hollow bottle beam geometry used in [145, 100], we initially attempted to use a dark mask to block the ionization beam. However, this method proved insufficient for effective protection. We then implemented a simple solution: casting the shadow of a copper wire (American Wire Gauge 36, diameter 127 μm) across the molecular cloud. This produces a shadow approximately 250 μm in diameter, which shields the molecules sufficiently from the ionization beam.

The ionization scheme is implemented as follows: we modulate the ODT at 5 kHz with a 50% duty cycle. During the dark period, a resonant laser pulse is first applied to remove flying KRb product molecules from previous cycles. We then wait 45 μs to allow newly formed KRb products to reach the ionization region. After this delay, the REMPI pulse is fired. The resulting ions are accelerated by an electric field and detected by the MCP detector. Rb ionization is carried out using a similar scheme, with two key differences: the 666 nm laser used for KRb is replaced with a 420 nm laser for Rb, and the optimal REMPI timing is slightly adjusted. The complete ionization sequence and corresponding spectroscopic data are shown in Fig. 7.3.

We find that the Rb spectroscopy data are consistent with the assumption that all Rb atoms start in the $|1, 1\rangle$ state. Based on the absence of a significant signal at other expected transition frequencies, we estimate that less than 5% of Rb atoms

occupy the $|1,0\rangle$ or $|1,-1\rangle$ states. For KRb, we observe ion signals corresponding to the $N = 0$, 1, and 2 rotational states, in agreement with theoretical predictions.

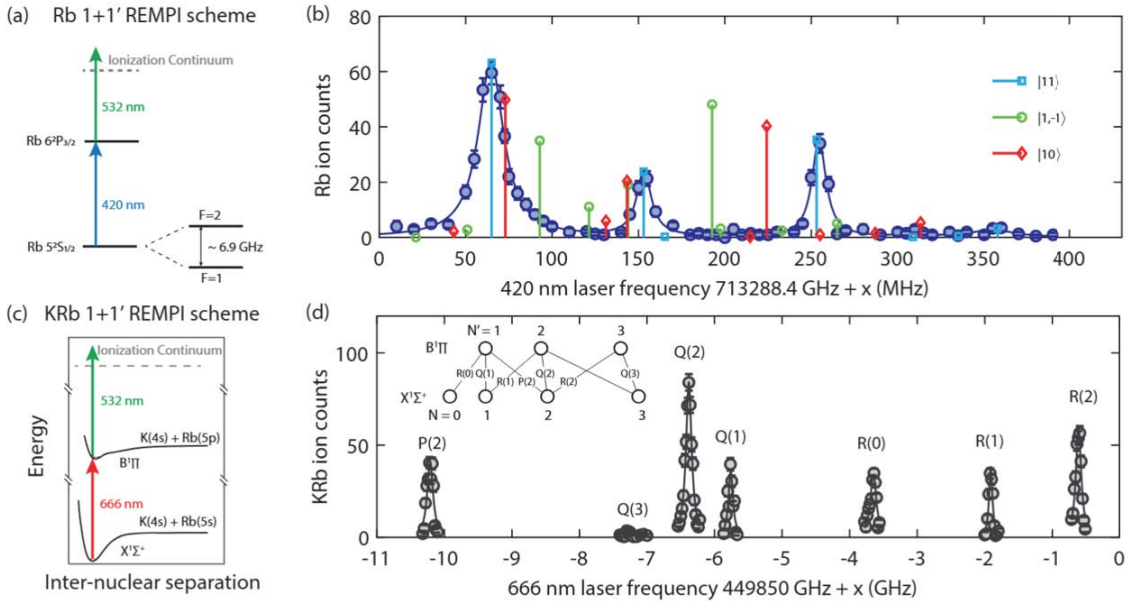

Figure 7.3: REMPI detection of collision products [77]. (a) Rb REMPI detection scheme (b) Rb REMPI spectroscopy collision products. Data points (blue circles) are compared with simulated transition line positions (vertical lines), corresponding to different $5S_{1/2}$ hyperfine states. Line heights are modeled using the polarization components of the 420 nm laser, assuming an equal population among Zeeman levels, and scaled to match the $|1,1\rangle$ data. (c) KRb REMPI detection scheme. (d) KRb REMPI spectra of collision products. Scanning the 666 nm laser over the 11 GHz range revealed features corresponding to P ($\Delta N = -1$), Q ($\Delta N = 0$), and R ($\Delta N = +1$) transitions for $N = 0$, 1, and 2. Solid lines are Lorentzian fits. We note that no ion signal was observed for $N = 3$.

7.3.2 Normalization and calibration

In addition to observing the presence of KRb molecules in $N = 0$, 1, and 2, it is also important to measure the branching ratios into these three channels. However, this task is nontrivial due to several factors. First, KRb molecules in different rotational states have different velocities due to energy conservation. This leads to two key effects: 1. They experience different Doppler shifts, and 2. They leave the ionization region at different speeds, resulting in experiencing different numbers of ionization pulses. The second effect was not initially recognized but was later found to be critical, as resonant light may fail to fully remove KRb products from previous cycles.

Furthermore, because the excited state is a Π state, it lacks a total $J = 0$ level. As a result, the $N = 0$ molecules can only access an R-branch transition. In contrast, it is more advantageous to use Q-branch transitions for ionizing $N = 1$ and $N = 2$ molecules. Consequently, the different transitions result in varying Rabi rates, which must be carefully accounted for to calibrate the branching ratios accurately.

Therefore, we performed a REMPI delay scan to measure the population in each rotational state, while simultaneously extracting the Rabi rates and excited state lifetimes for comparison. We selected the Q2, Q1, and R0 transitions and varied the delay between the onset of the 666 nm pulse and the 532 nm pulse, while recording the KRb ion signal, as shown in Fig. 7.4.

In principle, the ion signal as a function of delay time reflects the excited state

population of KRb under continuous driving by the 666 nm laser, which would ideally exhibit Rabi oscillations. However, because the Rabi frequency is comparable to the excited state decay rate, and due to ensemble averaging effects, we do not observe clear oscillations in the measured time dependence.

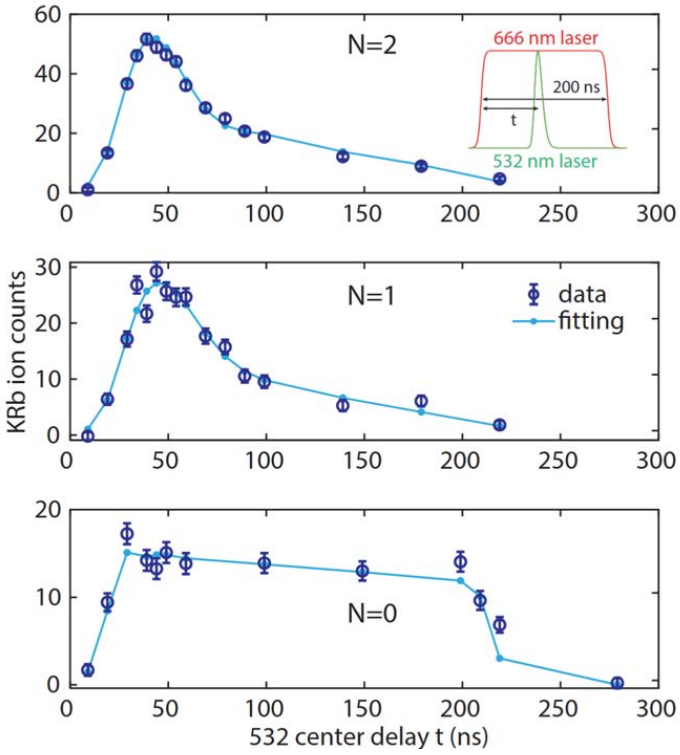

Figure 7.4: Extracting KRb branching ratios with a pulse delay scan [77]. The relative time delay between the 666 nm and 532 nm REMPI pulses is scanned, with the 666 nm laser resonant with the Q2 (top), Q1 (middle), and R0 (bottom) transitions, respectively. The 666 nm pulse duration is fixed at 200 ns. The inset shows a laser pulse schedule, displaying the powers of the REMPI beams as a function of time. Blue circles are data points. Solid lines are fits to a Monte Carlo simulation (discussed later). From the lineshapes, we extract the Rabi rates of the three transitions and determine the populations of molecules in the three rotational states after the collision.

To accurately model the time dependence of the REMPI signal for calibration

of the branching ratios, we performed a Monte Carlo simulation that accounted for KRb products flying out at all times and in all directions. The simulation incorporated several important factors: 1. the Rabi rate of the 666 nm transition was comparable to the excited state decay rate, so a single ionization event could not fully deplete the ground state population, 2. the small kinetic energy release from the collision allowed products to experience multiple ionization pulses within the detection volume, and 3. the Gaussian intensity profile of the ionization beams introduced spatial dependence in the 666 nm Rabi rates. In the simulation, both the 666 nm and 532 nm beams have Gaussian profiles with a $1/e^2$ radius of 1 mm, and a dark region with a 250 μm shadow at the beam center to match the experimental geometry of the dark line. KRb product molecules were initialized at the trap center with velocities $v_0 = 4.18$ m/s, $v_1 = 3.54$ m/s, and $v_2 = 0.74$ m/s for $N = 0$, 1, and 2, respectively. The molecules were launched in a random direction at a time randomly drawn to model asynchronous production.

The quantum dynamics for each molecule were computed by solving the optical Bloch equations with decay in the excited state:

$$\begin{aligned}
\frac{d}{dt}\rho_{gg} &= -\frac{i}{2}(\Omega_{ge}\rho_{eg} - \text{c.c.}), \\
\frac{d}{dt}\rho_{ee} &= -(\Gamma + \Gamma_{\text{ion}})\rho_{ee} + \frac{i}{2}(\Omega_{ge}\rho_{eg} - \text{c.c.}), \\
\frac{d}{dt}\rho_{eg} &= -\frac{1}{2}(\Gamma + \Gamma_{\text{ion}})\rho_{eg} + i\Delta\rho_{eg} + \frac{i}{2}\Omega_{eg}(\rho_{ee} - \rho_{gg}),
\end{aligned} \tag{7.1}$$

where Ω_{ge} is the Rabi rate of the 666 nm transition, Δ is the detuning, Γ is the

excited state decay rate, and Γ_{ion} is the ionization rate by the 532 nm laser. The ion counts were calculated as the integral $\int dt\, \rho_{ee}(t)\Gamma_{\text{ion}}(t)$, where $\Gamma_{\text{ion}}(t)$ followed the temporal profile of the 532 nm pulses measured with a photodetector.

The excited state decay rate $\Gamma = 2\pi \times 15.6(3.2)$ MHz was independently measured with absorption imaging and fixed in the simulation. The peak ionization rate at the beam center was determined to be $\Gamma_{\text{ion}} = 2\pi \times 5$ MHz [43] by scaling the 532 nm intensity. Doppler shifts from the moving molecules and position-dependent REMPI beam intensities were fully included in the simulation.

During fitting, we allowed the initial molecule number, the 666 nm Rabi rate, and the 666 nm detuning to vary freely, while fixing the decay rate, the REMPI beam geometries, and the temporal pulse profiles.

For the R0 transition, we also accounted for a time-dependent light shift induced by the 532 nm pulse (the cause of the flat ion counts versus delay time). We modeled the excited-state hyperfine structure by extending the two-level model to three independent excited states with identical Rabi and decay rates. Light shifts were not observed for the Q1 and Q2 transitions. Neglecting hyperfine effects for Q1 and Q2 would result in an overestimation of at most 5% in the extracted excited state populations.

The fitted Rabi rates for the Q2, Q1, and R0 transitions were $2\pi \times 10.2(2)$ MHz, $2\pi \times 10.0(5)$ MHz, and $2\pi \times 13.7(1.0)$ MHz, respectively, with error bars representing a 68% confidence interval. The extracted R0 Rabi rate agrees well with an

independently measured value from absorption spectroscopy, $2\pi \times 14(4)$ MHz. Furthermore, the ratios among the three Rabi rates are consistent with the Hönl-London factors [146] for $X^1\Sigma^+$ to $B^1\Pi$ transitions. Additionally, no polarization dependence of the KRb ion counts was observed across all transitions, further supporting that the projection of N along the quantization axis was scrambled in the collision.

At the same time, we extracted the number of molecules in each rotational state and determined the branching ratios for $N = 2$, 1, and 0 to be 0.53(9) : 0.33(8) : 0.13(3). The error bars were calculated by propagating the 68% confidence intervals from the fitted molecule numbers and also assuming a 10% fluctuation in the initial atom and molecule numbers.

We also studied collisions between Rb in the $|2, 2\rangle$ state and KRb molecules prepared in $N = 1$, and found that the product KRb rotational state populations followed a branching ratio of 0.59(13) : 0.32(9) : 0.09(2) for $N = 2$, 1, and 0, respectively. This result suggests that the scattering process is relatively insensitive to the initial conditions and the details of the interaction potential energy surface.

One might wonder if a pure atom exchange, where the incoming Rb atom swaps with the Rb in the KRb molecule, could explain the observations. In collisions between KRb in the $|0, 0, -4, 1/2\rangle$ state and Rb in the $|2, 2\rangle$ state, the nuclear spins of the two Rb atoms are indeed different, allowing the outgoing Rb atom to occupy the $|1, 1\rangle$ hyperfine state after exchange.

To test whether this atom exchange alone could account for our results, we studied collisions involving KRb in the $|0, 0, -4, 3/2\rangle$ state and Rb in the $|2, 2\rangle$ state, where both Rb atoms have the same nuclear spin projection $M_{I,\mathrm{Rb}} = 3/2$. In this case, we still observed KRb molecules excited to the $N = 2$ state after the collision, indicating that coupling between atomic spin and mechanical rotation must be present in the KRb_2 system, as a pure chemical exchange process would only lead to elastic scattering.

7.4 Statistical theory

To explain our observations, we first turn to a statistical theory, motivated by the fact that the measured KRb branching ratios resemble a $5 : 3 : 1$ pattern. A complete explanation must address both the Rb spin outcome and the KRb rotational distributions.

The observed Rb spin flip from $|2, 2\rangle$ to $|1, 1\rangle$ can be understood using a statistical theory of collision complexes, combined with a time-dependent perturbation treatment of the spin degrees of freedom [105]. In this framework, the collision complex is modeled as an Rb atom repeatedly bouncing off a KRb molecule, with the average time between collisions estimated from classical trajectories under a C_6 potential. Given a typical GHz-scale spin-dependent interaction strength [147] and a measured complex lifetime of 0.54(10) ns (Chapter 4), the probability of a single Rb spin flip is close to unity, while the likelihood of a second flip into the $|1, 0\rangle$

state is negligible. This matches the experimental observations.

Turning to the KRb rotational outcomes, the relative populations of $N = 0$, 1, and 2, being proportional to their degeneracies of $2N + 1$, suggest a statistical picture before invoking full quantum scattering calculations. Assuming the collision is ergodic and that all available complex and exit states are populated uniformly, we can predict the expected KRb branching ratios.

A more systematic and rigorous treatment is shown as follows: In total, there are six angular momenta involved in the system: molecular rotation $\hat{\mathbf{N}}$, collision partial wave $\hat{\mathbf{L}}$, Rb atomic nuclear spin $\hat{\mathbf{I}}_a$, Rb electronic spin $\hat{\mathbf{S}}$, and the K and Rb molecular nuclear spins, $\hat{\mathbf{I}}_1$ and $\hat{\mathbf{I}}_2$, respectively. Since our detection resolves only the atomic spin and molecular rotation, the molecular nuclear spins and partial wave contributions are reflected statistically in the degeneracies of the $N = 0$, 1, and 2 rotational channels.

Under weak external electric and magnetic fields (we observe similar branching ratios at both 2 G and 30 G), the total angular momentum $\hat{\mathbf{J}}$ is conserved. Here, $\hat{\mathbf{J}}$ is the vector sum of the mechanical angular momentum $\hat{\mathbf{J}}_r = \hat{\mathbf{N}} + \hat{\mathbf{L}}$ and the spin angular momentum $\hat{\mathbf{F}} = \hat{\mathbf{S}} + \hat{\mathbf{I}}_a + \hat{\mathbf{I}}_1 + \hat{\mathbf{I}}_2$.

Assuming all degrees of freedom are fully scrambled during the collision, the statistical model predicts a branching ratio of $0.544 : 0.340 : 0.116$ for $N = 2 : 1 : 0$, which agrees well with the experimentally measured values.

However, if spin-dependent interactions in the Hamiltonian were too weak, the

mechanical angular momentum J_r would be conserved. In that case, the model assuming conservation of $J_r = 0$ would predict equal populations $(1 : 1 : 1)$ across the $N = 0$, 1, and 2 states, which clearly disagrees with the experiment. Therefore, the observed branching ratios support a statistical hypothesis, provided that J_r can change freely in the collision.

7.5 PES and coupled-channel calculations

This section is based on collaboration with the team led by Michał Tomza and Timur Tschurbul.

To validate the statistical theory, it is crucial to investigate whether the underlying assumption that J_r is not conserved actually holds. This requires a quantitative analysis of various spin-dependent interactions in the short range:

$$\hat{V}_{\mathrm{sd}} = \sum_{m=1,2,a} \left[A_m^{\mathrm{FC}}(R,r,\theta)\, \hat{\mathbf{S}} \cdot \hat{\mathbf{I}}_m + \hat{\mathbf{S}} \cdot \mathbf{A}_m^{\mathrm{ahf}}(R,r,\theta) \cdot \hat{\mathbf{I}}_m \right] + \hat{\mathbf{S}} \cdot \epsilon(R,r,\theta) \cdot (\hat{\mathbf{N}} + \hat{\mathbf{L}}) \tag{7.2}$$

where R is the atom-molecule separation, r is the internuclear distance within KRb, and θ is the orientation angle between them.

The intermolecular hyperfine interactions between the electronic spin $\hat{\mathbf{S}}$ and the nuclear spins $\hat{\mathbf{I}}_m$ consist of scalar Fermi contact terms $A_m^{\mathrm{FC}}(R,r,\theta)$ and anisotropic

hyperfine tensor couplings $\mathbf{A}_m^{\mathrm{ahf}}(R, r, \theta)$. The spin-rotation interaction between the total mechanical rotation ($\hat{\mathbf{N}} + \hat{\mathbf{L}}$) and the electronic spin is described by the tensor $\epsilon(R, r, \theta)$. All terms in Eq. 7.2 depend on θ and couple spins to mechanical rotation, providing a possible mechanism for the J_r non-conservation and the hyperfine-to-rotation energy transfer.

Among these terms, the Fermi contact interaction is typically the dominant spin-dependent coupling at short range, with characteristic strengths on the order of GHz [147]. However, the Fermi contact interaction conserves J_r, which cannot be responsible for J_r breaking alone.

In contrast, the intermolecular spin-rotation interaction, tensor hyperfine interaction, and the intramolecular nuclear electric quadrupole interaction within KRb can couple states with different J_r. The short-range strength of the spin-rotation coupling is typically around 10 MHz, but can be enhanced to the GHz level near a conical intersection (CI), known to exist in our system (Fig. 7.5). The tensor hyperfine interaction is typically $\sim$10 MHz for Rb + KRb collisions. The nuclear electric quadrupole interaction in KRb is weaker, typically less than 1 MHz.

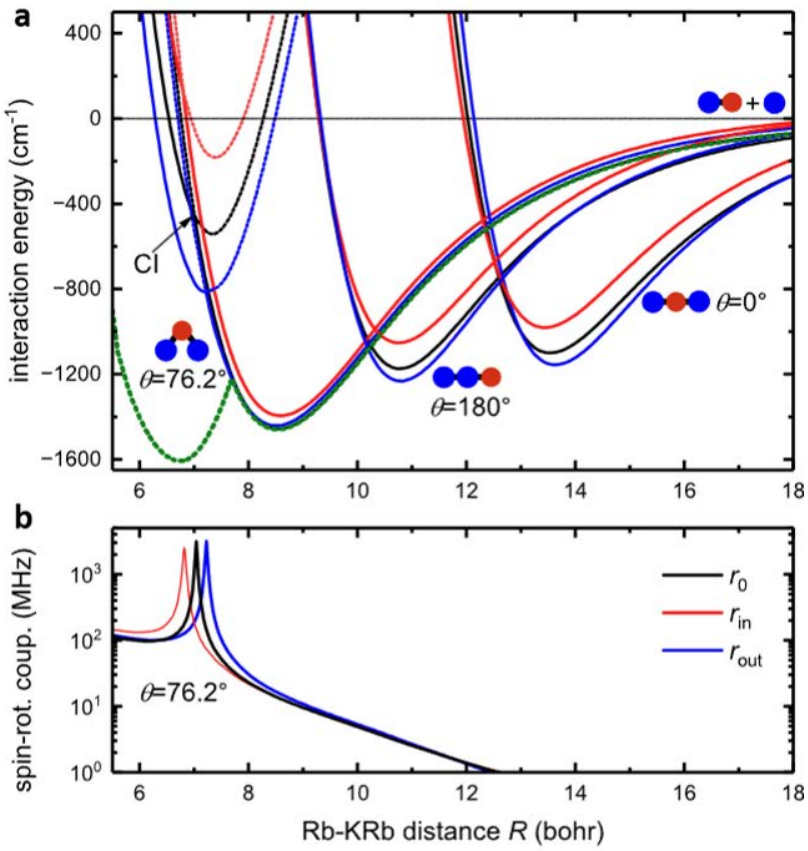

Figure 7.5: Potential energy surfaces and spin-rotation coupling of the Rb+KRb system [77] (a) One-dimensional cuts through the three-dimensional electronic interaction potential $V(R, r, \theta)$ for the ground (solid lines) and first excited (dashed lines) electronic states. Three orientations θ are shown: two linear configurations ($\theta = 0°$ and 180°) and a bent configuration where a conical intersection (CI) occurs ($\theta_{\mathrm{CI}} \approx 76.2°$). Three intramolecular KRb distances are selected: the vibrationally averaged bond length r_0 and the inner and outer classical turning points r_{in} and r_{out} of the ground rovibrational level. For linear geometries, the excited state potential lies outside the plotted energy range. The green dotted line shows the ground state interaction energy at θ_{CI}, minimized over r. (b) Isotropic spin-rotation coupling.

While the strengths of short-range interactions can be estimated and the CI between electronic states has been identified, it remains computationally intractable to fully model all these effects in a complete quantum scattering calculation. To make progress, we adopt two key simplifying assumptions: first, the KRb molecule is treated as a rigid rotor, which reduces the number of scattering channels and keeps the computational complexity manageable. Second, the CI between the ground and first excited electronic states of Rb-KRb is neglected for the exact same reason.

Under these approximations, a coupled-channel (CC) model is developed to capture Rb + KRb collisions in an external magnetic field, based on *ab initio* potential energy surfaces [147] and spin-dependent interactions [Eq. 7.2]. This approach rigorously includes all rotational and spin degrees of freedom, along with Zeeman effects.

Interestingly, within this CC model, J_r is found to be nearly perfectly conserved under the adopted approximations. To explore the influence of the CI, we included the spin-rotation tensor in the model, artificially enhancing it near the CI. The calculations show that, even with significant enhancement, the spin-rotation interaction would need to be inflated by an additional factor of $\gtrsim 100$ to break J_r conservation. This suggests that the effects of vibrational modes and the CI extend beyond merely enhancing the spin-rotation interaction, indicating that a more rigorous treatment, by explicitly incorporating vibrational degrees of freedom and the CI into future calculations, would be necessary.

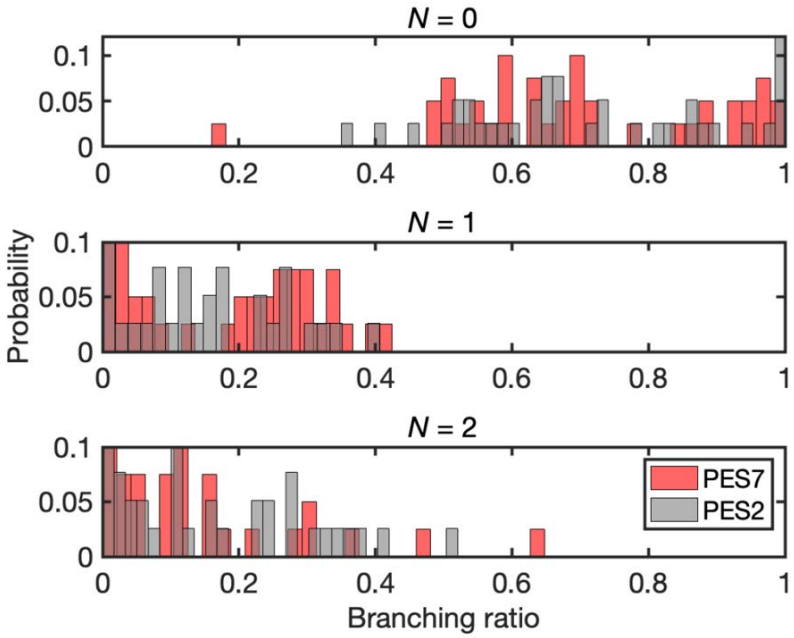

Figure 7.6: Product KRb rotational state distributions from the CC calculations [77]. The distributions represent the state-to-state inelastic cross sections into a given final KRb rotational state (N), summed over all hyperfine sublevels within each N manifold and normalized. The results are averaged over 40 samples each of two potential energy surfaces: PES2 (grey) and PES7 (red). Here, PES2 and PES7 differ in the number of radial expansion terms $V_\lambda(R)$ included in their Legendre polynomial expansion: PES2 includes only the V_0 and V_2 terms, while PES7 incorporates additional higher-order anisotropic terms up to $\lambda \leq 7$.

In this calculation, Fig. 7.6 displays the resulting product KRb rotational state distribution, where the population peaks at the lowest rotational state, $N = 0$, which completely disagrees with experimental observations. The corresponding Rb product

state distribution is dominated by the $|F_a = 1, M_{F_a} = 1\rangle$ and $|F_a = 2, M_{F_a} = 1\rangle$ hyperfine states.

Although it is possible to bring the CC calculations into agreement with the observed product state distributions by fine-tuning the strength of the Rb-KRb interaction, the resulting potential energy surface would only fit in a narrow parameter space, contradictory with the $N = 1$ branching ratio observations, and the experimentally observed total inelastic rate would still not be reproduced.

The lack of quantitative agreement between experiment and quantum scattering calculations, which are based solely on the ground-state PES (neglecting CI) and the rigid-rotor approximation, strongly suggests that vibrational degrees of freedom and excited electronic surfaces play essential roles.

This conclusion is further supported by the interaction strength calculations, which show that at short range, the rigid-rotor approximation breaks down due to the energetic accessibility of the excited electronic state of Rb-KRb. Moreover, the strong enhancement of spin-rotation coupling near the CI, where the electron g-factor approaches zero, could lead to Majorana-type spin-flip transitions. Thus, the CI could introduce strong mixing between different J_r manifolds and explain the statistical distribution of KRb rotational states observed in the experiment.

7.6 Conclusion and Outlook

Our experiment revealed energy transfer from the atomic hyperfine degree of freedom to molecular rotation during collisions between Rb ($|2,2\rangle$) and KRb ($|0,0,-4,1/2\rangle$). After the collision, Rb atoms predominantly occupied a single hyperfine state ($|1,1\rangle$), while KRb molecules were distributed among rotational levels up to $N = 2$.

Interestingly, the observed outcomes align with a statistical model that assumes J_r non-conservation. To investigate the underlying mechanisms, we performed state-of-the-art quantum scattering calculations. However, under the rigid-rotor approximation and using only the ground-state potential energy surface, J_r remains conserved, and the calculated branching ratios and inelastic scattering cross sections fail to quantitatively reproduce the experimental results.

In contrast, electronic structure calculations revealed a strong enhancement of the spin-rotation coupling near a conical intersection, which is energetically accessible and may significantly influence the collision dynamics. Fully converged quantum scattering calculations incorporating vibrational modes and conical intersections remain beyond the reach of current computational capabilities. Nevertheless, our findings provide additional insight into the exceptionally long lifetime of ground-state Rb-KRb complexes observed in earlier experiments [99]. For the spin-state combination explored here, we measured a complex lifetime of 0.54 ns (Chapter 4), compared to a calculated RRKM lifetime of 0.6 ps based on the ground-state PES without spin-rotation coupling. Properly accounting for nuclear

spins and spin-dependent interactions could dramatically increase the density of states, potentially bringing theoretical predictions into better agreement with experimental observations.

Chapter 8

Future directions

In this final chapter, I briefly discuss three experimental projects that we have partially conceived. I will outline the motivations, experimental ideas, and potential challenges associated with each project. Due to time constraints, it was not possible to fully realize these experiments within the duration of my Ph.D. Nevertheless, they represent exciting opportunities (at least in my view) and may be of interest to future generations of researchers.

8.1 K + KRb reactions

Among the limited number of chemical reactions and inelastic collisions accessible in our system, the $\mathrm{K} + \mathrm{KRb} \rightarrow \mathrm{K}_2 + \mathrm{Rb}$ reaction remains largely unexplored experimentally. Numerically exact quantum scattering calculations have predicted

chaotic behavior [58] in the rovibronic product state distribution of the K_2 molecules. With an exothermicity of ~ 225 cm^{-1}, the total number of accessible K_2 product states is ~ 140, which is not prohibitively large. In principle, using REMPI, it would be possible to map out the full product state distribution, providing a valuable benchmark for comparison with theory.

It is important to note that the theoretical calculations neglect all spin degrees of freedom (both electronic and nuclear) and are performed on a single electronic potential energy surface [58]. Our recent work on Rb + KRb collisions [77] has revealed significant discrepancies between theory and experiment, highlighting the critical roles played by vibrational motion, conical intersections, and spin degrees of freedom at short range. It is therefore reasonable to expect that spins will also play an essential role in the K + KRb reaction, making an experimental test against the spinless and conical-interaction-free theory particularly meaningful.

Experimentally, the goal sounds straightforward: prepare a sample of K atoms and KRb molecules and probe the K_2 product state distribution across all channels using REMPI. However, this task is nontrivial. Literature values for the $^{40}K_2$ transitions are incomplete, requiring experimental searches for transition frequencies for each product channel. Additionally, the products are significantly faster (at least four times faster than the K_2 products from KRb + KRb reactions), posing further challenges in detection and accumulating statistics.

Even if mapping all product channels proves infeasible, important information can still be obtained by studying the rotational parity of the K_2 products. For

instance, when reactants are prepared in well-defined hyperfine states, K in $|9/2, -9/2\rangle$ and KRb in $|0, 0, -4, 1/2\rangle$, the nuclear spins of the two K atoms are identical and are in stretched states ($|I_{\mathrm{K}} = 4, m_{I_{\mathrm{K}}} = -4\rangle$). If nuclear spins are conserved during the reaction, as suggested in [36], the product K_2 molecules should populate a symmetric nuclear spin state $|I_{\mathrm{K}_2} = 8, m_{I_{\mathrm{K}_2}} = -8\rangle$, thereby restricting the product rovibronic states to be symmetric. This prediction can be tested by selectively probing a subset of product channels of choice, rather than covering all rovibronic states.

8.2 Alternative explanations for KRb + KRb reactions in superposition states

We have observed puzzling outcomes in the KRb + KRb reaction when the reactants are prepared in superposition states: in some cases, the results suggest that coherence is preserved, while in others, coherence appears to be lost.

In discussions with our theory collaborator Goulven Quéméner, we identified an alternative way to analyze the reaction, particularly when the two colliding KRb molecules are prepared with slightly different phases (for example, in $\frac{1}{\sqrt{2}}(|0\rangle + |1\rangle)$ and $\frac{1}{\sqrt{2}}(|0\rangle + e^{i\phi}|1\rangle)$). The key idea is to decompose the two-body system into spatially symmetric and antisymmetric channels. The antisymmetric spatial channel corresponds to the standard p-wave collision pathway for two identical fermionic

KRb molecules with a symmetric spin wavefunction. This case has been extensively studied in [79], and corresponds to a zero imprinted phase in our recent theoretical framework of [118].

When ϕ is nonzero, a symmetric spatial channel becomes possible. In this case, two KRb molecules can collide via s-wave, provided their spin wavefunction is antisymmetric. This corresponds to a π phase shift in the imposed superposition, as discussed in [118]. The total reaction outcome is thus a statistical sum over contributions from both the symmetric and antisymmetric spatial channels.

This framework provides a potential explanation for the unusually high population observed in the $|e, e\rangle$ channel in Case 3 of the superposition initial state experiments. If the majority of KRb molecules react through the symmetric channel (s-wave) under those conditions, such an outcome becomes plausible.

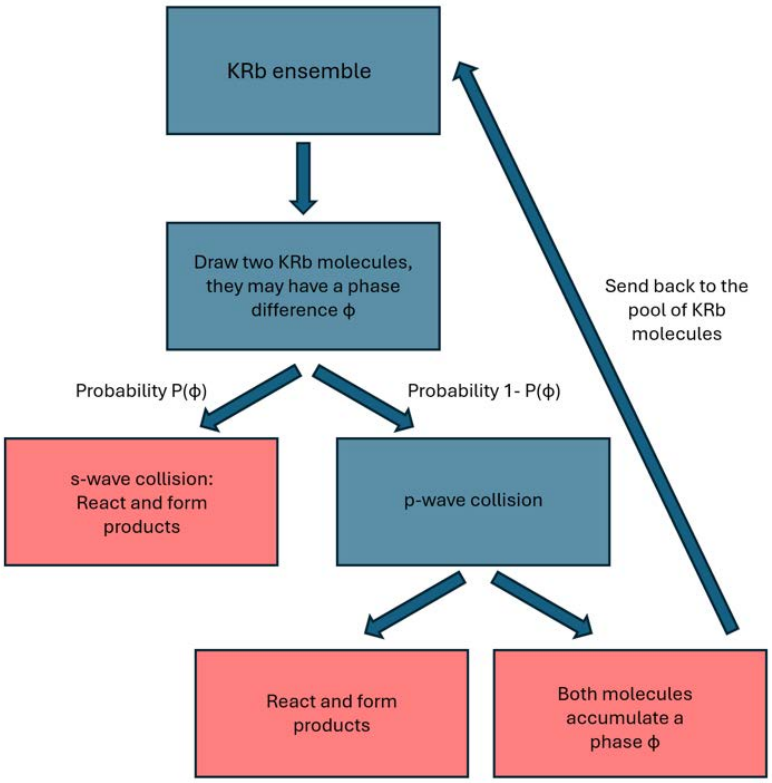

Figure 8.1: Procedure flowchart illustrating the creation of reaction products in KRb + KRb collisions through different symmetry channels.

A natural question then arises: what could generate a phase difference ϕ between KRb molecules? A recent study [148] has shown that collisions between KRb molecules prepared in superpositions of rotational states can induce decoherence. Although the superposition only involves different hyperfine states in our case, it is plausible that a slight collision-induced phase shift could arise, creating a relative phase ϕ between the molecules. Within this framework, we propose an alternative picture to explain the KRb + KRb reaction result, as summarized in the flowchart

in Fig. 8.1.

To validate this hypothesis, several missing pieces must be addressed. First, we need to determine what fraction of reaction events proceed through each symmetry channel. This may be achievable through Ramsey measurements. Although oscillations are consistently observed in all Ramsey experiments, the relative decay rates vary with the choice of initial state. These decay rates could potentially provide insight into the proportion of molecules reacting via each channel.

In parallel, a theoretical investigation is necessary to explore the physical origin of this phase shift. If a collision-induced phase does exist, one could perform a Monte Carlo simulation incorporating this phase into an ensemble of KRb molecules and track collisions in different symmetry channels to test whether it can reproduce the experimental observations.

8.3 Near-threshold reactions

Chemical reactions occurring near energetic thresholds can exhibit behavior fundamentally different from those with significant excess energy. The combination of ultracold temperatures and precise control of external electric and magnetic fields in our system allows us to fine-tune the exothermicity of a given reaction pathway with unprecedented precision. This opens the door to systematically studying threshold effects in chemical reactions.

A particularly viable system for such investigations is the inelastic collision between Rb ($|2,2\rangle$) and KRb ($N = 0$), which was examined at low electric fields in Chapter 7. In this collision, the dissociation channel Rb ($|1,1\rangle$) + KRb ($N = 2$) lies approximately 170 MHz below the initial state. This energy release can be controlled using an external electric field, which modifies the rotational energy level spacings of KRb via DC Stark shifts, while leaving the Rb energy levels largely unchanged. At sufficiently large electric fields (on the order of ~ 5 kV/cm, still too small to cause significant shifts for Rb), the energy gap between the KRb $N = 0$ and some $N = 2$ states exceeds the Rb hyperfine splitting between $|2,2\rangle$ and $|1,1\rangle$, effectively shutting off the corresponding reaction pathway. By tuning the electric field near this critical threshold, one can probe the product state distribution as a function of energy release, providing new insights into near-threshold reaction dynamics.

Experimentally, this study would require improvements to the electric field generation setup, as the current system begins to arc at an applied voltage of approximately 3 kV. Additionally, at higher electric fields, the degeneracy between different m_N states of KRb is lifted. This necessitates spectroscopic resolution of individual m_N states, effectively increasing the number of product channels that must be measured and calibrated.

References

[1] E. F. Caldin, "Tunneling in proton-transfer reactions in solution," *Chemical Reviews*, vol. 69, no. 1, pp. 135–156, 1969.

[2] R. P. Bell, *The tunnel effect in chemistry*. Springer, 2013.

[3] V. A. Benderskii, D. E. Makarov, and C. A. Wight, *Chemical Dynamics at Low Temperatures, Volume 88*, vol. 88. John Wiley & Sons, 2009.

[4] M. J. Knapp and J. P. Klinman, "Environmentally coupled hydrogen tunneling: Linking catalysis to dynamics," *European Journal of Biochemistry*, vol. 269, no. 13, pp. 3113–3121, 2002.

[5] S. Hammes-Schiffer, "Hydrogen tunneling and protein motion in enzyme reactions," *Accounts of chemical research*, vol. 39, no. 2, pp. 93–100, 2006.

[6] R. J. McMahon, "Chemical reactions involving quantum tunneling," *Science*, vol. 299, no. 5608, pp. 833–834, 2003.

[7] J. Meisner and J. Kästner, "Atom tunneling in chemistry," *Angewandte Chemie International Edition*, vol. 55, no. 18, pp. 5400–5413, 2016.

[8] E. P. Wigner, "On the behavior of cross sections near thresholds," *Physical Review*, vol. 73, no. 9, p. 1002, 1948.

[9] P. Paliwal, N. Deb, D. M. Reich, A. v. d. Avoird, C. P. Koch, and E. Narevicius, "Determining the nature of quantum resonances by probing elastic and reactive scattering in cold collisions," *Nature Chemistry*, vol. 13, no. 1, pp. 94–98, 2021.

[10] X. Wang, W. Dong, M. Qiu, Z. Ren, L. Che, D. Dai, X. Wang, X. Yang, Z. Sun, B. Fu, *et al.*, "Hf (v= 3) forward scattering in the f+ h2 reaction:

shape resonance and slow-down mechanism," *Proceedings of the National Academy of Sciences*, vol. 105, no. 17, pp. 6227–6231, 2008.

[11] C. Chin, R. Grimm, P. Julienne, and E. Tiesinga, "Feshbach resonances in ultracold gases," *Reviews of Modern Physics*, vol. 82, no. 2, pp. 1225–1286, 2010.

[12] C. L. Shoemaker and R. E. Wyatt, "Feshbach resonances in chemical reactions," *Advances in quantum chemistry*, vol. 14, pp. 169–240, 1981.

[13] M. Qiu, Z. Ren, L. Che, D. Dai, S. A. Harich, X. Wang, X. Yang, C. Xu, D. Xie, M. Gustafsson, *et al.*, "Observation of feshbach resonances in the f+ h2→ hf+ h reaction," *Science*, vol. 311, no. 5766, pp. 1440–1443, 2006.

[14] J. J. Park, Y.-K. Lu, A. O. Jamison, T. V. Tscherbul, and W. Ketterle, "A feshbach resonance in collisions between triplet ground-state molecules," *Nature*, vol. 614, no. 7946, pp. 54–58, 2023.

[15] S. Haze, J.-L. Li, D. Dorer, J. P. D'Incao, P. S. Julienne, E. Tiemann, M. Deiß, and J. Hecker Denschlag, "Controlling few-body reaction pathways using a feshbach resonance," *Nature Physics*, pp. 1–5, 2025.

[16] F. Fernández-Alonso and R. N. Zare, "Scattering resonances in the simplest chemical reaction," *Annual review of physical chemistry*, vol. 53, no. 1, pp. 67–99, 2002.

[17] A. Teslja and J. J. Valentini, "State-to-state reaction dynamics: A selective review," *The Journal of chemical physics*, vol. 125, no. 13, 2006.

[18] X. Yang, "State-to-state dynamics of elementary bimolecular reactions," *Annu. Rev. Phys. Chem.*, vol. 58, no. 1, pp. 433–459, 2007.

[19] G. Zhang, D. Lu, H. Guo, and H. Gao, "Imaging the state-to-state charge-transfer dynamics between the spin-orbit excited ar+ (2p1/2) ion and n2," *Nature Communications*, vol. 15, no. 1, p. 1001, 2024.

[20] X. Yang*, "State-to-state dynamics of elementary chemical reactions using rydberg h-atom translational spectroscopy," *International Reviews in Physical Chemistry*, vol. 24, no. 1, pp. 37–98, 2005.

[21] D. B. Blasing, J. Pérez-Ríos, Y. Yan, S. Dutta, C.-H. Li, Q. Zhou, and Y. P. Chen, "Observation of quantum interference and coherent control in a photochemical reaction," *Physical review letters*, vol. 121, no. 7, p. 073202, 2018.

[22] L. Zhu, V. Kleiman, X. Li, S. P. Lu, K. Trentelman, and R. J. Gordon, "Coherent laser control of the product distribution obtained in the photoexcitation of hi," *Science*, vol. 270, no. 5233, pp. 77–80, 1995.

[23] B. Sheehy, B. Walker, and L. DiMauro, "Phase control in the two-color photodissociation of hd+," *Physical review letters*, vol. 74, no. 24, p. 4799, 1995.

[24] A. Shnitman, I. Sofer, I. Golub, A. Yogev, M. Shapiro, Z. Chen, and P. Brumer, "Experimental observation of laser control: Electronic branching in the photodissociation of n a 2," *Physical review letters*, vol. 76, no. 16, p. 2886, 1996.

[25] M. Shapiro and P. Brumer, "Coherent control of collisional events: Bimolecular reactive scattering," *Physical review letters*, vol. 77, no. 12, p. 2574, 1996.

[26] S. S. Kale, Y. P. Chen, and S. Kais, "Constructive quantum interference in photochemical reactions," *Journal of Chemical Theory and Computation*, vol. 17, no. 12, pp. 7822–7826, 2021.

[27] P. G. Jambrina, D. Herráez-Aguilar, F. J. Aoiz, M. Sneha, J. Jankunas, and R. N. Zare, "Quantum interference between h+ d2 quasiclassical reaction mechanisms," *Nature chemistry*, vol. 7, no. 8, pp. 661–667, 2015.

[28] Y. Xie, H. Zhao, Y. Wang, Y. Huang, T. Wang, X. Xu, C. Xiao, Z. Sun, D. H. Zhang, and X. Yang, "Quantum interference in h+ hd→ h2+ d between direct abstraction and roaming insertion pathways," *Science*, vol. 368, no. 6492, pp. 767–771, 2020.

[29] W. Chen, R. Wang, D. Yuan, H. Zhao, C. Luo, Y. Tan, S. Li, D. H. Zhang, X. Wang, Z. Sun, *et al.*, "Quantum interference between spin-orbit split partial waves in the f+ hd→ hf+ d reaction," *Science*, vol. 371, no. 6532, pp. 936–940, 2021.

[30] A. Enríquez-Cabrera, Y. Lai, L. Salmon, L. Routaboul, and A. Bousseksou, "Spin-state effect on the efficiency of a post-synthetic modification reaction on a spin crossover complex," *Communications Chemistry*, vol. 8, no. 1, p. 47, 2025.

[31] H.-Z. Xue, J.-H. Wu, B.-W. Wang, S. Gao, and J.-L. Zhang, "Coordination induced spin state transition switches the reactivity of nickel (ii) porphyrin in hydrogen evolution reaction," *Angewandte Chemie International Edition*, vol. 64, no. 1, p. e202413042, 2025.

[32] Y. Zhang, Q. Wu, J. Z. Y. Seow, Y. Jia, X. Ren, and Z. J. Xu, "Spin states of metal centers in electrocatalysis," *Chemical Society Reviews*, 2024.

[33] J. N. Harvey, "Understanding the kinetics of spin-forbidden chemical reactions," *Physical Chemistry Chemical Physics*, vol. 9, no. 3, pp. 331–343, 2007.

[34] J. N. Harvey, "Spin-forbidden reactions: computational insight into mechanisms and kinetics," *Wiley Interdisciplinary Reviews: Computational Molecular Science*, vol. 4, no. 1, pp. 1–14, 2014.

[35] T. Oka, "Nuclear spin selection rules in chemical reactions by angular momentum algebra," *Journal of Molecular Spectroscopy*, vol. 228, no. 2, pp. 635–639, 2004.

[36] M.-G. Hu, Y. Liu, M. A. Nichols, L. Zhu, G. Quéméner, O. Dulieu, and K.-K. Ni, "Nuclear spin conservation enables state-to-state control of ultracold molecular reactions," *Nature Chemistry*, vol. 13, no. 5, pp. 435–440, 2021.

[37] N. J. Turro, "Influence of nuclear spin on chemical reactions: magnetic isotope and magnetic field effects (a review)," *Proceedings of the National Academy of Sciences*, vol. 80, no. 2, pp. 609–621, 1983.

[38] U. E. Steiner and T. Ulrich, "Magnetic field effects in chemical kinetics and related phenomena," *Chemical Reviews*, vol. 89, no. 1, pp. 51–147, 1989.

[39] L. J. Butler, "Chemical reaction dynamics beyond the born-oppenheimer approximation," *Annual review of physical chemistry*, vol. 49, no. 1, pp. 125–171, 1998.

[40] D. R. Yarkony, "Diabolical conical intersections," *Reviews of Modern Physics*, vol. 68, no. 4, p. 985, 1996.

[41] D. Polli, P. Altoè, O. Weingart, K. M. Spillane, C. Manzoni, D. Brida, G. Tomasello, G. Orlandi, P. Kukura, R. A. Mathies, *et al.*, "Conical intersection dynamics of the primary photoisomerization event in vision," *Nature*, vol. 467, no. 7314, pp. 440–443, 2010.

[42] Y. Boeije and M. Olivucci, "From a one-mode to a multi-mode understanding of conical intersection mediated ultrafast organic photochemical reactions," *Chemical Society Reviews*, vol. 52, no. 8, pp. 2643–2687, 2023.

[43] Y. Liu, M.-G. Hu, M. A. Nichols, D. Yang, D. Xie, H. Guo, and K.-K. Ni, "Precision test of statistical dynamics with state-to-state ultracold chemistry," *Nature*, vol. 593, no. 7859, pp. 379–384, 2021.

[44] D. Egorov, T. Lahaye, W. Schöllkopf, B. Friedrich, and J. M. Doyle, "Buffer-gas cooling of atomic and molecular beams," *Physical Review A*, vol. 66, no. 4, p. 043401, 2002.

[45] D. Egorov, W. Campbell, B. Friedrich, S. Maxwell, E. Tsikata, L. Van Buuren, and J. Doyle, "Buffer-gas cooling of nh via the beam loaded buffer-gas method," *The European Physical Journal D-Atomic, Molecular, Optical and Plasma Physics*, vol. 31, pp. 307–311, 2004.

[46] N. R. Hutzler, H.-I. Lu, and J. M. Doyle, "The buffer gas beam: An intense, cold, and slow source for atoms and molecules," *Chemical reviews*, vol. 112, no. 9, pp. 4803–4827, 2012.

[47] S. Y. van de Meerakker, N. Vanhaecke, and G. Meijer, "Stark deceleration and trapping of oh radicals," *Annu. Rev. Phys. Chem.*, vol. 57, no. 1, pp. 159–190, 2006.

[48] S. Y. Van De Meerakker, H. L. Bethlem, and G. Meijer, "Taming molecular beams," *Nature Physics*, vol. 4, no. 8, pp. 595–602, 2008.

[49] W. Ketterle, "Nobel lecture: When atoms behave as waves: Bose-einstein condensation and the atom laser," *Reviews of Modern Physics*, vol. 74, no. 4, p. 1131, 2002.

[50] E. A. Cornell and C. E. Wieman, "Nobel lecture: Bose-einstein condensation in a dilute gas, the first 70 years and some recent experiments," *Reviews of Modern Physics*, vol. 74, no. 3, p. 875, 2002.

[51] T. Langen, G. Valtolina, D. Wang, and J. Ye, "Quantum state manipulation and cooling of ultracold molecules," *Nature Physics*, vol. 20, no. 5, pp. 702–712, 2024.

[52] K.-K. Ni, S. Ospelkaus, M. De Miranda, A. Pe'Er, B. Neyenhuis, J. Zirbel, S. Kotochigova, P. Julienne, D. Jin, and J. Ye, "A high phase-space-density gas of polar molecules," *science*, vol. 322, no. 5899, pp. 231–235, 2008.

[53] M.-S. Heo, T. T. Wang, C. A. Christensen, T. M. Rvachov, D. A. Cotta, J.-H. Choi, Y.-R. Lee, and W. Ketterle, "Formation of ultracold fermionic nali feshbach molecules," *Physical Review A—Atomic, Molecular, and Optical Physics*, vol. 86, no. 2, p. 021602, 2012.

[54] P. K. Molony, P. D. Gregory, Z. Ji, B. Lu, M. P. Köppinger, C. R. Le Sueur, C. L. Blackley, J. M. Hutson, and S. L. Cornish, "Creation of ultracold rb 87 cs 133 molecules in the rovibrational ground state," *Physical review letters*, vol. 113, no. 25, p. 255301, 2014.

[55] J. W. Park, S. A. Will, and M. W. Zwierlein, "Ultracold dipolar gas of fermionic na 23 k 40 molecules in their absolute ground state," *Physical review letters*, vol. 114, no. 20, p. 205302, 2015.

[56] F. Wang, X. He, X. Li, B. Zhu, J. Chen, and D. Wang, "Formation of ultracold narb feshbach molecules," *New Journal of Physics*, vol. 17, no. 3, p. 035003, 2015.

[57] L. Borst and J. Floyd, "The radioactive decay of k 40," *Physical Review*, vol. 74, no. 8, p. 989, 1948.

[58] J. F. Croft, C. Makrides, M. Li, A. Petrov, B. K. Kendrick, N. Balakrishnan, and S. Kotochigova, "Universality and chaoticity in ultracold k+ krb chemical reactions," *Nature communications*, vol. 8, no. 1, p. 15897, 2017.

[59] K.-K. Ni, "A quantum gas of polar molecules," *Ph. D. Thesis*, 2009.

[60] Y. Liu, *Bimolecular chemistry at sub-microkelvin temperatures*. PhD thesis, Harvard University, 2020.

[61] W. G. Tobias, *Degenerate Polar Molecules with Controlled Interactions and Reactivity*. PhD thesis, University of Colorado at Boulder, 2022.

[62] M. Greiner, I. Bloch, T. W. Hänsch, and T. Esslinger, "Magnetic transport of trapped cold atoms over a large distance," *Physical Review A*, vol. 63, no. 3, p. 031401, 2001.

[63] H. F. Hess, "Evaporative cooling of magnetically trapped and compressed spin-polarized hydrogen," *Physical Review B*, vol. 34, no. 5, p. 3476, 1986.

[64] D. Naik and C. Raman, "Optically plugged quadrupole trap for bose-einstein condensates," *Physical Review A—Atomic, Molecular, and Optical Physics*, vol. 71, no. 3, p. 033617, 2005.

[65] T. Esslinger, I. Bloch, and T. W. Hänsch, "Bose-einstein condensation in a quadrupole-ioffe-configuration trap," *Physical Review A*, vol. 58, no. 4, p. R2664, 1998.

[66] P. B. Wigley, P. J. Everitt, A. van den Hengel, J. W. Bastian, M. A. Sooriyabandara, G. D. McDonald, K. S. Hardman, C. D. Quinlivan, P. Manju, C. C. Kuhn, *et al.*, "Fast machine-learning online optimization of ultra-cold-atom experiments," *Scientific reports*, vol. 6, no. 1, p. 25890, 2016.

[67] A. Houwman, "Diatomix, version 2.3.4.0," 2023. MATLAB package.

[68] M. H. Anderson, J. R. Ensher, M. R. Matthews, C. E. Wieman, and E. A. Cornell, "Observation of bose-einstein condensation in a dilute atomic vapor," *science*, vol. 269, no. 5221, pp. 198–201, 1995.

[69] W. Wiley and I. H. McLaren, "Time-of-flight mass spectrometer with improved resolution," *Review of scientific instruments*, vol. 26, no. 12, pp. 1150–1157, 1955.

[70] D. W. Chandler and P. L. Houston, "Two-dimensional imaging of state-selected photodissociation products detected by multiphoton ionization," *The Journal of chemical physics*, vol. 87, no. 2, pp. 1445–1447, 1987.

[71] A. T. Eppink and D. H. Parker, "Velocity map imaging of ions and electrons using electrostatic lenses: Application in photoelectron and photofragment ion imaging of molecular oxygen," *Review of Scientific Instruments*, vol. 68, no. 9, pp. 3477–3484, 1997.

[72] J. W. Goodman, *Introduction to Fourier optics*. Roberts and Company publishers, 2005.

[73] W. Ketterle, D. S. Durfee, and D. Stamper-Kurn, "Making, probing and understanding bose-einstein condensates," in *Bose-Einstein condensation in atomic gases*, pp. 67–176, IOS Press, 1999.

[74] D. A. Steck, "Rubidium 87 d line data," 2001.

[75] LIOP-TEC GmbH, "Liopstar hq tunable dye laser system manual." `https://www.liop-tec.com/resources/LiopStar-complete+2014.pdf`, 2014.

[76] Sirah Lasertechnik GmbH, "Laser dyes for tunable dye lasers." `https://www.sirah.com/accessories/dyes/`, 2024.

[77] Y.-X. Liu, L. Zhu, J. Luke, M. C. Babin, M. Gronowski, H. Ladjimi, M. Tomza, J. L. Bohn, T. V. Tscherbul, and K.-K. Ni, "Hyperfine-to-rotational energy transfer in ultracold atom–molecule collisions of rb and krb," *Nature Chemistry*, pp. 1–7, 2025.

[78] C. Glaser, F. Karlewski, J. Kluge, J. Grimmel, M. Kaiser, A. Günther, H. Hattermann, M. Krutzik, and J. Fortágh, "Absolute frequency measurement of rubidium 5 s-6 p transitions," *Physical Review A*, vol. 102, no. 1, p. 012804, 2020.

[79] Y.-X. Liu, L. Zhu, J. Luke, J. A. Houwman, M. C. Babin, M.-G. Hu, and K.-K. Ni, "Quantum interference in atom-exchange reactions," *Science*, vol. 384, no. 6700, pp. 1117–1121, 2024.

[80] K.-K. Ni, S. Ospelkaus, D. Wang, G. Quéméner, B. Neyenhuis, M. De Miranda, J. Bohn, J. Ye, and D. Jin, "Dipolar collisions of polar molecules in the quantum regime," *Nature*, vol. 464, no. 7293, pp. 1324–1328, 2010.

[81] T. Takekoshi, L. Reichsöllner, A. Schindewolf, J. M. Hutson, C. R. Le Sueur, O. Dulieu, F. Ferlaino, R. Grimm, and H.-C. Nägerl, "Ultracold dense samples of dipolar rbcs molecules in the rovibrational and hyperfine ground state," *Physical review letters*, vol. 113, no. 20, p. 205301, 2014.

[82] M. Guo, X. Ye, J. He, M. L. González-Martínez, R. Vexiau, G. Quéméner, and D. Wang, "Dipolar collisions of ultracold ground-state bosonic molecules," *Physical Review X*, vol. 8, no. 4, p. 041044, 2018.

[83] R. A. Marcus, "Unimolecular dissociations and free radical recombination reactions," *The Journal of Chemical Physics*, vol. 20, no. 3, pp. 359–364, 1952.

[84] Y. Liu, M.-G. Hu, M. A. Nichols, D. D. Grimes, T. Karman, H. Guo, and K.-K. Ni, "Photo-excitation of long-lived transient intermediates in ultracold reactions," *Nature Physics*, vol. 16, no. 11, pp. 1132–1136, 2020.

[85] P. D. Gregory, J. A. Blackmore, S. L. Bromley, and S. L. Cornish, "Loss of ultracold rb 87 cs 133 molecules via optical excitation of long-lived two-body collision complexes," *Physical Review Letters*, vol. 124, no. 16, p. 163402, 2020.

[86] R. Bause, A. Schindewolf, R. Tao, M. Duda, X.-Y. Chen, G. Quéméner, T. Karman, A. Christianen, I. Bloch, and X.-Y. Luo, "Collisions of ultracold molecules in bright and dark optical dipole traps," *Physical Review Research*, vol. 3, no. 3, p. 033013, 2021.

[87] K. K. Voges, P. Gersema, M. Meyer zum Alten Borgloh, T. A. Schulze, T. Hartmann, A. Zenesini, and S. Ospelkaus, "Ultracold gas of bosonic na 23 k 39 ground-state molecules," *Physical Review Letters*, vol. 125, no. 8, p. 083401, 2020.

[88] J. F. Croft and J. L. Bohn, "Long-lived complexes and chaos in ultracold molecular collisions," *Physical Review A*, vol. 89, no. 1, p. 012714, 2014.

[89] J. Li, B. Zhao, D. Xie, and H. Guo, "Advances and new challenges to bimolecular reaction dynamics theory," *The Journal of Physical Chemistry Letters*, vol. 11, no. 20, pp. 8844–8860, 2020.

[90] R. Bause, A. Christianen, A. Schindewolf, I. Bloch, and X.-Y. Luo, "Ultracold sticky collisions: Theoretical and experimental status," *The Journal of Physical Chemistry A*, vol. 127, no. 3, pp. 729–741, 2023.

[91] M. Mayle, G. Quéméner, B. P. Ruzic, and J. L. Bohn, "Scattering of ultracold molecules in the highly resonant regime," *Physical Review A—Atomic, Molecular, and Optical Physics*, vol. 87, no. 1, p. 012709, 2013.

[92] A. Christianen, T. Karman, and G. C. Groenenboom, "Quasiclassical method for calculating the density of states of ultracold collision complexes," *Physical Review A*, vol. 100, no. 3, p. 032708, 2019.

[93] G. Quéméner, J. F. Croft, and J. L. Bohn, "Electric field dependence of complex-dominated ultracold molecular collisions," *Physical Review A*, vol. 105, no. 1, p. 013310, 2022.

[94] M. P. Man, G. C. Groenenboom, and T. Karman, "Symmetry breaking in sticky collisions between ultracold molecules," *Physical Review Letters*, vol. 129, no. 24, p. 243401, 2022.

[95] J. F. Croft, J. L. Bohn, and G. Quéméner, "Anomalous lifetimes of ultracold complexes decaying into a single channel," *Physical Review A*, vol. 107, no. 2, p. 023304, 2023.

[96] J. F. Croft, N. Balakrishnan, and B. K. Kendrick, "Long-lived complexes and signatures of chaos in ultracold k 2+ rb collisions," *Physical Review A*, vol. 96, no. 6, p. 062707, 2017.

[97] B. K. Kendrick, H. Li, M. Li, S. Kotochigova, J. F. Croft, and N. Balakrishnan, "Non-adiabatic quantum interference in the ultracold li+ lina→ li 2+ na reaction," *Physical Chemistry Chemical Physics*, vol. 23, no. 9, pp. 5096–5112, 2021.

[98] H. Li, M. Li, C. Makrides, A. Petrov, and S. Kotochigova, "Universal scattering of ultracold atoms and molecules in optical potentials," *Atoms*, vol. 7, no. 1, p. 36, 2019.

[99] M. A. Nichols, Y.-X. Liu, L. Zhu, M.-G. Hu, Y. Liu, and K.-K. Ni, "Detection of long-lived complexes in ultracold atom-molecule collisions," *Physical Review X*, vol. 12, no. 1, p. 011049, 2022.

[100] M.-G. Hu, Y. Liu, D. D. Grimes, Y.-W. Lin, A. H. Gheorghe, R. Vexiau, N. Bouloufa-Maafa, O. Dulieu, T. Rosenband, and K.-K. Ni, "Direct observation of bimolecular reactions of ultracold krb molecules," *Science*, vol. 366, no. 6469, pp. 1111–1115, 2019.

[101] S. Chu and C. Wieman, "Laser cooling and trapping of atoms," in *Laser Materials And Laser Spectroscopy: A Satellite Meeting Of Iqec'88*, p. 340, World Scientific, 1989.

[102] D. Comparat, A. Fioretti, G. Stern, E. Dimova, B. L. Tolra, and P. Pillet, "Optimized production of large bose-einstein condensates," *Physical Review A—Atomic, Molecular, and Optical Physics*, vol. 73, no. 4, p. 043410, 2006.

[103] R. E. Continetti and H. Guo, "Dynamics of transient species via anion photodetachment," *Chemical Society Reviews*, vol. 46, no. 24, pp. 7650–7667, 2017.

[104] N. Cooper and G. V. Shlyapnikov, "Stable topological superfluid phase of ultracold polar fermionic molecules," *Physical review letters*, vol. 103, no. 15, p. 155302, 2009.

[105] M. Mayle, B. P. Ruzic, and J. L. Bohn, "Statistical aspects of ultracold resonant scattering," *Physical Review A—Atomic, Molecular, and Optical Physics*, vol. 85, no. 6, p. 062712, 2012.

[106] M. L. González-Martínez, O. Dulieu, P. Larrégaray, and L. Bonnet, "Statistical product distributions for ultracold reactions in external fields," *Physical Review A*, vol. 90, no. 5, p. 052716, 2014.

[107] G. Quemener, "Private communication," 2025. Private communication.

[108] T. Hartmann, T. A. Schulze, K. K. Voges, P. Gersema, M. W. Gempel, E. Tiemann, A. Zenesini, and S. Ospelkaus, "Feshbach resonances in na 23+ k 39 mixtures and refined molecular potentials for the nak molecule," *Physical Review A*, vol. 99, no. 3, p. 032711, 2019.

[109] H. Yang, D.-C. Zhang, L. Liu, Y.-X. Liu, J. Nan, B. Zhao, and J.-W. Pan, "Observation of magnetically tunable feshbach resonances in ultracold 23na40k+ 40k collisions," *Science*, vol. 363, no. 6424, pp. 261–264, 2019.

[110] J. J. Park, H. Son, Y.-K. Lu, T. Karman, M. Gronowski, M. Tomza, A. O. Jamison, and W. Ketterle, "Spectrum of feshbach resonances in na li+ na collisions," *Physical Review X*, vol. 13, no. 3, p. 031018, 2023.

[111] K. Jachymski and P. S. Julienne, "Analytical model of overlapping feshbach resonances," *Physical Review A—Atomic, Molecular, and Optical Physics*, vol. 88, no. 5, p. 052701, 2013.

[112] A. Christianen, G. C. Groenenboom, and T. Karman, "Lossy quantum defect theory of ultracold molecular collisions," *Physical Review A*, vol. 104, no. 4, p. 043327, 2021.

[113] P. Brumer and M. Shapiro, "Control of unimolecular reactions using coherent light," *Chemical physics letters*, vol. 126, no. 6, pp. 541–546, 1986.

[114] J. Herek, A. Materny, and A. Zewail, "Femtosecond control of an elementary unimolecular reaction from the transition-state region," *Chemical physics letters*, vol. 228, no. 1-3, pp. 15–25, 1994.

[115] J. Gong, M. Shapiro, and P. Brumer, "Entanglement-assisted coherent control in nonreactive diatom–diatom scattering," *The Journal of chemical physics*, vol. 118, no. 6, pp. 2626–2636, 2003.

[116] A. Devolder, P. Brumer, and T. V. Tscherbul, "Complete quantum coherent control of ultracold molecular collisions," *Physical Review Letters*, vol. 126, no. 15, p. 153403, 2021.

[117] M. Quack, "Detailed symmetry selection rules for reactive collisions," *Molecular Physics*, vol. 34, no. 2, pp. 477–504, 1977.

[118] J. Luke, L. Zhu, Y.-X. Liu, and K.-K. Ni, "Reaction interferometry with ultracold molecules," *Faraday Discussions*, vol. 251, pp. 63–75, 2024.

[119] S. J. Evered, D. Bluvstein, M. Kalinowski, S. Ebadi, T. Manovitz, H. Zhou, S. H. Li, A. A. Geim, T. T. Wang, N. Maskara, *et al.*, "High-fidelity parallel entangling gates on a neutral-atom quantum computer," *Nature*, vol. 622, no. 7982, pp. 268–272, 2023.

[120] R. B.-S. Tsai, X. Sun, A. L. Shaw, R. Finkelstein, and M. Endres, "Benchmarking and fidelity response theory of high-fidelity rydberg entangling gates," *PRX Quantum*, vol. 6, no. 1, p. 010331, 2025.

[121] L. R. Picard, A. J. Park, G. E. Patenotte, S. Gebretsadkan, D. Wellnitz, A. M. Rey, and K.-K. Ni, "Entanglement and iswap gate between molecular qubits," *Nature*, vol. 637, no. 8047, pp. 821–826, 2025.

[122] M. Xu, L. H. Kendrick, A. Kale, Y. Gang, G. Ji, R. T. Scalettar, M. Lebrat, and M. Greiner, "Frustration-and doping-induced magnetism in a fermi–hubbard simulator," *Nature*, vol. 620, no. 7976, pp. 971–976, 2023.

[123] K. Wang, C. P. Williams, L. R. Picard, N. Y. Yao, and K.-K. Ni, "Enriching the quantum toolbox of ultracold molecules with rydberg atoms," *PRX Quantum*, vol. 3, no. 3, p. 030339, 2022.

[124] C. Zhang and M. Tarbutt, "Quantum computation in a hybrid array of molecules and rydberg atoms," *PRX Quantum*, vol. 3, no. 3, p. 030340, 2022.

[125] A. Guttridge, D. K. Ruttley, A. C. Baldock, R. González-Férez, H. Sadeghpour, C. Adams, and S. L. Cornish, "Observation of rydberg blockade due to the charge-dipole interaction between an atom and a polar molecule," *Physical Review Letters*, vol. 131, no. 1, p. 013401, 2023.

[126] K. Gawlas and S. Hogan, "Rydberg-state-resolved resonant energy transfer in cold electric-field-controlled intrabeam collisions of nh3 with rydberg he atoms," *The Journal of Physical Chemistry Letters*, vol. 11, no. 1, pp. 83–87, 2019.

[127] S. Patsch, M. Zeppenfeld, and C. P. Koch, "Rydberg atom-enabled spectroscopy of polar molecules via forster resonance energy transfer," *The Journal of Physical Chemistry Letters*, vol. 13, no. 46, pp. 10728–10733, 2022.

[128] J. Zou and S. Hogan, "Probing van der waals interactions and detecting polar molecules by förster-resonance energy transfer with rydberg atoms at temperatures below 100 mk," *Physical Review A*, vol. 106, no. 4, p. 043111, 2022.

[129] S. G. Kukolich, "Measurement of ammonia hyperfine structure with a two-cavity maser," *Physical Review*, vol. 156, no. 1, p. 83, 1967.

[130] L. Zhu, J. Luke, R. Shaham, Y.-X. Liu, and K.-K. Ni, "Probing dipolar interactions between rydberg atoms and ultracold polar molecules," *arXiv preprint arXiv:2504.06977*, 2025.

[131] Corning, "ULE Corning Code 7972 Ultra Low Expansion Glass: Product Information," Jan. 2016. Datasheet.

[132] U. Raitzsch, R. Heidemann, H. Weimer, B. Butscher, P. Kollmann, R. Löw, H. Büchler, and T. Pfau, "Investigation of dephasing rates in an interacting rydberg gas," *New Journal of Physics*, vol. 11, no. 5, p. 055014, 2009.

[133] A. E. Siegman, *Lasers*. University science books, 1986.

[134] J. Gea-Banacloche, Y.-q. Li, S.-z. Jin, and M. Xiao, "Electromagnetically induced transparency in ladder-type inhomogeneously broadened media: Theory and experiment," *Physical Review A*, vol. 51, no. 1, p. 576, 1995.

[135] T. F. Gallagher, "Rydberg atoms," *Reports on Progress in Physics*, vol. 51, no. 2, p. 143, 1988.

[136] G. Raithel and H. Walther, "Ionization energy of rubidium rydberg atoms in strong crossed electric and magnetic fields," *Physical Review A*, vol. 49, no. 3, p. 1646, 1994.

[137] V. C. Gregoric, J. J. Bennett, B. R. Gualtieri, A. Kannad, Z. C. Liu, Z. A. Rowley, T. J. Carroll, and M. W. Noel, "Improving the state selectivity of field ionization with quantum control," *Physical Review A*, vol. 98, no. 6, p. 063404, 2018.

[138] C. H. Greene, A. Dickinson, and H. Sadeghpour, "Creation of polar and nonpolar ultra-long-range rydberg molecules," *Physical review letters*, vol. 85, no. 12, p. 2458, 2000.

[139] V. Bendkowsky, B. Butscher, J. Nipper, J. P. Shaffer, R. Löw, and T. Pfau, "Observation of ultralong-range rydberg molecules," *Nature*, vol. 458, no. 7241, pp. 1005–1008, 2009.

[140] N. Šibalić, J. D. Pritchard, C. S. Adams, and K. J. Weatherill, "Arc: An open-source library for calculating properties of alkali rydberg atoms," *Computer Physics Communications*, vol. 220, pp. 319–331, 2017.

[141] A. Savitzky and M. J. Golay, "Smoothing and differentiation of data by simplified least squares procedures.," *Analytical chemistry*, vol. 36, no. 8, pp. 1627–1639, 1964.

[142] T. C. Liebisch, M. Schlagmüller, F. Engel, H. Nguyen, J. Balewski, G. Lochead, F. Böttcher, K. M. Westphal, K. S. Kleinbach, T. Schmid, *et al.*, "Controlling rydberg atom excitations in dense background gases," *Journal of Physics B: Atomic, Molecular and Optical Physics*, vol. 49, no. 18, p. 182001, 2016.

[143] M. Schlagmüller, T. C. Liebisch, F. Engel, K. S. Kleinbach, F. Böttcher, U. Hermann, K. M. Westphal, A. Gaj, R. Löw, S. Hofferberth, *et al.*, "Ultracold chemical reactions of a single rydberg atom in a dense gas," *Physical Review X*, vol. 6, no. 3, p. 031020, 2016.

[144] D. Borsalino, B. Londoño-Florèz, R. Vexiau, O. Dulieu, N. Bouloufa-Maafa, and E. Luc-Koenig, "Efficient optical schemes to create ultracold krb molecules in their rovibronic ground state," *Physical Review A*, vol. 90, no. 3, p. 033413, 2014.

[145] Y. Liu, D. D. Grimes, M.-G. Hu, and K.-K. Ni, "Probing ultracold chemistry using ion spectrometry," *Physical Chemistry Chemical Physics*, vol. 22, no. 9, pp. 4861–4874, 2020.

[146] A. Hansson and J. K. Watson, "A comment on hönl-london factors," *Journal of Molecular Spectroscopy*, vol. 233, no. 2, pp. 169–173, 2005.

[147] K. Jachymski, M. Gronowski, and M. Tomza, "Collisional losses of ultracold molecules due to intermediate complex formation," *Physical Review A*, vol. 106, no. 4, p. L041301, 2022.

[148] A. N. Carroll, H. Hirzler, C. Miller, D. Wellnitz, S. R. Muleady, J. Lin, K. P. Zamarski, R. R. Wang, J. L. Bohn, A. M. Rey, *et al.*, "Observation of generalized tj spin dynamics with tunable dipolar interactions," *Science*, vol. 388, no. 6745, pp. 381–386, 2025.